A Stochastic Approach to modeling the Dynamics of Linear, Entangled Polymer Melt

Neergaard, Jesper

Publication date:
2002

Document Version
Publisher's PDF, also known as Version of record

A Stochastic Approach to Modeling the Dynamics of Linear, Entangled Polymer Melts

Jesper Neergaard

27th November 2001

Department of Chemical Engineering
Technical University of Denmark
DK-2800 Kongens Lyngby, Denmark

Preface

This thesis presents the results of my Ph.D project carried out at the Danish Polymer Centre, Department of Chemical Engineering, Technical University of Denmark (DTU) under supervision of Professor Ole Hassager. The project was conducted in collaboration with Center of Excellence for Polymer Science and Engineering, Chemical and Environmental Engineering Department, Illinois Institute of Technology (IIT), Chicago, Illinois, USA, and co-supervised by Professor Jay D. Schieber. The work was performed during the period from September 1998 to September 2001, and was financed through a grant from the Department of Chemical Engineering, Technical University of Denmark.

I would like to express my sincere gratitude to Professor Ole Hassager for giving me the opportunity to carry out this study at the Department of Chemical Engineering and for introducing me to rheology. I am grateful for the inspiring guidance, the fruitful discussions and endless support he offered throughout my Ph.D. project.

Also, I would like to thank Professor Jay D. Schieber, who is the mastermind behind the model proposed at the end of this thesis, for teaching me stochastics and reptation theory and for his patience during the process. I am very grateful for the numerous invaluable discussions we have had in the course of this project.

Special thanks go to Professor David C. Venerus at IIT, who provided all experimental data used in this study and always willingly offered his comments and thoughts on my work. Also in this regard, many thanks to both Jay and David for making me feel right at home in Chicago and for making my stays at IIT most convenient and enjoyable.

I would like to acknowledge my colleagues Henrik Koblitz Rasmussen, Peter Szabo and Johannes Nielsen (Joe) for their stimulating scientific and social input during my Ph.D. work. Special thanks, in this regard, go to Anders Bach, with whom I have literally lived together for the past three years sharing both office and apartment at times.

Also, many thanks to my friends for all their moral support throughout this study and beyond. Finally, I want to express my most sincere gratitude to my parents, other family and Mette for always being there for me.

Lyngby, September 2001

Jesper Neergaard

Contents

Synopsis

In this thesis we perform Brownian dynamics simulations of a full-chain reptation model to gain insight in how various microscopic dynamics, of importance for the flow of linear entangled polymer melts, affect each other and the macroscopic rheological properties.

First, we consider linear viscoelasticity. A relaxation spectrum is found for the test fluid, which is a concentrated solution of nearly monodisperse polystyrene in tricresyl phosphate, that serves as a model system for polymer melts of entangled linear chains. The relaxation spectrum is found from both small-amplitude oscillatory shear flow and from stress relaxation following small-step shear strain flow. The spectrum exhibits a plateau at moderate time constants, and a downturn at large time constants, whereas the classical reptation picture exhibits the opposite trend. Using the full-chain reptation model we study the qualitative impact on the relaxation spectrum, of including chain-length fluctuations and constraint release in the theory. We find that chain-length fluctuations are important to describe the plateau, and that incorporation of constraint release leads to the observed downturn. Constraint release is already known to be important in nonlinear flows and for polydisperse systems, but is clearly shown here to be necessary to describe the linear viscoelasticity of monodisperse systems.

Next, predictions of the full-chain reptation model in transient and steady shearing flows are studied. We discuss the effects of chain tumbling, molecular chain stretching and constraint release and their influence on the macroscopic stress as well as the extinction angle under various flow conditions. The anticipated strong correlation between normal stress and molecular stretching is confirmed, and it is found that chain tumbling causes the undershoot in extinction angle during inception of shear. Furthermore, we find that chain tumbling is itself suppressed by the presence of molecular stretching. Also investigated is the monomer density along the chain contour which reveals information about the local chain stretching and orientation. Here, it is found that the distribution of monomers along the contour becomes non-uniform when the shear rate exceeds the inverse Rouse relaxation time. In the final part of this chapter, we discuss a possible violation of the stress-optic rule during start up of steady shear flow at high shear rates.

We proceed to look at exponential shear. Here, the full-chain reptation model is used to interpret data obtained from exponential shear flow of the same entangled polystyrene solution as mentioned above. Guided by the model, which contains well known dynamics, we are able to explain all trends seen in the data, and a novel analysis of the data is suggested. This

analysis demonstrates that exponential shearing flow is no more capable of stretching polymer chains than is inception of steady shear at comparable instantaneous shear rates. In fact, we show that all exponential shear flow stresses are bounded quantitatively by stresses exhibited during inception of steady shear.

In the last chapter of this work, a new full-chain, temporary network model is proposed for nonlinear flows of linear, entangled polymeric liquids. The model is inspired by the full-chain reptation model and its properties as observed in the previous chapters of the thesis. However, the new model contains no tubes and uses a different smaller set of dynamic variables: the location of each entanglement, and the number of Kuhn steps in chain strands between entanglements. In the language of reptation, the model exhibits chain connectivity, chain-length fluctuations, chain stretching, and tube dilation.

We describe a simulation algorithm in detail, and using this algorithm we look at some predictions of the model, first in the linear viscoelastic regime and then for start up of steady shear at both low and high shear rates. Finally, we discuss options for future work and possible generalizations of the proposed theory.

Dansk Resumé

I denne afhandling udføres Brownian dynamics simuleringer af en fuld-kæde reptation model. Formålet er at opnå øget indsigt i, hvordan forskellige dynamiske effekter, som er af betydning for lineære, sammenfiltrede ("entangled") polymer smelters flydning, påvirker hinanden samt de makroskopiske reologiske egenskaber.

Vi ser først på lineær viskoelasticitet. Et relaksationsspektrum findes for test væsken, der er en koncentreret opløsning af næsten monodispers polystyren i tricresyl fosfat og benyttes som et model system for polymersmelter bestående af lineære, sammenfiltrede kæder. Relaksationsspektret findes både via lav-amplitude oscillerende forskydningsstrømning og fra spændingsrelaksation efterfølgende en lille trin forskydning. Spektret udviser et plateau for moderate tidskonstanter og aftager for store tidskonstanter, hvorimod den klassiske reptation teori forudsiger den modsatte tendens. Via fuld-kæde modellen studerer vi den kvalitative påvirkning af relaksationsspektret ved inkludering af kæde-længde fluktuationer og "constraint release" i teorien. Herved findes det, at kæde-længde fluktuationer er vigtige for beskrivelsen af plateauet, og at hensyntagen til "constraint release" fører til det observerede fald for store tidskonstanter. Det er allerede kendt, at "constraint release" har betydning for ikke-lineær strømning og for polydisperse systemer, men her vises det, at denne effekt også er nødvendig for at kunne beskrive monodisperse systemers lineære viskoelasticitet.

Herefter studeres fuld-kæde reptation modellens forudsigelser i transient og konstant forskydningstrømning. Vi diskuterer effekterne af kædeomdrejning ("tumbling"), molekylær kædestræk og "constraint release" på molekylært niveau, samt deres indflydelse på de makroskopiske spændinger og udslukningsvinklen under forskellige strømningsbetingelser. Den forventede stærke korrelation mellem normal spænding og molekylært stræk bekræftes, og vi finder, at udslukningsvinklens undersving under opstart af forskydningsstrømning skyldes kædeomdrejning. Endvidere finder vi, at kædeomdrejning undertrykkes af tilstedeværelsen af molekylært stræk. Monomer densiteten langs kædens kontur, som giver information om lokalt kædestræk og orientering, undersøges også. Her finder vi, at fordelingen af monomerer langs konturen bliver uensartet, når forskydningshastigheden overstiger den reciprokke Rouse relaksationstid. Som det sidste i denne del af afhandlingen diskuteres en mulig afvigelse fra den stress-optiske lov under opstart af forskydningsstrømning ved store forskydningshastigheder.

Vi betragter dernæst eksponentiel forskydning. Her anvendes fuld-kæde reptation modellen til at fortolke data fra målinger i eksponentiel forskydningsstrømning af den samme sammenfiltrede polystyren opløsning, som

nævnt ovenfor. Vi er i stand til at forklare alle tendenser i målingerne ved hjælp af modellen, hvis dynamik er fuldstændig kendt, og på baggrund heraf foreslås en ny metode til analyse af målingerne. Denne analyse viser, at eksponentiel forskydningsstømning ikke er i stand til at strække polymerkæder mere, end det er tilfældet under opstart af konstant forskydningsstrømning. Det vises tilmed, at alle spændinger i forbindelse med eksponentiel forskydning er kvantitativt afgrænsede af de spændinger, der opnås under opstart af konstant forskydningsstrømning med samme øjeblikkelige forskydningshastighed.

I afhandlingens sidste kapitel foreslås en ny fuld-kæde, midlertidig netværksmodel for ikke-lineær strømning af lineære, sammenfiltrede polymervæsker. Modellen er inspireret af fuld-kæde reptation modellen og dennes egenskaber, som er blevet undersøgt i de forrige kapitler af afhandlingen. Men til forskel fra fuld-kæde reptation modellen er der i den nye model ingen rør, og de færre dynamiske variable er anderledes: positionen af hvert knudepunkt ("entanglement"), samt antallet af Kuhn skridt i hvert kædestykke mellem knudepunkterne. Indenfor begreberne af reptation er der i modellen taget hensyn til sammenhæng mellem kædesegmenter, kæde-længde fluktuationer, kædestræk og dynamisk rørudvidelse. Vi beskriver en detaljeret simuleringsalgoritme, og ved hjælp af denne algoritme undersøger vi nogle af modellens egenskaber, først i det lineært viskoelastiske regime og derefter under opstart af konstant forskydningsstrømning ved både lave og høje forskydningshastigheder. Endelig diskuteres fremtidsperspektiver og muligheder for generalisering af den foreslåede teori.

1

Introduction

Prediction of the flow behavior of polymeric materials at process conditions is of great interest to the plastics manufacturing industry for design purposes of processing equipment. Traditionally, conservative designs have been made, based on empirical relations providing rough estimates of the rheological properties. However, due to the continued research and the development of increasing computational power, it has become possible to perform numerical simulations of the complex flows taking place in the processing equipment. Such simulations provide much more accurate information about the involved material behavior, which in turn result in more efficient process designs.

The research efforts concerning flow simulations involving polymeric materials may be divided into two major thrusts. The first of these thrusts deals with the task of accurately simulating flows in complex geometries, whereas the other deals with the relationship between material deformations and the stresses induced by flow. The latter constitutive relationship is nontrivial due to the viscoelastic nature of polymeric materials.

While the contents of the present thesis focuses on constitutive modeling of linear entangled polymers, some flow calculations have also been considered within the course of this Ph.D. work. Here, an algorithm was developed to simulate inflation of a circular polymeric film, which is an inhomogeneous shear-free deformation ranging from equi-biaxial to planar elongation; two types of deformation, which are of importance in polymer processing applications such as blow molding and thermoforming. The simulations provide an easy comparison of the rheological properties in these deformations as predicted by various constitutive models, since in the algorithm the constitutive equation is easily exchanged. Details of the simulation algorithm and obtained results may be found in Hassager *et al.* (1999), and are also given without further comments in Appendix B.

1.1 Constitutive Modeling Based on the Molecular Level

Employing kinetic theory, several closed form constitutive models with molecular origin have been developed for entangled polymer melts. The early models are almost all based on network theories extending the theory of rubber elasticity (Bird *et al.*, 1987) with the reptation model by Doi

and Edwards (1986) being an important exception (see Section 1.2).

Commonly, these models describe only some types of flow well while failing to capture important rheological behavior in other deformations, at least within a fixed set of parameters. However, the flows in industrial processing equipment are typically inhomogeneous, involving elements of both shearing and extensional deformations. Thus, with the development of simulators for these complex flows, the demand for more complete constitutive models, capable of describing in detail more types of deformations, is increasing.

A new class of constitutive relations with molecular origin emerged with the introduction of the CONNFFESSIT (Calculation Of Non-Newtonian Flow: Finite Elements and Stochastic SImulation Techniques) idea (Laso and Öttinger, 1993), which suggests implementing the constitutive behavior in flow simulators by means of stochastic simulations. This approach is particularly beneficial for kinetic theory models based on reptation theory, since many of these, while being unavailable in closed form, are suitable for numerical solution in terms of Brownian dynamics simulations. Hence, over the past two decades, improvement of the reptation theory has been subject to much research, due to its potential of describing the rheological behavior of linear entangled polymer melts combined with the immediate applicability in flow simulations utilizing the CONNFFESSIT approach. The concept of reptation and the evolution of the theory within this concept are outlined in the next section.

1.2 Overview of Reptation Theory

Constitutive modeling of entangled linear polymer melts based on the molecular level entered a new era when Doi and Edwards presented their reptation model (Doi and Edwards, 1978a,b,c, 1979) to describe the viscoelastic behavior of linear entangled polymer chains. Their model was a generalization of the tube concept introduced earlier by de Gennes (1971), who argued that the motion of each chain in a polymer melt is equivalent to a chain restricted to one dimensional motion inside a confining tube. The tube represents obstacles imposed by other chains in the melt, and since the motion of the chain inside the tube is restricted to be along its own contour, de Gennes named this idea "reptation". The tube concept greatly reduces the complex many-body problem of treating entanglement interactions between chains in a polymer melt.

However, Doi and Edwards left out several important dynamics on the molecular level and made additional assumptions for mathematical convenience in order to obtain analytic results. Consequently, despite its success at predicting certain rheological properties, the Doi-Edwards model (DE) fails to describe several experimentally observed characteristics in various deformations even qualitatively. Therefore, it has been the subject of much research to study the influence of systematically removing the

approximations originally made and to incorporate the microscopic dynamics missing in the DE model. Below we first outline the DE model including the assumption of independent alignment (IA). Then in the following we summarize the considered modifications of the DE model and the development of reptation theory since the introduction of the original DE model.

1.2.1 The Doi-Edwards model with independent alignment

Doi and Edwards (1978a,b,c) assume the dynamics of a single tube segment to be

$$\dot{\boldsymbol{u}} = (\boldsymbol{\delta} - \boldsymbol{u}\boldsymbol{u}) \cdot \boldsymbol{\kappa} \cdot \boldsymbol{u}, \tag{1.1}$$

where $\boldsymbol{u}$ is the unit vector describing the orientation of the tube segment, $\boldsymbol{\kappa} := (\nabla \boldsymbol{v})^{\dagger}$ is the transpose of the velocity gradient, and $\boldsymbol{\delta}$ is the unit tensor. It is seen that the tube segment first deforms affinely with the imposed flow, and then the projection operator in the parentheses returns the length of the vector back to unity providing instantaneous retraction of the chain. Hence, both the length of each tube segment and the distance between entanglements stay constant.

Neglecting inertia a force balance on the chain prescribes the dynamics of the chain within the tube. The only two forces on the chain are the friction of the chain with the tube, and the Brownian forces. If s is the distance along the contour to a point on the chain that occupies the tube segment, measured from an arbitrarily chosen point on the tube, then the dynamics are described by the stochastic differential equation

$$0 = -\zeta_{\text{segment}} Z ds + \sqrt{2 k_{\text{B}} T Z \zeta_{\text{segment}}} dW_t, \tag{1.2}$$

where, ζ_{segment} is the friction coefficient between a segment in the primitive chain and the tube, Z is the number of tube segments, k_{B} is Boltzmann's constant, T is the absolute temperature, and W_t is a Wiener process. It is noted that the total friction coefficient of the *chain* is $Z\zeta_{\text{segment}}$.

Finally, these two motions are coupled through the boundary condition

$$\boldsymbol{u} \text{ takes random orientation when } s = 0, Za, \tag{1.3}$$

where a is the equilibrium length between entanglement points. This boundary condition specifies that the chain is given a random orientation when it reptates out of the tube.

It should be noted that Curtiss and Bird, developing a systematic kinetic theory for polymer melts, arrived at a very similar model although by a different approach (Bird *et al.*, 1987). In their derivation of a diffusion equation for the polymer dynamics, they used anisotropic friction tensors to describe the hindrance of sideways motions of the polymers in concentrated systems, which essentially expresses the same physical idea as the tube in reptation.

1.2.2 Avoiding independent alignment (IA)

The assumption of independent alignment (IA), which implies uniform deformation regardless of the position along the chain contour, allowed Doi and Edwards to formulate their model as a single-segment theory as opposed to considering simultaneously the entire test chain in its surrounding tube. The IA assumption is valid for the case of single-step strain deformations, which the DE model describes extremely well, but it fails for other types of flows and in particular if the deformation includes reversing flows. Recognizing this, Doi (1980a,b) and Doi and Edwards (1986) derived a constitutive equation for double-step strain deformations with flow reversal while avoiding the IA assumption and still assuming instantaneous chain retraction. It was shown that this equation could predict reversing double-step strain deformations as long as the time between the two steps is much larger than the retraction time.

Later, Marrucci (1986) and Marrucci and Grizzuti (1986) derived the DE model without IA and showed that this leads to a correct prediction of the Weissenberg effect. The equation for double-step strain flows derived by Doi was confirmed by a full-chain model with constant contour length (Hua *et al.*, 1997). By considering the entire chain at all times, assumptions of IA and consistent averaging are avoided in this model, which also recovers the results of the DE model without IA for single-step shear strain deformations.

1.2.3 Additional chain-tube interactions

In their "rigorous" model, Doi and Edwards (1986) derived another constitutive equation taking into account that the friction between a test chain and its confining tube depends on the chain velocity relative to the tube velocity rather than the chain velocity alone, as assumed in the original DE model. Few calculations have been made with the "rigorous" model, which still contains mathematically convenient approximations for the purpose of keeping the model a single-segment theory.

Geurts and Jongschaap (1988) considered additional chain-tube interactions, and looked at the increased chain tension due to friction between the chain and the tube by means of the "reptating rope" model. More details on the physics of the reptating rope model can be found in Öttinger (1996).

1.2.4 Chain-length fluctuations

Doi realized that the failure of the DE model in predicting the correct scaling law for dependence of the longest relaxation time on molecular weight could be corrected by including chain-length fluctuations (Doi, 1983). This was later confirmed by Ketzmerick and Öttinger (1989), who performed equilibrium Brownian dynamics simulations of the DE model

with chain-length fluctuations and recovered the experimentally observed scaling exponent of 3.4.

Milner and McLeish (1998) arrived at the same result although using a different approach. They applied a theory developed for arm retraction in star-molecules (Milner and McLeish, 1997) to reptating linear chains based on the idea that motion of star arms retracting is nearly the same as the fluctuating motion of an end of a linear chain.

1.2.5 Chain stretching

Removing the assumption of instantaneous chain retraction, Marrucci and Grizzuti (1988) modified the DE model to allow for molecular chain stretching. They made predictions for steady state shear, but found no improvement over the original model for the shear viscosity power law exponent of $-\frac{3}{2}$. The reason for the too high power law exponent, which implies a maximum in the shear stress versus shear rate curve at steady state, is that the model predicts too much orientation at high shear rates. Hence, the chains become too aligned in the flow direction, and the flow loses its ability to stretch the chains. This situation is not improved by including segmental stretching in the model.

Studying the same type of model, Pearson *et al.* (1991) extended the calculations to transient flows and observed overshoot in both shear stress and first normal stress difference upon start up of steady shear. Onset of the overshoot is predicted to occur at a higher shear rate for the first normal stress difference than for the shear stress consistent with experimental data, and the predicted strains, at which the stress maxima occur, also agree with experiments.

The DE model including segmental stretch and finite extensibility has been further considered by Mead and Leal (1995) and Mead *et al.* (1995), who has made calculations for steady two-dimensional flows of both shear and extensional character. Their predictions reveal increasing molecular stretching as the extensional flow components become increasingly important.

1.2.6 Double reptation

In the DE model the tube surrounding the test chain is assumed a static object. However, the tube consists of other reptating chains making it a dynamic object, which provides additional relaxation removing some of the obstacles felt by the test chain. Based on this idea of "double reptation" or constraint release (CR), Tsenoglou (1987) and des Cloizeaux (1988) derived a successful polydispersity mixing rule for the linear viscoelastic regime, which has been further considered by Mead (1996). Double reptation has also proved to play a crucial role in the recent successes of predicting molecular weight distributions from linear viscoelastic experiments (Tuminello, 1986; Mead, 1994; Wasserman, 1995; Liu *et al.*, 1998).

Öttinger (1994) incorporated the constraint release mechanism in the DE model by means of a noise term in the time-evolution equation for orientation. Using this model he recovered the correct mixing rule in the linear regime and found an improved value of the shear viscosity power law exponent of $-\frac{4}{3}$. However, the shear stress versus shear rate curve still exhibits a maximum, despite the improved power law exponent.

1.2.7 Convective constraint release

A different constraint release mechanism important only under flow conditions was proposed by Marrucci (1996) and Ianniruberto and Marrucci (1996). They argued that another mechanism contributes to relaxation of chain orientation during flow in addition to ordinary diffusion due to thermal motion (reptation and double reptation), which also occurs in the absence of flow. The additional relaxation mechanism is constraint release induced by the flow through chain stretching followed by retraction. As the chains surrounding the test chain retract, some of them cease to create topological obstacles for the test chain, which consequently feels the presence of less constraints. Since this mechanism is induced by flow Ianniruberto and Marrucci named it convective constraint release (CCR).

Based on the idea of CCR Mead *et al.* (1998) further modified the DE model including chain stretching (Marrucci and Grizzuti, 1988; Pearson *et al.*, 1991; Mead and Leal, 1995; Mead *et al.*, 1995) to obtain a reptation model with segmental stretch, chain-length fluctuations and CCR but without the effect of double reptation and without avoiding the IA assumption. Nevertheless, the model captures many experimentally observed trends and the authors thus concluded that stretching and CCR are responsible for most discrepancies between predictions of the DE model and experimental data in nonlinear shearing flows.

1.2.8 Thermodynamic modeling approach

Öttinger and Beris (1999) recently reformulated the DE model without IA to obtain a thermodynamically admissible reptation model by means of thermodynamic modeling (Öttinger, 1999b). Using the same approach Öttinger (1999a) then derived a reptation model which includes all of the dynamic effects discussed above, except for chain-length fluctuations and connectivity between different chain segments, while avoiding the IA assumption. The predictions of the resulting single-segment model compare well with experiments capturing most trends observed in nonlinear shearing flows upon appropriate choice of the adjustable model parameters, δ_1 and δ_2 (Fang *et al.*, 2000).

1.2.9 Full-chain theory

All of the microscopic physical effects discussed above have been incorporated in a full-chain model in a self-consistent manner by Hua and Schieber (1998). Their full-chain theory is formulated in terms of a set of stochastic differential equations suitable for numerical simulations utilizing Brownian dynamics, without making any approximations such as IA or consistent averaging. A detailed description of the model and the simulation algorithm used to obtain numerical results can be found in Appendix A.

The model, whose lone adjustable parameter is fixed by linear viscoelasticity, is able to predict quantitatively the stresses and to capture all experimental trends of the flows considered so far, with two exceptions: At high shear rates the steady state extinction angle approaches zero rather than a non-zero plateau, and the magnitude of shear and normal stress overshoots during inception of steady shear is overpredicted.

The model has been thoroughly tested in several shearing flows including single-step shear strain (Hua and Schieber, 1998), double-step shear strain (Hua *et al.*, 1998), inception and cessation of steady shear, steady shear (Hua *et al.*, 1999) and exponential shear (Neergaard *et al.*, 2000). In fact, the predictions of the model in exponential shear were conducted as part of the present thesis work (see Chapter 4).

1.3 Thesis Outline

An object of the present thesis work is to gain insight in, by means of stochastic simulations, how the various microscopic dynamics within the reptation picture affect each other and the macroscopic rheological properties. For this purpose it is essential to use a model, which contains all the dynamical features of interest, while providing results without introducing mathematical approximations that might obscure the outcome.

Therefore, more simulations are made with the full-chain model mentioned above (see Section 1.2.9), which appears to be among the most complete of existing reptation models. Except for some equilibrium cases, the simulations all involve shear flows, which from a theoretical point of view are the most challenging due to the implicated vorticity effects.

By developing an improved physical understanding of the polymer chain motion on the molecular level, the goal is to identify shortcomings in the existing reptation theory, and to possibly overcome such shortcomings by refining the theory for linear entangled polymers.

In **Chapter 2** we consider linear viscoelasticity. A relaxation spectrum is found for the test fluid, which is a concentrated solution of nearly monodisperse polystyrene in tricresyl phosphate, that serves as a model system for polymer melts of entangled linear chains. The relaxation spectrum is found from both small-amplitude oscillatory shear flow and from

stress relaxation following small-step shear strain flow. The spectrum exhibits a plateau at moderate time constants, and a downturn at large time constants, whereas the Doi-Edwards model exhibits the opposite trend. Using the full-chain model we study the qualitative impact on the relaxation spectrum, of including chain-length fluctuations and constraint release in the theory, and find that both effects are necessary to describe the linear viscoelasticity even for monodisperse systems.

Chapter 3 deals with steady shear flows; inception of steady shear, steady state shear and relaxation following cessation of steady shear are the specific cases considered. Here, we look into the relationships between macroscopically observed rheological properties and dynamics on the molecular level within the picture of the full-chain reptation model. The effects of chain tumbling, molecular chain stretching and constraint release are discussed, and the distribution of monomers along the chain contour is investigated. Finally, we consider a possible violation of the stress-optic rule during start up of steady shear flow at high shear rates.

The topic of **Chapter 4** is exponential shear. Here, the full-chain model is used to interpret data obtained from exponential shear flow of the same entangled polystyrene solution as mentioned above. Guided by the model, which contains well known dynamics, we are able to explain all trends seen in the data, and a novel analysis of the data is suggested. This analysis demonstrates that exponential shearing flow is no more capable of stretching polymer chains than is inception of steady shear at comparable instantaneous shear rates.

In **Chapter 5** a new full-chain, temporary network model is proposed for nonlinear flows of linear, entangled polymeric liquids. The model is inspired by the full-chain reptation model and its properties as observed in the previous chapters of the thesis. However, the new model contains no tubes and uses a different smaller set of dynamic variables: the location of each entanglement, and the number of Kuhn steps in chain strands between entanglements. In the language of reptation, the model exhibits chain connectivity, chain-length fluctuations, chain stretching, and tube dilation. We describe a simulation algorithm in detail and present some linear viscoelastic predictions of the model. A problem with the free energy expressions, when performing flow calculations, is discussed, and an alternative expression for the free energy is suggested, before some shear flow simulations are made. Finally, we discuss options for future work and possible generalizations of the proposed theory.

Chapters 2 – 5 have been written in the format of scientific articles containing separate abstracts, conclusions and bibliographies to rationalize the process of subsequent publishing in scientific journals.

References

Bird, R. B.; Curtiss, C. F.; Armstrong, R. C. and Hassager, O. (1987). *Dynamics of Polymeric Liquids Vol. II: Kinetic Theory*. Wiley-Interscience, New York, second edition.

de Gennes, P.-G. (1971). Reptation of a polymer chain in the presence of fixed obstacles. *J. Chem. Phys.*, **55**, 572–579.

des Cloizeaux, J. (1988). Double reptation vs. simple reptation in polymer melts. *Europhys. Lett.*, **5**, 437–442.

Doi, M. (1980a). Stress relaxation of polymeric liquids after double step strain. *J. Polym. Sci., Polym. Phys. Ed.*, **18**, 1891–1905.

Doi, M. (1980b). A constitutive equation derived from the model of Doi and Edwards for concentrated polymer solutions and polymer melts. *J. Polym. Sci., Polym. Phys. Ed.*, **18**, 2055–2067.

Doi, M. (1983). Explanation for the 3.4-power law for viscosity of polymeric liquids on the basis of the tube model. *J. Polym. Sci., Polym. Phys. Ed.*, **21**, 667–684.

Doi, M. and Edwards, S. F. (1978a). Dynamics of concentrated polymer systems part 1. Brownian motions in the equilibrium state. *J. Chem. Soc. Faraday Trans. II*, **74**, 1789–1800.

Doi, M. and Edwards, S. F. (1978b). Dynamics of concentrated polymer systems part 2. Molecular motion under flow. *J. Chem. Soc. Faraday Trans. II*, **74**, 1802–1817.

Doi, M. and Edwards, S. F. (1978c). Dynamics of concentrated polymer systems part 3. The constitutive equation. *J. Chem. Soc. Faraday Trans. II*, **74**, 1818–1832.

Doi, M. and Edwards, S. F. (1979). Dynamics of concentrated polymer systems part 4. Rheological properties. *J. Chem. Soc. Faraday Trans. II*, **75**, 38–54.

Doi, M. and Edwards, S. F. (1986). *The Theory of Polymer Dynamics*. Clarendon Press, Oxford.

Fang, J.; Kröger, M. and Öttinger, H. C. (2000). A thermodynamically admissible reptation model for fast flows of entangled polymers. II. Model predictions for shear and extensional flows. *J. Rheol.*, **44**, 1293–1317.

Geurts, B. J. and Jongschaap, R. J. J. (1988). A new reptation model for the rheological properties of concentrated polymer solutions and melts. *J. Rheol.*, **32**(4), 353–365.

Hassager, O.; Kristiansen, S. B.; Larsen, J. L. and Neergaard, J. (1999). Inflation and Instability of a Polymeric Membrane. *J. Non-Newtonian Fluid Mech.*, **88**, 185–204.

Hua, C. C. and Schieber, J. D. (1998). Segment connectivity, chain-length breathing, segmental stretch, and constraint release in reptation models. I. Theory and single-step strain predictions. *J. Chem. Phys.*, **109**(22), 10018–10027.

Hua, C. C.; Schieber, J. D. and Andrews, N. C. (1997). A constant-contour-length reptation model without independent alignment or consistent averaging approximations for chain retraction. *Rheol. Acta*, **36**, 544–554.

Hua, C. C.; Schieber, J. D. and Venerus, D. C. (1998). Segment connectivity, chain-length breathing, segmental stretch, and constraint release in reptation models. II. Double-step strain predictions. *J. Chem. Phys.*, **109**(22), 10028–10032.

Hua, C. C.; Schieber, J. D. and Venerus, D. C. (1999). Segment connectivity, chain-length breathing, segmental stretch, and constraint release in reptation models. III. Shear Flows. *J. Rheol.*, **43**(3), 701–717.

Ianniruberto, G. and Marrucci, G. (1996). On compatibility of the Cox-Merz rule with the model of Doi and Edwards. *J. Non-Newtonian Fluid Mech.*, **65**, 241–246.

Ketzmerick, R. and Öttinger, H. C. (1989). Simulation of a non-Markovian process modeling contour length fluctuation in the Doi-Edwards model. *Continuum Mech. Thermodyn.*, **1**, 113.

Laso, M. and Öttinger, H. C. (1993). Calculation of viscoelastic flow using molecular models: the CONNFFESSIT approach. *J. Non-Newtonian Fluid Mech.*, **47**, 1–20.

Liu, Y.; Shaw, M. T. and Tuminello, W. H. (1998). Obtaining molecular-weight distribution information from the linear viscosity data of linear polymer melts. *J. Rheol.*, **42**(3), 453–476.

Marrucci, G. (1986). The Doi-Edwards model without independent alignment. *J. Non-Newtonian Fluid Mech.*, **21**, 329–336.

Marrucci, G. (1996). Dynamics of entanglements: A nonlinear model consistent with the Cox-Merz rule. *J. Non-Newtonian Fluid Mech.*, **62**, 279–289.

Marrucci, G. and Grizzuti, N. (1986). The Doi-Edwards model in slow flows. Predictions on the Weissenberg effect. *J. Non-Newtonian Fluid Mech.*, **21**, 319–328.

Marrucci, G. and Grizzuti, N. (1988). Fast flows of concentrated polymers: Predictions of the tube model on chain stretching. *Gazzetta Chimica Italiana*, **118**, 179–185.

Mead, D. W. (1994). Determination of molecular weight distributions of linear flexible polymers from linear viscoelastic material functions. *J. Rheol.*, **38**(6), 1797–1827.

Mead, D. W. (1996). Component predictions and the relaxation spectrum of the double reptation mixing rule for polydisperse linear flexible polymers. *J. Rheol.*, **40**, 633–661.

Mead, D. W. and Leal, L. G. (1995). The reptation model with segmental stretch I. Basic equations and general properties. *Rheol. Acta*, **34**, 339–359.

Mead, D. W.; Yavich, D. and Leal, L. G. (1995). The reptation model with segmental stretch II. Steady flow properties. *Rheol. Acta*, **34**, 360–383.

Mead, D. W.; Larson, R. G. and Doi, M. (1998). A molecular theory for fast flows of entangled polymers. *Macromolecules*, **31**, 7895–7914.

Milner, S. T. and McLeish, T. C. B. (1997). Parameter-Free Theory for Stress Relaxation in Star Polymer Melts. *Macromolecules*, **30**, 2159–2166.

Milner, S. T. and McLeish, T. C. B. (1998). Reptation and Contour-Length Fluctuations in Melts of Linear Polymers. *Phys. Rev. Letters*, **81**(3), 725–728.

Neergaard, J.; Park, K.; Venerus, D. C. and Schieber, J. D. (2000). Exponential Shear Flow of Linear, Entangled Polymeric Liquids. *J. Rheol.*, **44**(5), 1043–1054.

Öttinger, H. C. (1994). Modified reptation model. *Phys. Rev. E*, **50**, 4891–4895.

Öttinger, H. C. (1996). *Stochastic Processes in Polymeric Fluids*. Springer, Berlin.

Öttinger, H. C. (1999a). A thermodynamically admissible reptation model for fast flows of entangled polymers. *J. Rheol.*, **43**, 1461–1493.

Öttinger, H. C. (1999b). Nonequilibrium thermodynamics – A tool for applied rheologists. *Appl. Rheol.*, **9**, 17–26.

Öttinger, H. C. and Beris, A. N. (1999). Thermodynamically consistent reptation model without independent alignment. *J. Chem. Phys.*, **110**, 6593–6596.

Pearson, D. S.; Herbolzheimer, E. A.; Marrucci, G. and Grizzuti, N. (1991). Transient behavior of entangled polymers at high shear rates. *J. Polym. Sci., Polym. Phys. Ed.*, **29**, 1589–1597.

Tsenoglou, C. (1987). Viscoelasticity of binary homopolymer blends. *Am. Chem. Soc. Polym. Preprints*, **28**, 185.

Tuminello, W. H. (1986). Molecular weight and molecular weight distribution from dynamic measurements of polymer melts. *Polym. Eng. Sci.*, **26**(19), 1339–1347.

Wasserman, S. H. (1995). Calculating the molecular weight distribution from linear viscoelastic response of polymer melts. *J. Rheol.*, **39**(3), 601–625.

2

Linear Viscoelastic Predictions of a Full-Chain Reptation Model with Chain-Length Fluctuations and Constraint Release

A recently proposed self-consistent reptation model—already successful at describing highly nonlinear shearing flows of many types using one adjustable parameter—is used here to interpret the linear viscoelasticity of the same entangled polystyrene solution. Using standard techniques, a relaxation spectrum is found for the entangled solution from both small-amplitude oscillatory shear flow and from stress relaxation following small step shear strain flow. The spectrum exhibits a plateau at moderate time constants, and a downturn at large time constants. The classical reptation picture, however, exhibits the opposite trend. Using the newly proposed model, we can switch on (or off) dynamics not included in the classical Doi-Edwards model: chain-length fluctuations and constraint release. We find that chain-length fluctuations are important to describe the plateau, and that incorporation of constraint release leads to the observed downturn. Constraint release has already been shown to be important in nonlinear flows and for polydisperse systems, but is clearly shown here to be necessary to describe the linear viscoelasticity of monodisperse systems. [1]

2.1 Introduction

Apparently, it is not widely known that the classical Doi-Edwards reptation model (Doi and Edwards, 1986) for polymer melts is incapable of describing the relaxation spectrum of polymer melts. It is, however, recognized that the width of the relaxation modulus is too narrow; it is often assumed that a proper account of polydispersity in the model will broaden the width sufficiently, and provide quantitative agreement with experiments. However, we show here that it is not only a quantitative

[1] This part of the work has been submitted for publication in *Macromolecules* (2001).

problem in the width of the distribution, but also a qualitative problem with the *trend* of the relaxation spectrum.

It is common to fit the relaxation modulus $G(t)$ of a polymer liquid to a sum of exponentials

$$G(t) = \sum_i g_i \exp(-t/\lambda_i), \tag{2.1}$$

where t is time, $\{g_i\}$ is a set of weighting factors, and $\{\lambda_i\}$ are the corresponding time constants. The fit may be performed either directly on $G(t)$ data obtained from step-strain measurements, or on data of its Fourier transform $G^*(\omega) = G'(\omega) + i\, G''(\omega)$ obtained from small-amplitude oscillatory shear measurements. Here,

$$G'(\omega) = \sum_i \frac{g_i(\lambda_i\omega)^2}{1+(\lambda_i\omega)^2}, \quad G''(\omega) = \sum_i \frac{g_i\lambda_i\omega}{1+(\lambda_i\omega)^2}, \tag{2.2}$$

are the storage and loss moduli, respectively, and ω is the frequency of oscillation. Alternatively, one may fit the relaxation modulus to a continuous weighting function of the relaxation times, $h(\lambda)$, in which case Eqs. (2.1) and (2.2) become

$$G(t) = \int_0^\infty h(\lambda) \exp(-t/\lambda) d\ln\lambda, \tag{2.3}$$

and

$$G'(\omega) = \int_0^\infty \frac{h(\lambda)\ (\lambda\omega)^2}{1+(\lambda\omega)^2} d\ln\lambda, \quad G''(\omega) = \int_0^\infty \frac{h(\lambda)\ \lambda\omega}{1+(\lambda\omega)^2} d\ln\lambda, \tag{2.4}$$

respectively. Performing these fits has been the subject of much research (Honerkamp and Weese, 1993; Mead, 1994a), but we are not interested in that question here; we will assume that such a fit is readily available. For our purposes, only trends are important, not actual values, so our results are not sensitive to the particular fitting method.

The Doi-Edwards reptation model predicts a specific form for the relaxation modulus in Eq. (2.1)

$$G(t) = G_N \sum_{k,\ \mathrm{odd}} \frac{8}{k^2\pi^2} \exp\left(-\frac{tk^2}{\tau_\mathrm{d}}\right), \tag{2.5}$$

where τ_d is the "reptation time" of the polymer, and G_N is the plateau modulus. Thus, we see that the Doi-Edwards model predicts that, as the time constant $\lambda_k \equiv \tau_\mathrm{d}/k^2$ goes up ($k \downarrow$), the weight factor $g_k \equiv 8G_N/(\pi^2k^2)$ also rises.

However, experimental data show the opposite trend. As we show below (see Figure 2.3), it is typical for the weight factors to show a decrease with time constant at small values for λ_i, a plateau in the middle, followed by a strong drop at large values. Polydispersity is unlikely to fix this problem.

Recent theoretical work has shown the importance of dynamical relaxation mechanisms not included in the Doi-Edwards model (Ketzmerick and Öttinger, 1989; Pearson *et al.*, 1991; Ianniruberto and Marrucci, 1996; Hua and Schieber, 1998; Mead *et al.*, 1998; Hua *et al.*, 1998, 1999; Öttinger, 1999). For example, chain stretching is important to predict the overshoots observed in first normal stresses during inception of steady shear (Pearson *et al.*, 1991; Hua *et al.*, 1999). Or, convective constraint release was found to be important in predicting the power-law region in shear stresses during steady shearing flow (Ianniruberto and Marrucci, 1996; Hua *et al.*, 1999). However, these effects are important only during fast deformation flows, and not at equilibrium.

Two other relaxation mechanisms are known to be important at equilibrium. First, chain-length fluctuations have been understood as important to predict the proper scaling relationship between zero-shear-rate viscosity and molecular weight (Doi and Edwards, 1986; Ketzmerick and Öttinger, 1989). Therefore, this physical effect might also be important to predict the proper relaxation modulus—another "zero-shear-rate" property. Secondly, recent successes in using linear viscoelasticity experiments to predict molecular weight distributions have relied heavily on the idea of "double reptation" or constraint release (Tuminello, 1986; Mead, 1994b; Wasserman, 1995; Liu *et al.*, 1998).

Therefore, it would be important to check if these effects can explain the current discrepancy between the reptation picture and experimental results in linear viscoelasticity.

In order to perform this check, it is necessary to use a generalized reptation model. Currently, there are several different thrusts to advance reptation models to include these effects. One such thrust, exploited by several different groups (Pearson *et al.*, 1991; Mead *et al.*, 1998), uses coupled deterministic equations to describe nonlinear flows. These works add no new adjustable parameters, but have not been checked for thermodynamic consistency. Unfortunately for our concerns here, these works put several of the effects in by hand, including the relaxation modulus—albeit without adding new parameters. Hence, they may not be used for our proposed check.

The most recent work, by Öttinger (1999), uses a stochastic dynamics (Fokker-Planck Equation) for a single segment. The model does use adjustable parameters, but these are bound by checks on thermodynamic consistency. Unfortunately here, chain-length fluctuations are not included in the theory, and no binary chain-chain interactions are used to account for constraint release; rather, a heuristic noise term is added to the entanglement dynamics to mimic the effect. Hence, this work is also not useful for such a check.

Therefore, the approach we use is a full-chain stochastic model that has been shown to make very good quantitative comparison with stresses in double-step shear strains (Hua *et al.*, 1998), inception and relaxation

of steady shearing flows, steady shearing flows (Hua *et al.*, 1999), and exponential shear flows (Neergaard *et al.*, 2000). The model includes both chain-length fluctuations, and constraint release—the latter may also be switched off.

The full-chain reptation model contains one phenomenological parameter important at equilibrium: the friction coefficient of a group of monomers. This parameter influences the longest relaxation time; however, for the trends that we are considering here, this parameter is unimportant. Hence, the model provides a good tool to test the assumption of chain-length fluctuations and constraint release in reptation models.

2.2 Experimental System and Model Description

The test fluid is a solution in tricresyl phosphate of nearly monodisperse polystyrene with a molecular weight M_w of 1.9×10^6 (polydispersity index of 1.2) at a polymer concentration n of 0.135 g/cm^3 corresponding to a polymer volume fraction ϕ of approximately 0.13. Extensive data sets in single- and double-step strain flows, inception of steady shear, steady shear, and cessation of steady shear for this fluid have been reported and were found to be in excellent agreement with predictions from the model considered in this study (Venerus and Kahvand, 1994; Hua and Schieber, 1998; Hua *et al.*, 1998, 1999).

All linear viscoelastic data used in this work have been previously reported (Venerus and Kahvand, 1994). Rheological experiments were made using the parallel plate geometry on an RMS-800 at 23°C. Small-amplitude oscillatory shear tests were carried out over five decades of frequency from which the shear storage $G'(\omega)$ and loss $G''(\omega)$ moduli could be obtained using standard methods. The shear stress relaxation modulus $G(t)$ was obtained by monitoring the shear stress following a "step" strain imposed in less than 0.05 s. For both flows, the shear strain amplitude was 0.25, which was sufficiently small to obtain a linear response from the fluid. All reported data are the average of at least two repeat experiments.

The model consists of $N+1$ beads attached by N finitely extendible entropic springs in a constraining tube with Z segments. Therefore, there are $N+1$ dynamic variables describing the monomer density in the tube, and $3Z$ dynamic variables describing the length and orientation of each tube segment. The beads experience frictional forces with the affinely deforming tube, entropic spring forces, and Brownian forces. Dynamics of the chain ends determine death and creation of the tube segments according to the standard reptation picture. In addition, a mean-field constraint release (CR) mechanism similar to that pictured by Tsenoglou (1987) and des Cloizeaux (1988) weakly couples the chains. A Kramers-type expression is used to relate chain dynamics and macroscopic stress. The resulting

expression is closely related to that derived for networks. The reader is referred to earlier papers (Hua and Schieber, 1998; Hua *et al.*, 1998) for more details of the model.

Before simulations begin it is necessary to specify three parameters in the model: $\langle Z\rangle_{\mathrm{eq}}$, the average number of entangled chain segments at equilibrium; $N+1$, the number of beads; and b, the finite extensibility parameter. The first depends upon the chemistry of the chain, and may be found in standard texts (Ferry, 1980; Fetters *et al.*, 1996), based upon molecular weight M_w and entanglement molecular weight M_{e} of the system studied. The second parameter is found from the first as $N = 3\langle Z\rangle_{\mathrm{eq}}$, as before (Hua *et al.*, 1999). b may also be found from standard references, and depends upon entanglement molecular weight M_{e}, and stiffness of the chain as expressed by the characteristic ratio C_∞ (Flory, 1988).

To estimate $\langle Z\rangle_{\mathrm{eq}}$ we use $M_{\mathrm{e}} = 18000$ (Ferry, 1980). To account for the dilution of the entanglements due to the solvent for the polystyrene solution discussed above, we use an empirical result (Graessley and Edwards, 1981) so that

$$\langle Z\rangle_{\mathrm{eq}} = \phi^{1.3}\frac{M_w}{M_{\mathrm{e}}} \approx 7.4. \tag{2.6}$$

An alternative estimate of $\langle Z\rangle_{\mathrm{eq}}$ may be obtained from the scaling relationship by Doi and Edwards (1986)

$$\langle Z\rangle_{\mathrm{eq}} = \frac{1}{3}\frac{\tau_{\mathrm{d}}}{\tau_{\mathrm{R}}} \approx 6.7, \tag{2.7}$$

where $\tau_{\mathrm{R}} = 0.75\,\mathrm{s}$ is the Rouse relaxation time found from the non-factorable part of the relaxation modulus $G(\gamma,t)$ in large-strain step experiments (Venerus and Kahvand, 1994) and $\tau_{\mathrm{d}} = 15\,\mathrm{s}$ is obtained as discussed in the following section. Hence, in this work, we use $\langle Z\rangle_{\mathrm{eq}} = 7$. The finite extensibility parameter, b, is picked to be 150 in all simulations. For $N/\langle Z\rangle_{\mathrm{eq}} = 3$, this value corresponds to 150 Kuhn steps per entanglement molecular weight M_{e}, or 17 monomers per Kuhn step. This value of b is consistent with the experimental system considered, but it actually plays no role in the results here (Flory, 1988).

Extracting simulation results for small-amplitude oscillatory shear flow is difficult because of the very large ensemble sizes needed to avoid excessive statistical noise. Instead, the relaxation modulus is found directly from an equilibrium simulation that exploits linear response theory (Résibois and Leener, 1977). Namely, we find $G(t)$ from the autocorrelation function of the shear stress at equilibrium

$$G(t) = \frac{1}{nkT}\left\langle \tau_{yx}(0)\tau_{yx}(t)\right\rangle_{\mathrm{eq}}, \tag{2.8}$$

where $\langle\ldots\rangle_{\mathrm{eq}}$ indicates taking an average over a large ensemble of chains at equilibrium. As pointed out by Hütter and Öttinger (1996), mean-field models may require modification of this equation. However, a comparison with step-strain simulations confirms the results using Eq. (2.8).

2.3 Results

We want to make comparisons between the data available from small-amplitude oscillatory shear and small step strain shear flow experiments, and compare these results to simulations of shear stress relaxation. In order to do so, however, we need to normalize the results in a way suitable for both kind of experiments and the simulations.

A reasonable estimate for τ_d is the mean relaxation time, τ_m, which can be estimated from the zero-shear-rate viscosity η_0 and the zero-shear-rate first normal stress coefficient $\Psi_{1,0}$ as $\tau_m = \Psi_{1,0}/2\eta_0$. From steady shear experiments for the polystyrene solution (Venerus and Kahvand, 1994) we have $\eta_0 = 6800$ Pa s, $\Psi_{1,0} = 200000$ Pa s^2 which yields a mean relaxation time τ_m of 15 s. Therefore, for all experimental results $\tau_d = 15$ s, which we will use subsequently for normalization of all time scales. The zero-shear-rate properties may also be estimated from the spectrum fit to linear viscoelastic data as $\eta_0 = \sum_i g_i\lambda_i$, $\Psi_{1,0} = 2\sum_i g_i\lambda_i^2$ which provides a consistency-check between linear viscoelastic and steady shear experiments. The latter approach also allows us to relate the time scales of the test fluid to those of the simulations. For the spectrum fit to the simulation with constraint release (Table 2.3) we obtain $\eta_0 = \sum_i g_i\lambda_i \approx 0.298\, nkT\langle Z\rangle_{eq}\tau_d$, $\Psi_{1,0} = 2\sum_i g_i\lambda_i^2 \approx 0.637\, nkT\langle Z\rangle_{eq}\tau_d^2$ which gives an estimated mean relaxation time of $\tau_m \approx 1.068\,\tau_d$.

The plateau modulus G_N is a natural choice for normalization of stresses and moduli. However, the definition of this quantity is somewhat arbitrary because G_N is not easy to assess neither experimentally nor by means of the simulations made in this work. The arbitrariness is due to the very fast initial relaxation mechanisms which occur on time scales much shorter than the Rouse time of the fluid. With our experimental setup, it is not possible to measure this initial fluid response because of the finite duration of the applied shear step strain, and the fast dynamics, which may be associated with lateral chain motion within the confining tube, are not accounted for in the full chain reptation model. Nevertheless, neglecting the very fast relaxation mechanisms, the shear stress relaxation modulus $G(t)$ initially takes the value of the plateau modulus G_N. Hence, we estimate the plateau modulus as $G_N \equiv G(0) = \sum_i g_i = 2480$ Pa, where $\{g_i\}$ is the set of weights from the fit to the shear stress relaxation experiment. Similarly, for the simulations we fix the plateau modulus as $G_N \equiv nkT\langle Z\rangle_{eq}\sum_i g_i$.

2.3.1 Experimental

Measured values of the shear storage and loss moduli (Venerus and Kahvand, 1994) are shown in Figure 2.1. Using a modified CONTIN algorithm (Provencher, 1982; Mead, 1994a), these data points are fit to Eq. (2.2), and the results are shown in Table 2.1. Using this set of $\{g_i, \lambda_i\}$, the storage and loss moduli are recalculated, and the results are shown as the

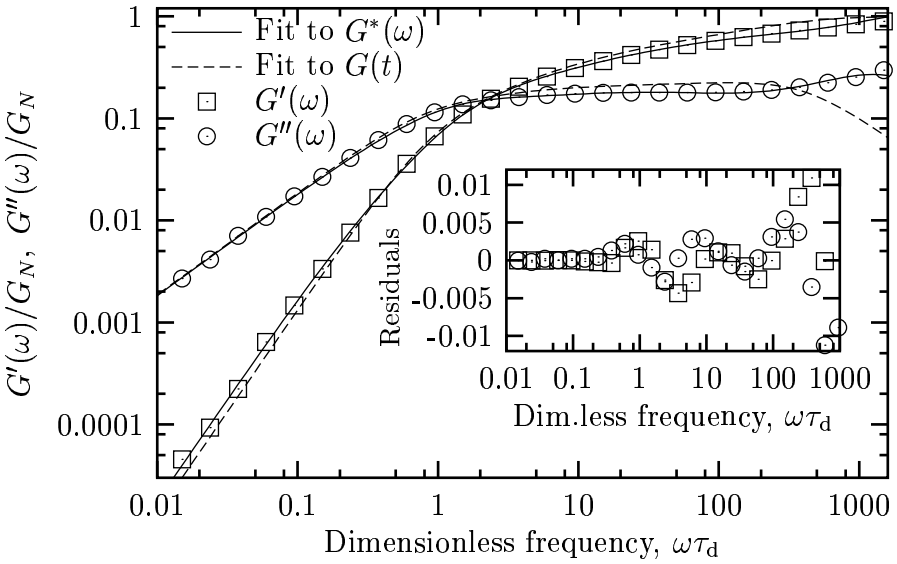

Figure 2.1. Measured storage (squares) and loss (circles) moduli versus frequency. The solid lines are calculated from the relaxation spectrum in Table 2.1, which was fit to the measured $G'(\omega)$, $G''(\omega)$ values (the inset shows the residuals for this fit, $[G^*_{\text{data}}(\omega) - G^*_{\text{fit}}(\omega)]/G_N$). The dashed lines are calculated from the relaxation spectrum in Table 2.2, which was fit to the measured $G(t)$ data shown in Figure 2.2.

solid lines in Figure 2.1. The fit is excellent, as seen in the inset residuals plot, except perhaps at the highest frequencies. From the spectrum in Table 2.1 fit to oscillatory shear data we obtain an estimated mean relaxation time $\tau_m \approx 15\,s$ which compares well with the above τ_m value based on steady shear data. Note, that due to improvement of the fitting algorithm utilized in the present work the spectrum in Table 2.1 differs slightly from the one previously reported on the same data set (Venerus and Kahvand, 1994).

Time const, λ_i/τ_d	Weight, g_i/G_N	Standard error
0.00066667	0.45263	0.019348
0.0021082	0.081475	0.015721
0.0066667	0.097847	0.012093
0.021082	0.146124	0.012093
0.066667	0.138292	0.012496
0.21082	0.112929	0.011690
0.66667	0.162938	0.007256
2.1082	0.015436	0.002177
6.6667	0.0006678	0.0002177

Table 2.1. Discrete relaxation spectrum fit to the $G^*(\omega)$ data in Figure 2.1.

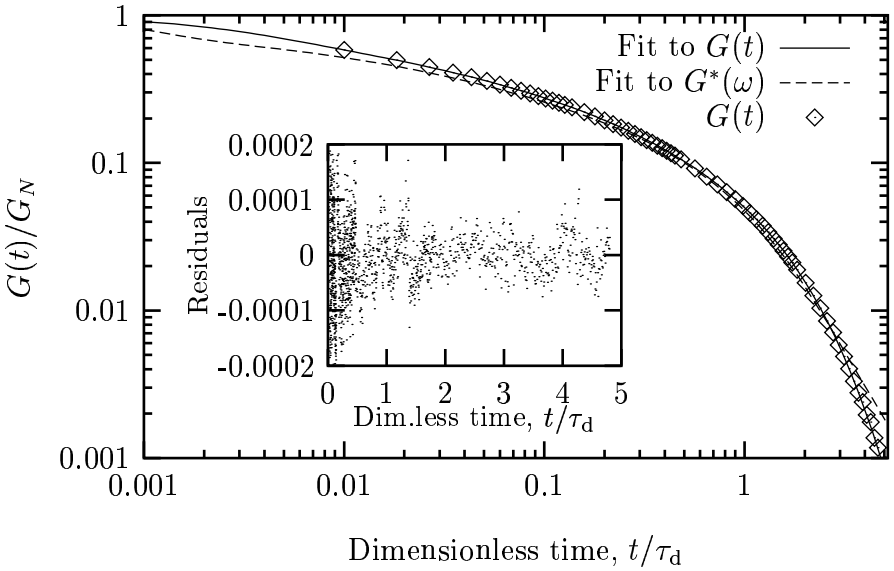

Figure 2.2. Measured relaxation modulus versus time. The solid line is calculated from the relaxation spectrum in Table 2.2, which was fit to the measured $G(t)$ values (the inset are the residuals for this fit, $[G_{\text{data}}(t) - G_{\text{fit}}(t)]/G_N$). The dashed line is calculated from the relaxation spectrum in Table 2.1, which was fit to the measured $G^*(\omega)$ data shown in Figure 2.1.

Shear stress relaxation modulus data (Venerus and Kahvand, 1994) are shown in Figure 2.2. Results of a fit of Eq. (2.1) to these data using the CONTIN algorithm (Provencher, 1982; Mead, 1994a) are shown in Table 2.2. Using this relaxation spectrum, the relaxation modulus is recalculated, and the result is plotted as the solid line in Figure 2.2. Again, the inset residuals plot indicates a satisfactory fit. Considering the number of available data points, it is not surprising that the residuals for the fit to stress relaxation data (Figure 2.2) are much smaller than those for the fit to the oscillatory shear results (Figure 2.1). Calculating the mean relaxation time from the spectrum in Table 2.2 fit we get $\tau_m \approx 11$ s which is comparable with the steady shear data value found above.

Time const, λ_i/τ_d	Standard error	Weight, g_i/G_N	Standard error
0.0030992	0.00017794	0.25475	0.02337
0.0095747	0.0002509	0.165860	0.003676
0.030281	0.0006211	0.152276	0.0016091
0.086320	0.002480	0.132895	0.002123
0.22456	0.006986	0.128126	0.0019663
0.62580	0.02808	0.093904	0.003302
1.10906	0.02038	0.072194	0.006482

Table 2.2. Discrete relaxation spectrum fit to the $G(t)$ experimental data shown in Figure 2.2.

As a consistency-check on these experiments, the spectrum from $G(t)$ data is used to predict $G^*(\omega)$, and vice-versa. The results are also shown in Figures 2.1 and 2.2 as dashed lines. We find that the storage and loss moduli are described rather well by the fit to the relaxation modulus data, except at the highest frequencies. The reverse comparision is not as good, but is still satisfactory. However, these small discrepancies are not important for our study, as we see in the next figure (Figure 2.3) that the relaxation spectra measured from these two methods show similar trends.

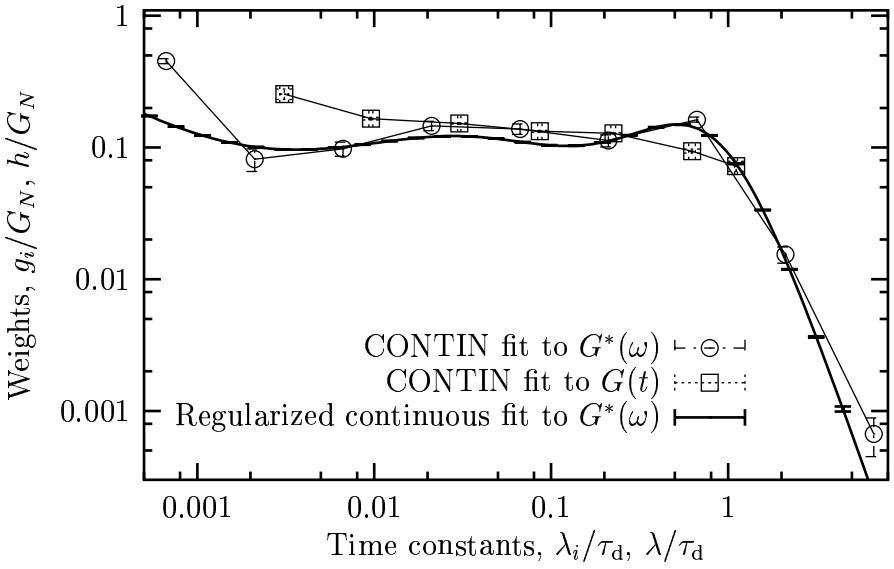

Figure 2.3. Discrete and continuous relaxation spectra for the $G^*(\omega)$ experiment and discrete relaxation spectrum for the $G(t)$ experiment. The included errorbars are almost all smaller than the size of the symbols.

We compare the discrete relaxation spectrum (unfilled symbols) for the $G^*(\omega)$ and $G(t)$ experiment in Figure 2.3 which shows the weights, g_i/G_N, plotted versus the time constants, λ_i/τ_d. The spectra are fit to the data using the CONTIN algorithm (Provencher, 1982; Mead, 1994a) and we note that the included error bars (also listed in Table 2.1 - 2.2) are about the same size or smaller than the symbols in the figure. It is seen, that there is good agreement between the spectra obtained from the different experiments although the decrease for large λ_i is not as pronounced for the $G(t)$ spectrum.

Also shown in Figure 2.3 (solid line) is a fit of the $G^*(\omega)$ data to Eq. (2.4), the continuous relaxation spectrum, h/G_N, which is obtained by means of a nonlinear regularization method (Honerkamp and Weese, 1993). The error bars for this fit are almost everywhere comparable to the thickness of the line and are therefore hardly visible in the figure. We see that the continuous and discrete spectrum for the $G^*(\omega)$ data compare very well except at the smallest time scales. This leads us to conclude that

the spectra considered in the remainder of this paper are independent of the particular fitting method used, at least for our purposes where only qualitative trends are important.

2.3.2 Theory

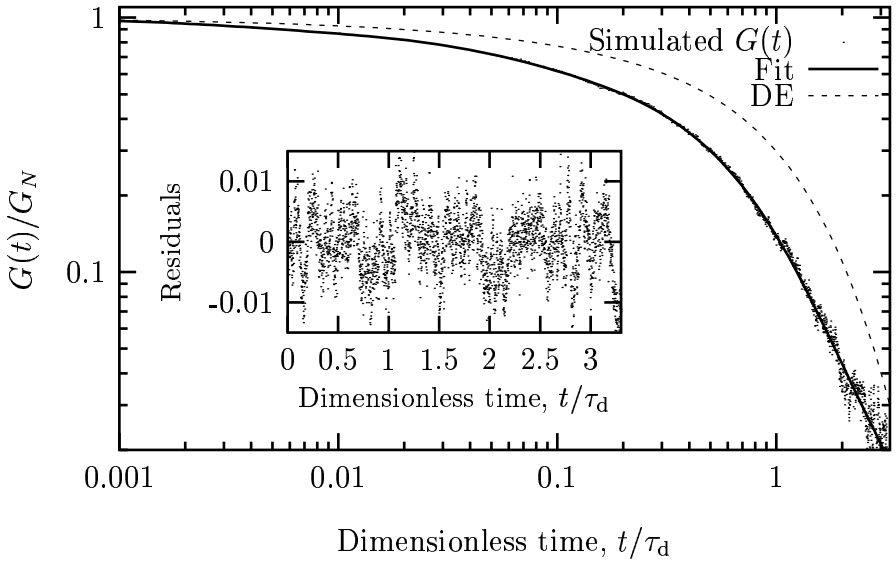

Figure 2.4. Relaxation modulus as a function of time predicted by the full-chain reptation model *with* constraint release (points). The solid line is the fit to these data – the relaxation spectrum given in Table 2.3. The inset shows the residuals for this fit, $[G_{\rm sim}(t) - G_{\rm fit}(t)]/G_N$. The dashed line is the prediction of $G(t)$ by the Doi-Edwards model (DE).

The relaxation modulus extracted from the linear response simulation including constraint release is shown in Figure 2.4. These results are fit to Eq. (2.1) and the relaxation spectrum using the CONTIN algorithm (Provencher, 1982; Mead, 1994a) is given in Table 2.3. Recalculating the relaxation modulus from this spectrum results in the solid line shown in Figure 2.4. The fit is excellent, as shown in the inset residuals plot. We may also switch off the constraint-release mechanism in the simulations

Time const, λ_i/τ_d	Standard error	Weight, g_i/G_N	Standard error
0.0030954	0.0004732	0.087126	0.008159
0.047955	0.0010604	0.20860	0.002518
0.51891	0.003926	0.63049	0.003144
2.2252	0.09639	0.073777	0.004112

Table 2.3. Discrete relaxation spectrum fit to the $G(t)$ simulation results *with* constraint release.

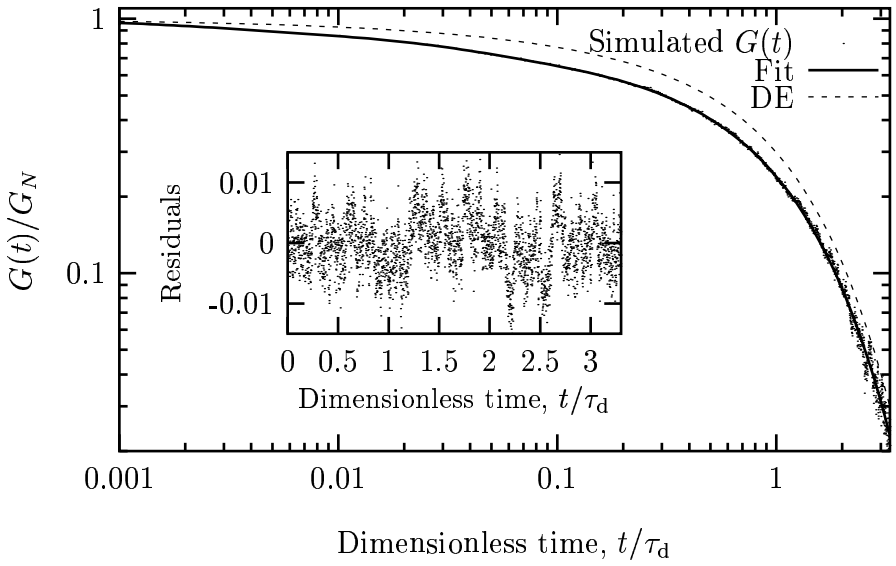

Figure 2.5. Relaxation modulus as a function of time predicted by the full-chain reptation model *without* constraint release (points). The solid line is the fit to these data – the relaxation spectrum given in Table 2.4. The inset are the residuals for this fit, $[G_{\rm sim}(t) - G_{\rm fit}(t)]/G_N$. The dashed line is the prediction of $G(t)$ by the Doi-Edwards model (DE).

and repeat the procedure: simulate $G(t)$, find the relaxation spectrum, and compare the results. These are shown in Figure 2.5 and Table 2.4; again, the agreement is excellent, so we have confidence in the fit.

The dashed lines in Figures 2.4 and 2.5 are the prediction of $G(t)$ by the Doi-Edwards reptation model as given in Eq. (2.5). In Figure 2.5 it is found that the full chain reptation model without constraint release broadens the relaxation modulus compared to that of the Doi-Edwards model. Simulation of stress relaxation following a shear step strain using a full chain reptation model without chain-length fluctuations (Hua *et al.*, 1997) resulted in a relaxation modulus identical to $G(t)$ predicted by the Doi-Edwards model. Thus, the observed broadening, which brings $G(t)$ in closer agreement with the experimental data, can be attributed to the chain-length fluctuations included in the present model. Using the pre-

Time const, λ_i/τ_d	Standard error	Weight, g_i/G_N	Standard error
0.0024638	0.0004443	0.091114	0.009587
0.031609	0.0016057	0.161300	0.004157
0.165158	0.009607	0.083541	0.003928
0.98174	0.0015276	0.66404	0.0014454

Table 2.4. Discrete relaxation spectrum fit to the $G(t)$ simulation results *without* constraint release.

diction of $G(t)$ by the Doi-Edwards model as a reference, comparison between the simulations in Figures 2.4 and 2.5 shows that incorporation of constraint release causes further broadening of the relaxation modulus, bringing it even closer to the experimental data.

2.3.3 Comparison Between Theory and Experiment

A comparison is made of the storage and loss moduli predicted by the theory (using the fit to the relaxation modulus) to experiments in Figure 2.6. However, it is not possible to make a direct, fair comparison between theoretical and experimental results in terms of the normalization of moduli utilized to this point, because of the arbitrariness of G_N discussed above. Instead we employ in this particular plot an empirical relationship for the plateau modulus, $\tilde{G}_N = 3.56 G''_{\max}(\omega)$, which is valid for concentrated systems of monodisperse, linear polymers (Raju *et al.*, 1981). $G''_{\max}(\omega)$ is estimated to be at the crossover for $G'(\omega)$ and $G''(\omega)$. By normalizing all dynamic moduli using $\tilde{G}_N$ rather than G_N, we effectively ensure vertical alignment of $G''_{\max}(\omega)$ for both experimental and theoretical results.

We find that the reptation model both with and without constraint release is not able to predict the data at high frequencies. This is not surprising, since the model is a coarse-grained object. Namely, the model is an elastic chain confined to the contours of a tube. Hence, fluctuations in

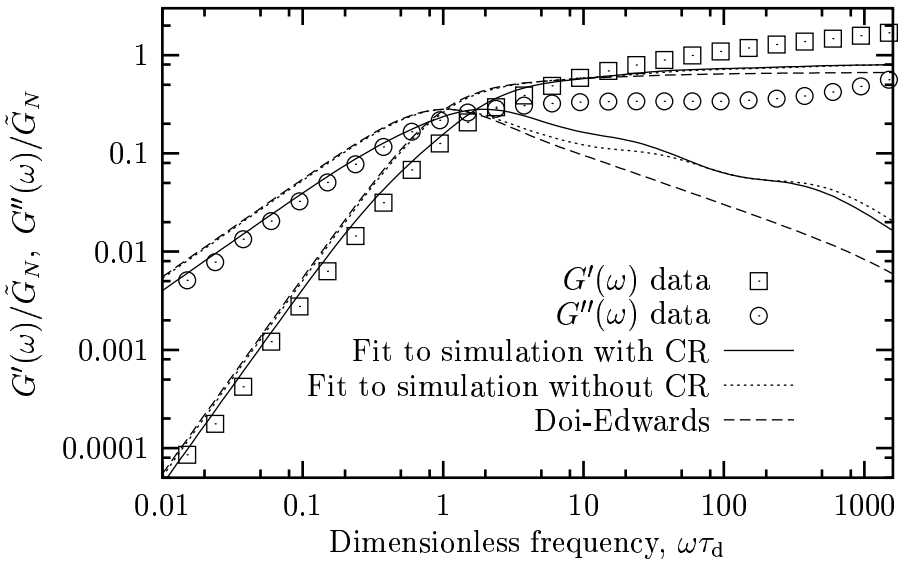

Figure 2.6. A comparison between the experimentally measured storage (squares) and loss (circles) moduli and the same quantities predicted by the model with (solid lines) and without (dotted lines) constraint release. Also shown is the prediction by the Doi-Edwards model (dashed lines). In this figure, all plateau moduli are estimated from the empirical relation $\tilde{G}_N \approx 3.56\, G''_{\max}(\omega)$ (Raju *et al.*, 1981).

the conformation of the chain perpendicular to the tube centerline are not accounted for in the theory. Such fluctuations presumably occur on time scales more rapid than reptation, chain-length fluctuations or constraint release. Secondly, however, we note that switching on constraint release improves the model's ability to describe the data at low to intermediate frequencies.

In Figure 2.7 we compare the relaxation spectrum predicted by the model (filled symbols) with that found for the test fluid (unfilled symbols). We only show the spectrum for the $G^*(\omega)$ experiment as we have already shown (see Figure 2.3) that the trends in the relaxation spectrum for the $G^*(\omega)$ and the $G(t)$ experiments are the same. We have also found (see Figure 2.3) that the shape of the spectrum is independent of the particular fitting algorithm used. Hence, for the comparison in Figure 2.7 we consider only the discrete relaxation spectra computed by the CONTIN algorithm. We have not included error bars in this figure, since they are all within the size of the symbols for the spectra predicted by the model. However, the standard deviation of all weights, g_i/G_N, and time constants, $\lambda_i/\tau_\mathrm{d}$, fit by the CONTIN algorithm are listed in Tables 2.1 - 2.4.

Also shown in Figure 2.7 is the prediction of the Doi-Edwards model (dashed lines), which does not include chain-length fluctuations or constraint release. As mentioned above, the prediction of the Doi-Edwards model is qualitatively different from the experimental results. One might argue that the infinite number of closely spaced modes at short times could be grouped into fewer modes with larger weights, and that such a procedure would be expected to bring the Doi-Edwards spectrum in closer

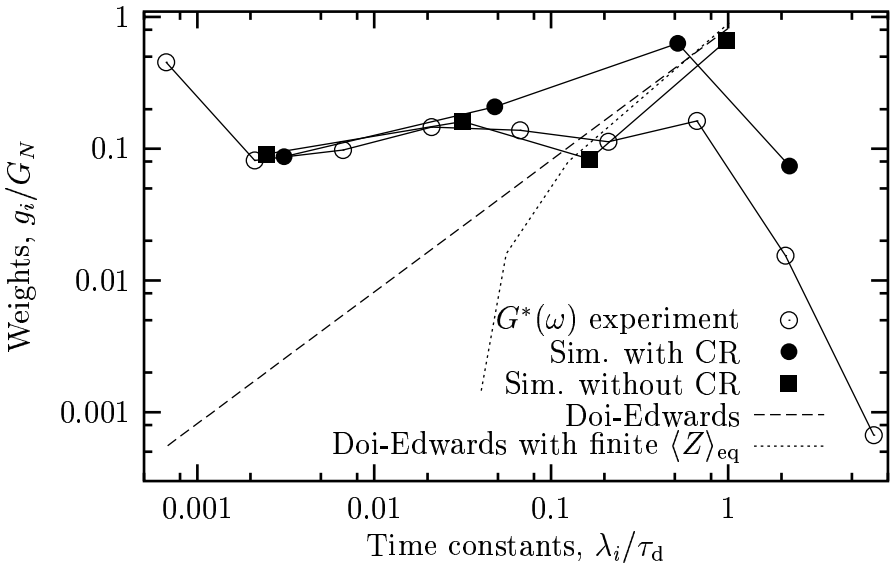

Figure 2.7. The discrete relaxation spectrum for the $G^*(\omega)$ experiment and all models discussed in this paper.

agreement with experiment. However, these modes are actually an artifact of a mathematical approximation used in the Doi-Edwards model, and do not arise from the physics. Namely, the derivation of the Doi-Edwards model assumes that the finite number of entanglements may be approximated by a continuous count along the chain. If this assumption is removed, the predictions actually become worse (dotted line in Figure 2.7) (Schieber, 1990).

On the other hand, the model without constraint release can be seen as allowing chain-length fluctuations to the Doi-Edwards model (filled squares). Here we see that these fluctuations give rise to a plateau in the spectrum—in closer agreement with data. Finally, when we also switch on constraint release (filled circles), we see that the model now also captures the downturn in the relaxation spectrum of the fluid that is observed in experiments. It appears that constraint release introduces a relaxation mechanism with a time scale greater than the reptation time, τ_d.

Finally, in Figure 2.8 we also compare the prediction of the model with the empirical Cox-Merz rule, $\eta(\dot{\gamma}) = |\eta^*(\omega)|$, where $\eta(\dot{\gamma})$ is the steady shear and $|\eta^*(\omega)|$ the complex viscosity. We find that, although the model overpredicts the amount of shear thinning relative to the experiments, it does show consistency with the Cox-Merz rule. For the complex viscosity, the data yields an asymptotic power-law exponent of -0.80 at high frequencies whereas a value of $\lim_{\omega\to\infty} |\eta^*(\omega)| = -0.94$ is obtained from the model with constraint release. The Doi-Edwards model predicts asymptotic power-law exponents of -1.5 and -1.0 for $\lim_{\dot{\gamma}\to\infty} \eta(\dot{\gamma})$ and

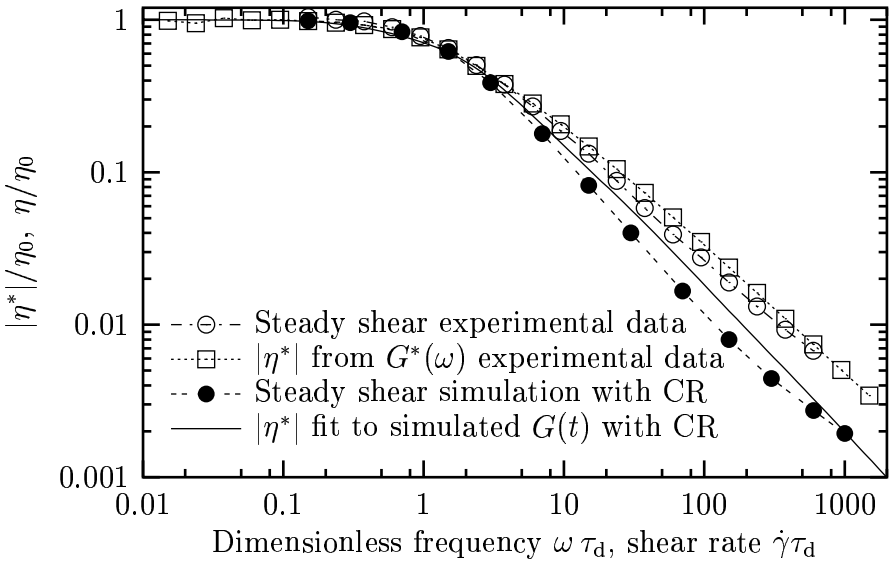

Figure 2.8. A check of the Cox-Merz rule for the full-chain reptation model with constraint release (CR). Experimental data are normalized using $\eta_0 = 6800\,\mathrm{Pa\,s}$ and simulations by $\eta_0 = \sum_i g_i\lambda_i \approx 0.298\,nkT\langle Z\rangle_{eq}\tau_d$.

$\lim_{\omega\to\infty} |\eta^*(\omega)|$ respectively, and thus fails to predict the Cox-Merz rule.

The failure of the Doi-Edwards model to give the Cox-Merz rule can be attributed to the excessive shear thinning which causes a power-law exponent smaller than -1.0. Iannirubertо and Marrucci (1996) showed, however, that by extending the Doi-Edwards model to include convective constraint release, which is important only at high deformation rates, the asymptotic power-law exponent for $\eta(\dot{\gamma})$ is improved to -1.0. Still, they got the asymptotic prediction of the Cox-Merz rule right only within a factor of 2.

The model with constraint release provides good agreement between $\eta(\dot{\gamma})$ and $|\eta^*(\omega)|$ at low and at the highest frequencies/shear rates, whereas small deviations are observed for intermediate frequencies/shear rates. Interestingly, the small deviation of the complex viscosity is in the direction of the experimental data, which also show minor differences between $\eta(\dot{\gamma})$ and $|\eta^*(\omega)|$ at intermediate frequencies/shear rates.

Acknowledgments

One of the authors (J.N.) would like to thank the Danish government for financial support through the Technical University of Denmark (DTU), and Kaj and Hermilla Ostenfeld's fund.

References

des Cloizeaux, J. (1988). Double reptation vs. simple reptation in polymer melts. *Europhys. Lett.*, **5**, 437–442.

Doi, M. and Edwards, S. F. (1986). *The Theory of Polymer Dynamics*. Clarendon Press, Oxford.

Ferry, J. L. (1980). *Viscoelastic Properties of Polymers*. John Wiley & Sons, New York, third edition.

Fetters, L. J.; Lohse, D. J. and Colby, R. H. (1996). Chain dimensions and entanglement spacings. In *Physical Properties of Polymers Handbook*. AIP, New York.

Flory, P. J. (1988). *Statistical Mechanics of Chain Molecules*. Hanser, Munich.

Graessley, W. W. and Edwards, S. F. (1981). Entanglement interactions in polymers and the chain contour concentration. *Polymer*, **22**, 1329–1334.

Honerkamp, J. and Weese, J. (1993). A nonlinear regularization method for the calculation of relaxation spectra. *Rheol. Acta*, **32**, 65–73.

Hua, C. C. and Schieber, J. D. (1998). Segment connectivity, chain-length breathing, segmental stretch, and constraint release in reptation models.

I. Theory and single-step strain predictions. *J. Chem. Phys.*, **109**(22), 10018–10027.

Hua, C. C.; Schieber, J. D. and Andrews, N. C. (1997). A constant-contour-length reptation model without independent alignment or consistent averaging approximations for chain retraction. *Rheol. Acta*, **36**, 544–554.

Hua, C. C.; Schieber, J. D. and Venerus, D. C. (1998). Segment connectivity, chain-length breathing, segmental stretch, and constraint release in reptation models. II. Double-step strain predictions. *J. Chem. Phys.*, **109**(22), 10028–10032.

Hua, C. C.; Schieber, J. D. and Venerus, D. C. (1999). Segment connectivity, chain-length breathing, segmental stretch, and constraint release in reptation models. III. Shear Flows. *J. Rheol.*, **43**(3), 701–717.

Hütter, M. and Öttinger, H. C. (1996). Modification of linear response theory for mean-field approximations. *Phys. Rev. E*, **54**(3), 2526–2530.

Ianniruberto, G. and Marrucci, G. (1996). On compatibility of the Cox-Merz rule with the model of Doi and Edwards. *J. Non-Newtonian Fluid Mech.*, **65**, 241–246.

Ketzmerick, R. and Öttinger, H. C. (1989). Simulation of a non-Markovian process modeling contour length fluctuation in the Doi-Edwards model. *Continuum Mech. Thermodyn.*, **1**, 113.

Liu, Y.; Shaw, M. T. and Tuminello, W. H. (1998). Obtaining molecular-weight distribution information from the linear viscosity data of linear polymer melts. *J. Rheol.*, **42**(3), 453–476.

Mead, D. W. (1994a). Numerical interconversion of linear viscoelastic material functions. *J. Rheol.*, **38**(6), 1769–1795.

Mead, D. W. (1994b). Determination of molecular weight distributions of linear flexible polymers from linear viscoelastic material functions. *J. Rheol.*, **38**(6), 1797–1827.

Mead, D. W.; Larson, R. G. and Doi, M. (1998). A molecular theory for fast flows of entangled polymers. *Macromolecules*, **31**, 7895–7914.

Neergaard, J.; Park, K.; Venerus, D. C. and Schieber, J. D. (2000). Exponential Shear Flow of Linear, Entangled Polymeric Liquids. *J. Rheol.*, **44**(5), 1043–1054.

Öttinger, H. C. (1999). A thermodynamically admissible reptation model for fast flows of entangled polymers. *J. Rheol.*, **43**, 1461–1493.

Pearson, D. S.; Herbolzheimer, E. A.; Marrucci, G. and Grizzuti, N. (1991). Transient behavior of entangled polymers at high shear rates. *J. Polym. Sci., Polym. Phys. Ed.*, **29**, 1589–1597.

Provencher, S. W. (1982). CONTIN: a general purpose constrained regularization program for inverting noisy linear algebraic and integral equations. *Computer Physics Communications*, **27**(3), 229–242.

Raju, V. R.; Menezes, E. V.; Marin, G.; Graessley, W. W. and Fetters, L. J. (1981). Concentration and Molecular Weight Dependence of Viscoelastic Properties in Linear and Star Polymers. *Macromolecules*, **14**, 1668–1676.

Résibois, P. and Leener, M. D. (1977). *Classical Kinetic Theory of Fluids*. John Wiley and Sons, New York.

Schieber, J. D. (1990). The Effect of Finite Bead Number on Reptation Models. *J. Non-Newtonian Fluid Mech.*, **26**, 205–242.

Tsenoglou, C. (1987). Viscoelasticity of binary homopolymer blends. *Am. Chem. Soc. Polym. Preprints*, **28**, 185.

Tuminello, W. H. (1986). Molecular weight and molecular weight distribution from dynamic measurements of polymer melts. *Polym. Eng. Sci.*, **26**(19), 1339–1347.

Venerus, D. C. and Kahvand, H. (1994). Doi-Edwards theory evaluation in double-step strain flows. *J. Polym. Sci., Polym. Phys. Ed.*, **32**, 1531–1542.

Wasserman, S. H. (1995). Calculating the molecular weight distribution from linear viscoelastic response of polymer melts. *J. Rheol.*, **39**(3), 601–625.

3

Dynamics of Linear, Entangled Polymeric Liquids in Shear Flows

We study predictions in transient and steady shearing flows of a previously proposed self-consistent reptation model, which includes chain stretching, chain-length fluctuations, segment connectivity and constraint release. In an earlier paper it was established that the model is able to capture all trends observed experimentally for viscometric flows allowing focus of the present work on the model. That is, we study in detail the physics and underlying dynamics of the model to explain the macroscopically observed rheological properties in terms of chain behavior and dynamics on the molecular level. More specifically, we discuss the effects of chain tumbling, molecular chain stretching and constraint release and their influence on the macroscopic stress as well as the extinction angle under various flow conditions. In particular, we find that chain tumbling causes the undershoot in extinction angle during inception of shear; chain tumbling is itself suppressed by the presence of molecular stretching; and the anticipated strong correlation between normal stress and molecular stretching is confirmed. Also investigated is the monomer density along the chain contour which reveals information about the local chain stretching and orientation. Here, it is found that the distribution of monomers along the contour becomes non-uniform when the shear rate exceeds the inverse Rouse relaxation time. Finally, we discuss a possible violation of the stress-optic rule during start up of steady shear flow at high shear rates. [1]

3.1 Introduction

When Doi and Edwards presented their reptation model (Doi and Edwards, 1978a,b,c, 1979, 1986) to describe the viscoelastic behavior of linear, entangled polymer chains, it was a major breakthrough for constitutive modeling based on the molecular level. However, Doi and Edwards

[1] This part of the work has been submitted for publication in *J. Non-Newtonian Fluid Mech.* (2001).

left out several important dynamics on the molecular level, and made additional assumptions for mathematical convenience in order to obtain analytic results. Consequently, despite its success at predicting certain rheological properties, the Doi-Edwards model (DE) fails to describe even qualitatively several experimentally observed characteristics in various deformations such as shear flows, which are considered in the present work.

Recognizing the limitations of the DE model, it has since been the subject of much research to avoid the approximations originally made and to incorporate the missing microscopic dynamics to improve constitutive modeling within the reptation picture. We give in the following a brief summary of the most important refinements of the DE model considered in order to develop a reptation model that is able to capture as many as possible of the rheological properties in shearing flows.

In the linear viscoelastic limit two effects have been found to be particularly important in improving the predictions of the DE model. Doi (1983) realized that including chain-length fluctuations in the theory was important for the reptation model to predict the correct scaling law for dependence of the longest relaxation time on molecular weight. This was later confirmed by means of equilibrium Brownian dynamics simulations by Ketzmerick and Öttinger (1989). Milner and McLeish (1998) arrived at the same result applying a theory developed for arm retraction in star-molecules (Milner and McLeish, 1997) to reptating linear chains.

The other missing effect in the DE model of importance in the linear viscoelastic limit is to recognize that the tube consists of other reptating chains making it a dynamic object which provides additional relaxation by removing some of the obstacles felt by the test chain. Based on this idea of "double reptation" or constraint release (CR) Tsenoglou (1987) and des Cloizeaux (1988) derived a successful polydispersity mixing rule for the linear viscoelastic regime. The mixing rule was recovered by Öttinger (1994), who incorporated the constraint release mechanism in the DE model by means of a noise term in the time-evolution equation for orientation and, using this model, found an improved value of the shear viscosity power law index.

The assumption of instantaneous chain retraction was first removed by Marrucci and Grizzuti (1988), who modified the DE model to allow for molecular chain stretching and made predictions for steady state shear without finding any improvements. Studying the same type of model, Pearson *et al.* (1991) extended the calculations to transient flows and observed overshoot in both shear stress and first normal stress difference upon start up of steady shear. Onset of the overshoot is predicted to occur at a higher shear rate for the first normal stress difference than for the shear stress in consistency with experimental data, and the predicted strains, at which the stress maxima occur, also agree with experiments.

The convective constraint release mechanism (CCR) was proposed by Marrucci (1996) and Ianniruberto and Marrucci (1996). They argued that

another mechanism contributes to relaxation of chain orientation during flow in addition to ordinary diffusion due to thermal motion (reptation and double reptation). The additional relaxation mechanism is constraint release induced by flow through chain stretching followed by retraction of the chains surrounding the test chain.

Based on the idea of CCR Mead *et al.* (1998) further modified the DE model including chain stretching (Marrucci and Grizzuti, 1988; Pearson *et al.*, 1991; Mead and Leal, 1995; Mead *et al.*, 1995) to obtain a reptation model with segmental stretch, chain-length fluctuations and CCR but without the effect of double reptation and without avoiding the assumption of independent alignment (IA). Nevertheless, the model captures many experimentally observed trends and the authors thus concluded that stretching and CCR are responsible for most discrepancies between predictions of the DE model and experimental data in nonlinear shearing flows.

Öttinger and Beris (1999) recently reformulated the DE model without IA to obtain a thermodynamically admissible reptation model by means of thermodynamic modeling. Using the same approach Öttinger (1999) then derived a reptation model which includes all of the dynamic effects discussed above, except for chain-length fluctuations, while avoiding the IA assumption. The predictions of the resulting single-segment model compare well with experiments capturing most trends observed in nonlinear shearing flows upon appropriate choice of the adjustable model parameters, δ_1 and δ_2 (Fang *et al.*, 2000).

The effect of segment connectivity and all of the microscopic physical effects discussed above have been incorporated in a full-chain model in a self-consistent manner by Hua and Schieber (1998). Their full-chain theory is formulated in terms of a set of stochastic differential equations suitable for numerical simulations utilizing Brownian dynamics, without making any approximations such as IA or consistent averaging. The model, whose lone adjustable parameter is fixed by linear viscoelasticity, is able to predict quantitatively the stresses and to capture all experimental trends of the flows considered with two exceptions: At high shear rates the steady state extinction angle approaches zero rather than a non-zero plateau, and the magnitude of shear and normal stress overshoot during inception of steady shear is overpredicted. The model has been thoroughly tested in several shearing flows including single-step shear strain (Hua and Schieber, 1998), double-step shear strain (Hua *et al.*, 1998), inception and cessation of steady shear, steady shear (Hua *et al.*, 1999) and exponential shear (Neergaard *et al.*, 2000).

The success of the recent reptation models in capturing nearly all rheological properties observed experimentally is very encouraging for future constitutive modeling based on reptation theory. In the current work we revisit the predictions of the full-chain model just mentioned and break down in detail the results in start up of steady shear, steady shear and

following cessation of steady shear. Focus here is solely on the model, since very good comparison of the model predictions with experimental data for the flows under consideration has already been established (Hua *et al.*, 1999). The physics and underlying dynamics of the model are to be studied to explain the macroscopically observed rheological properties in terms of chain behavior and dynamics on the molecular level. While one may have an intuitive feeling for the relationships between microscopic and macroscopic properties, we here offer explicit evidence, within the model picture, of how stress is related to molecular stretching and chain orientation.

In Section 3.2 we present the full-chain model followed by a description of the microscopic effects considered. These include chain tumbling, molecular stretching and the distribution of monomers along the chain contour. Results are given in Section 3.3 along with a discussion of these, and finally we summarize the conclusions made in Section 3.4.

3.2 Theory

3.2.1 The model and its parameters

The model consists of $N+1$ beads attached by N finitely extendible entropic springs in a constraining tube with Z segments. Therefore, there are $N+1$ dynamic variables describing the monomer density in the tube, and $3Z$ dynamic variables describing the length and orientation of each tube segment. The beads experience frictional forces with the affinely deforming tube, entropic spring forces, and Brownian forces. Dynamics of the chain ends determine creation and destruction of the tube segments according to the standard reptation picture. Thus, the effects of segment connectivity, segmental stretch and chain-length fluctuations are incorporated in the model in a self-consistent manner, since they are all implied by the mechanical model. In addition, a self-consistent, mean-field constraint release mechanism similar to that pictured by Tsenoglou (1987) and des Cloizeaux (1988) weakly couples the chains. The constraint release mechanism (CR) is switched on for most of the cases, otherwise to be mentioned. To relate chain dynamics and macroscopic stress a Kramers-type expression is used, which is closely related to that derived for networks (Bird *et al.*, 1987). The reader is referred to earlier papers (Hua and Schieber, 1998; Hua *et al.*, 1999) for more details on the model.

Before simulations begin it is necessary to specify three parameters in the model: $\langle Z\rangle_{\mathrm{eq}}$, the average number of entangled chain segments at equilibrium; $N+1$, the number of beads; and b, the finite extensibility parameter. The first depends upon the chemistry of the chain, and may be found in standard texts (Ferry, 1980; Fetters *et al.*, 1996), based upon molecular weight M_w and entanglement molecular weight M_{e} of the system studied. The second parameter is found from the first as $N = 3\langle Z\rangle_{\mathrm{eq}}$, as

before (Hua *et al.*, 1999). The finite extensibility parameter b may also be found from standard references, and depends upon entanglement molecular weight M_e, and stiffness of the chain as expressed by the characteristic ratio C_∞ (Flory, 1988).

In this work, we use $\langle Z \rangle_{eq} = 7$, which is the same value as previously used when studying shear flow predictions of the model (Hua *et al.*, 1999). This is also reasonably consistent with the value estimated for the entangled polystyrene solution (Venerus and Kahvand, 1994) which has been used to quantitatively validate the model (Hua *et al.*, 1998, 1999; Neergaard *et al.*, 2000). The finite extensibility parameter, b, is picked to be 150 in all simulations. For $N/\langle Z \rangle_{eq} = 3$, this value corresponds to 150 Kuhn steps per entanglement molecular weight M_e, or 17 monomers per Kuhn step. This value of b is consistent with the experimental system considered (Flory, 1988, p.39). Too small of a value was used by Hua *et al.* (1999); however, the results given previously and in the present work are not sensitive to finite extensibility, as comparison with $b = \infty$ results has shown.

From an equilibrium simulation, the single adjustable parameter can be found: the disengagement time, τ_d. Therefore, for all nonlinear flow calculations, the model contains no adjustable parameters.

3.2.2 Microscopic dynamics considered

The dynamic features on the molecular level, to which we pay special attention in this work, are described in the following.

A reasonable measure of the average chain orientation is the extinction angle, χ, which in fact is a macroscopic quantity that can be measured directly from birefringence experiments. In terms of the model the extinction angle is obtained from the simulated stresses as

$$\chi = \frac{1}{2} \tan^{-1} \left(\frac{2\tau_{yx}}{\tau_{xx} - \tau_{yy}} \right), \tag{3.1}$$

in which τ_{yx} and τ_{ii} are the shear and normal stress components of the stress tensor. Eq. (3.1) is equivalent to χ measured directly from birefringence under conditions where the stress-optic rule applies. The extinction angle gives us an idea of how closely the chain segments are aligned with the flow direction. Such an angle is important, among other reasons, because the force to stretch the chains is proportional to how closely the chains are aligned at 45°. As the chains align more strongly with the flow ($\chi \to 0$), they are stretched less strongly by the flow. However, for any given orientation they are pulled more strongly by increasing shear rate. Hence, a shear flow field causes competing effects: stretching by shear rate, and vorticity tending to align the chains in the flow direction.

We look further into the vorticity effect by keeping track of the *tumbling* of the chains. For this purpose, we define a tumble-rate, Ω_z, as *the average*

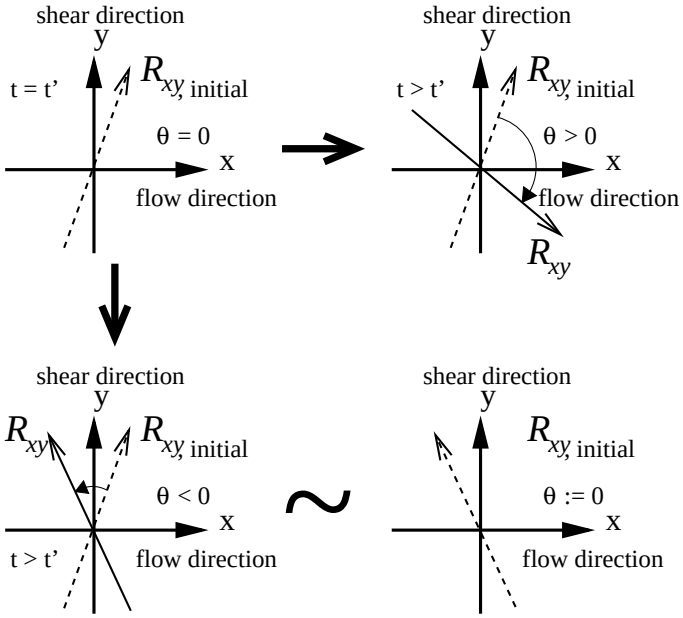

Figure 3.1. Sketch of chain tumble counting. Top: The origin of the count is the initial position of R_{xy}, the projection of the end-to-end vector on the xy-plane. A tumble is counted when the tumble angle, θ, reaches 360°. Bottom: If R_{xy} turns in the negative direction ($\theta < 0$), the new position of R_{xy} becomes the initial one, and the count starts over.

number of tumbles per chain per disengagement time, τ_{d}. Obviously, this requires a definition of a chain tumble which is illustrated in Figure 3.1. That is, we define a chain tumble as a full, positive revolution of R_{xy}, the projection of the chain end-to-end vector on the plane perpendicular to the neutral z-direction. Here, a shear flow with flow-direction x and shear-direction y is assumed. Hence, for each chain in the simulated ensemble we simply keep track of the initial orientation of R_{xy}, and count a tumble when R_{xy} has made a full revolution in the positive direction (the clockwise direction in the figure). However, if R_{xy} turns in the negative direction and passes the initial position for the tumble count, we reset the count and make this position the initial one for the tumble revolution. This situation is shown in the bottom part of Figure 3.1.

The above definition provides a good measure of our physical picture of chain tumbling in entangled polymer systems. Within this picture, tumbling is a "rope-over-a-pulley" kind of motion initiated by a chain end being grabbed by the flow after attaining an orientation in the shear direction. We expect Ω_z to be of order unity at equilibrium, since chain tumbling is governed by reptation in this case. This is confirmed by an equilibrium simulation.

The other main subject of this work, besides looking at chain orientation, is to study the amount of molecular stretching during and following a shear deformation. This is done by introducing an overall stretch ratio, λ,

which we define as the ratio of the present average chain contour length to the average contour length of a chain at equilibrium. In addition to the average overall chain stretching, we look into how the molecular stretch is distributed along the chain contour. We do this in terms of the *monomer density*, ρ_{mono}, rather than a local stretch ratio, λ_{local}, which is the inverse quantity. Thus, we define the local monomer density along the chain contour as

$$\rho_{\text{mono}} = \lambda_{\text{local}}^{-1} = \left(\frac{\langle Q_i \rangle}{\langle Q_i \rangle_{\text{eq}} \lambda} \right)^{-1}, \tag{3.2}$$

where $\langle Q_i \rangle$ is the average length of the chain segment between beads i and $i+1$, and $\langle Q_i \rangle_{\text{eq}}$ is the corresponding equilibrium length. The presence of λ in Eq. (3.2) serves to decouple the local stretching from the overall extension of the chain. Hence, $\rho_{\text{mono}} = 1$ results everywhere if the monomers are distributed uniformly along the contour length, whereas $\rho_{\text{mono}} > 1$ denotes a segment, which is less stretched relative to λ.

For both the monomer density and the chain contour length it should be kept in mind that these quantities can vary only on the level of description resolved by the model, whereas both the monomer density along the chain contour and the total contour length are always fixed on a sufficiently detailed level of description.

3.3 Results and discussion

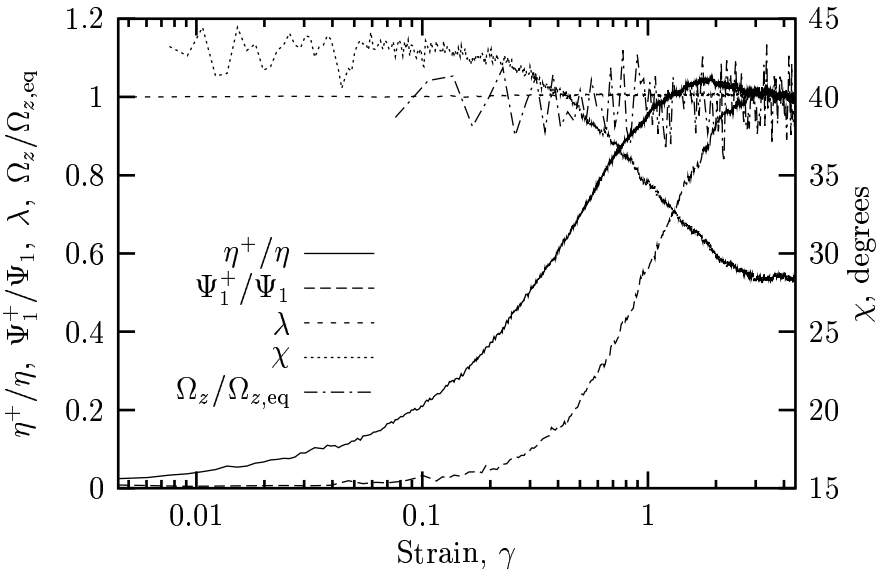

Figure 3.2. Start up of steady shear flow with $De = 1.5$. The transient shear viscosity, η^+, and first normal stress coefficient, Ψ_1^+, normalized by their steady state values are plotted against the shear strain, γ. Also shown are the extinction angle, χ, the overall chain stretching, λ, and the tumble-rate, Ω_z, normalized by its equilibrium value.

3.3.1 Inception of steady shear and steady shear

Figure 3.2 shows the transient shear viscosity, η^+, and first normal stress coefficient, Ψ_1^+, normalized by their steady state values, as functions of the shear strain, γ, following inception of steady shear for a slow deformation. The Deborah number for the flow, which is the shear-rate made dimensionless by the disengagement time, is $De = 1.5$. Similar curves for several shear rates are given in the previous work (Hua *et al.*, 1999, Figures 1–3 and 10), which also contain experimental data that validates the model predictions.

Also shown in Figure 3.2 is the extinction angle, χ, which confirms that the flow is indeed weak in this case. The steady state value of $\chi = 28.5°$ does not differ dramatically from 45°, the isotropic value, which shows that the chains are only weakly aligned with the flow. Furthermore, we show in Figure 3.2 the overall chain stretching, λ, and the tumble-rate, Ω_z, normalized by its equilibrium value. It is seen that there is no significant chain stretching, and that the tumble-rate stays at its equilibrium value, which is expected because of the slow deformation rate. The rather noisy tumble-rate signal is due to the fact that chain tumbling is a very infrequently occurring event.

Figure 3.3 shows the same plots as in Figure 3.2 but for an intermediate shear rate of $De = 30$. At the intermediate shear rate the chains align much more with the flow as is seen in the extinction angle, which decreases to a steady state value of 9.3°. A calculation of a Deborah number based

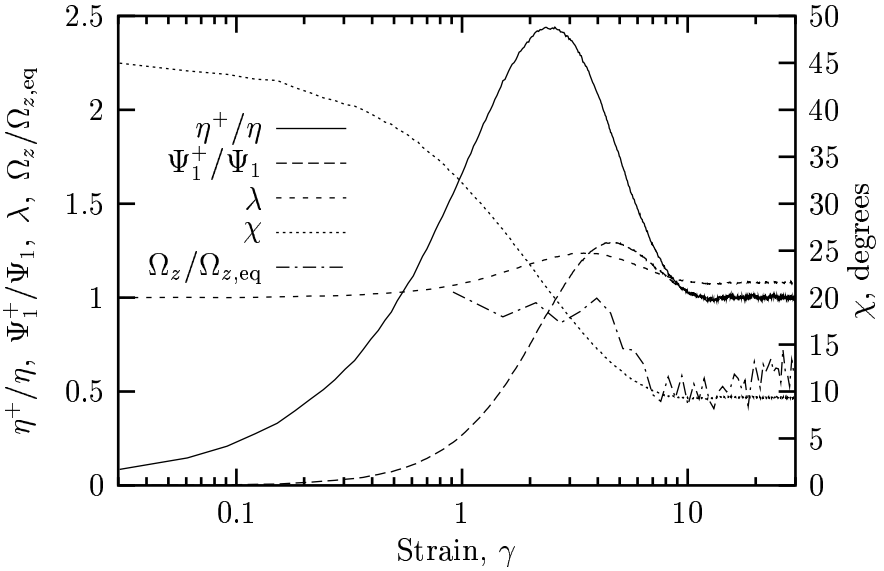

Figure 3.3. Start up of steady shear flow with $De = 30$. The transient shear viscosity, η^+, and first normal stress coefficient, Ψ_1^+, normalized by their steady state values are plotted against the shear strain, γ. Also shown are the extinction angle, χ, the overall chain stretching, λ, and the tumble-rate, Ω_z, normalized by its equilibrium value.

on the Rouse relaxation time, τ_{R}, rather than the disengagement time, τ_{d}, gives $De_{\mathrm{Rouse}} = De/3\langle Z\rangle_{\mathrm{eq}} = 30/21 \approx 1.43$ with $\langle Z\rangle_{\mathrm{eq}} = 7$. Hence, for $De = 30$ we expect the flow to be strong enough to induce molecular stretching, not only in the transient phase but also at steady state, and this is indeed seen from the λ-curve in Figure 3.3.

Following the initially induced stresses the competing effects of orientation and stretching also become evident in Figure 3.3. Chain stretching, λ, tends to enhance both the shear stress and the first normal stress difference whereas the increasing orientation, as seen by the decreasing χ-value, decreases η^+ but increases Ψ_1^+. In the strain interval $1 < \gamma < 2.5$ stretching dominates orientation causing both η^+ and Ψ_1^+ to grow. However, at a strain of about 2.5, where η^+ attains its maximum value, orientation takes over, and the shear viscosity begins to drop. Soon thereafter, at $\gamma \approx 3$, the stretching reaches its maximum and starts decreasing because of the growing inability of the flow to stretch the chains, which in turn is due to the increased chain alignment with the flow. The first normal stress coefficient continues to rise, though, despite the decreasing λ, since χ is still decreasing, but as the change in χ levels off, Ψ_1^+ also peaks and begins approaching its steady state value from above.

The above trends are consistent with the stress developments depicted in Figure 3.2, where the shear rate is low. In that case we observe no molecular stretching, and as a consequence there is no overshoot in the first normal stress coefficient, which attains its steady state as the steady state orientation is reached. The decreasing effect of orientation on the shear stress does not kick in, however, until χ differs sufficiently from the isotropic value of 45°, which explains the overshoot in η^+.

A somewhat surprising observation in Figure 3.3 is, that the tumble-rate, Ω_z, decreases significantly from a level around its equilibrium value before rising again to a steady state level also below the equilibrium value. The suppression of Ω_z by the flow may be attributed to an effect of chain retraction following molecular chain stretching. As a chain retracts to relax stretching, the chain ends are pulled into tube segments of greater orientation, which, as a first effect, enhances the overall orientation to further decrease the stretching ability of the flow.

Continuous chain stretching by the flow followed by chain retraction causes relatively more destruction than creation of tube segments, which decreases the ability of the chain ends to explore new configurations. The reduced ability of the ends to explore new orientations is what slows down the tumble-rate, since tumbles are initiated by chain ends being grabbed by the flow after attaining an orientation in the shear-direction. This explanation of the suppression of Ω_z also accounts for the increasing tumble-rate later on when the stretching and retraction processes slow down to their steady state values, and it is consistent with the fact that no change in Ω_z is observed at low shear rates, where chain stretching does not occur (see Figure 3.2).

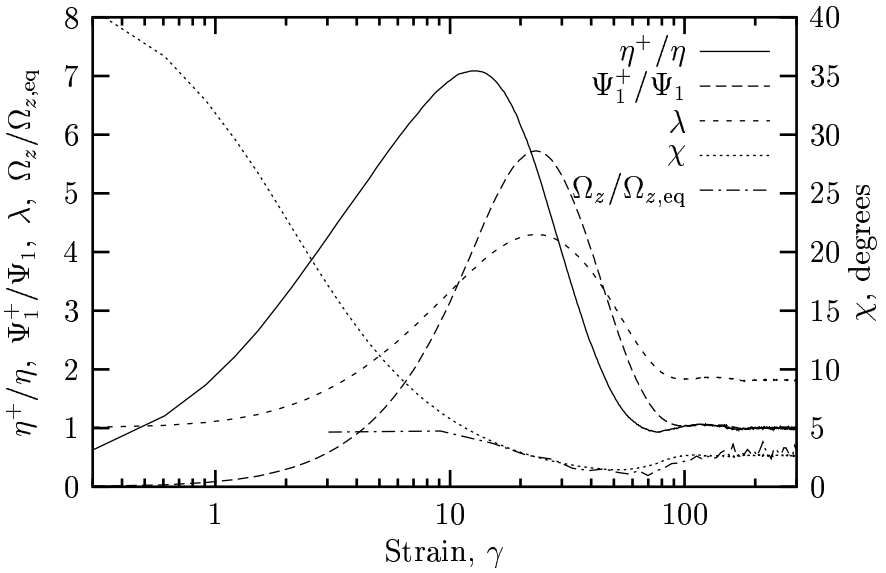

Figure 3.4. Start up of steady shear flow with $De = 300$. The transient shear viscosity, η^+, and first normal stress coefficient, Ψ_1^+, normalized by their steady state values are plotted against the shear strain, γ. Also shown are the extinction angle, χ, the overall chain stretching, λ, and the tumble-rate, Ω_z, normalized by its equilibrium value.

In Figure 3.4, we repeat the plots from the two previous figures, but for a high shear rate of $De = 300$. It is immediately evident that the effect of molecular stretching is much more pronounced at the high shear rate, which makes all the trends observed in Figure 3.3 appear more clearly. The effects of orientation and stretching are competing as previously described, but in Figure 3.4, where the maxima of Ψ_1^+ and λ occur at the same strain, it becomes evident, that the first normal stress difference is largely governed by chain stretching as recognized by Pearson *et al.* (1991). For the shear viscosity we observe an undershoot at the end of the transient that may be attributed to the extinction angle, which also undershoots and approaches its steady state value from below. A similar undershoot in χ, although of substantially smaller magnitude, is observed for the intermediate shear rate in Figure 3.3.

The simultaneous occurrences of the minima in χ and Ω_z revealed in Figure 3.4 strongly suggest that the undershoot in the extinction angle is caused by the undershoot in tumble-rate. As Ω_z decreases due to the suppression mechanism described above, relaxation of orientation also slows down which causes greater orientation of the average chain and is manifested in a smaller extinction angle. Conversely, χ grows with the increasing orientational relaxation as suppression of the tumble-rate ceases, and consequently, the extinction angle follows the trend of the tumble-rate until steady state is reached.

The extinction angle undershoot, which is observed experimentally only

at shear rates where chain stretching occurs (Oberhauser *et al.*, 1997; Hua *et al.*, 1999), is not captured by other advanced reptation theories of the single-segment type, presumably because of an insufficient level of description. One such theory (Mead *et al.*, 1998) does not get the effect at all, while another (Fang *et al.*, 2000) shows some undershoot in χ, although it is too small and too abrupt.

In the latter theory, considered by Fang *et al.* (2000), the effect of constraint release is mimicked by a noise term added to the governing equation for the tube dynamics, and undershoot in the extinction angle is observed only if the CR mechanism is switched on. This is because the noise added to the tube motion enables the chain segment to attain orientations in the shear direction, which in turn allows the chain to be grabbed by the flow and initiates tumbling in the same fashion the chain ends trigger tumbling for the full-chain model. However, since the model is a single-segment theory, the induced tumbling occurs on a too fast time scale because it involves revolution of one tube segment only as opposed to the full-chain model, where tumbling is a coordinated motion of the entire chain. This fundamental difference explains why the undershoot in extinction angle observed by Fang *et al.* is too small and too abrupt. Thus, it appears that a full-chain description, in which segment connectivity is taken into account, and which therefore allows for chain tumbling on the correct time scale, may be necessary in order to capture the subtle effect of undershoot in χ quantitatively.

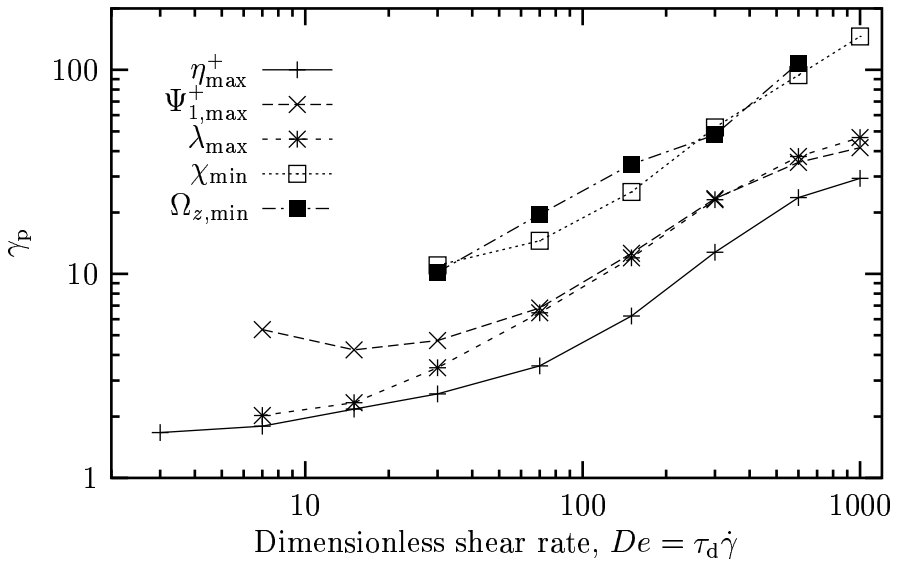

Figure 3.5. Start up of steady shear flow. Strain magnitude, γ_p, as a function of shear rate for the occurrences of extrema in the transient shear viscosity, η^+, the transient first normal stress coefficient, Ψ_1^+, the overall chain stretching, λ, the extinction angle, χ, and the tumble-rate, Ω_z.

In order to further support the proposed relationship between the undershoots in extinction angle and tumble-rate, we show in Figure 3.5 the strain, γ_p, at which these minima occur for several shear rates. The agreement between the resulting curves for χ_{min} and $\Omega_{z,min}$ is remarkable considering the generally rather noisy tumble-rate signal in the simulations. The occurrences of the maxima in the shear viscosity, the first normal stress coefficient and the overall chain stretching are also shown in Figure 3.5. It is seen that the curves for $\Psi^+_{1,max}$ and λ_{max} coincide for $De \geq 70$ which verifies the recognition by Pearson *et al.* (1991), that for sufficiently high shear rates, the first normal stress difference is governed by and is a good measure of the overall chain stretching.

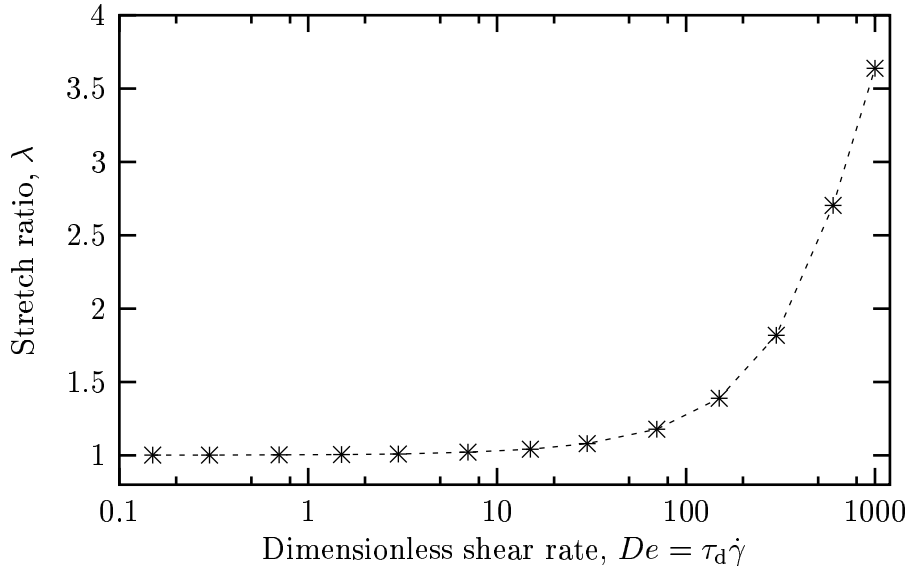

Figure 3.6. Steady state shear. Overall chain stretching as a function of shear rate.

The onset of chain stretching at steady state is expected to occur at a shear rate equal to the inverse Rouse relaxation time, τ_R. Hence, keeping in mind that for the model $\tau_d/\tau_R = 3\langle Z\rangle_{eq}$, we expect to observe chain stretching when $De \geq 21$ (for $\langle Z\rangle_{eq} = 7$). This is confirmed by Figure 3.6, in which we have plotted the steady state stretch ratio, λ, against the shear rate.

We obtain a more detailed view of the chain stretching at steady state in Figure 3.7, which depicts the steady state distribution of monomers, ρ_{mono}, along the chain contour, s, for several shear rates. The figure shows that for low shear rates ($De \leq 15$) the monomer density is uniform along the contour. However, as the shear rate is increased and chain stretching becomes increasingly important, the monomers become more and more non-uniformly distributed along the chain contour with the lowest monomer density at the middle of the chain and the highest density at the ends.

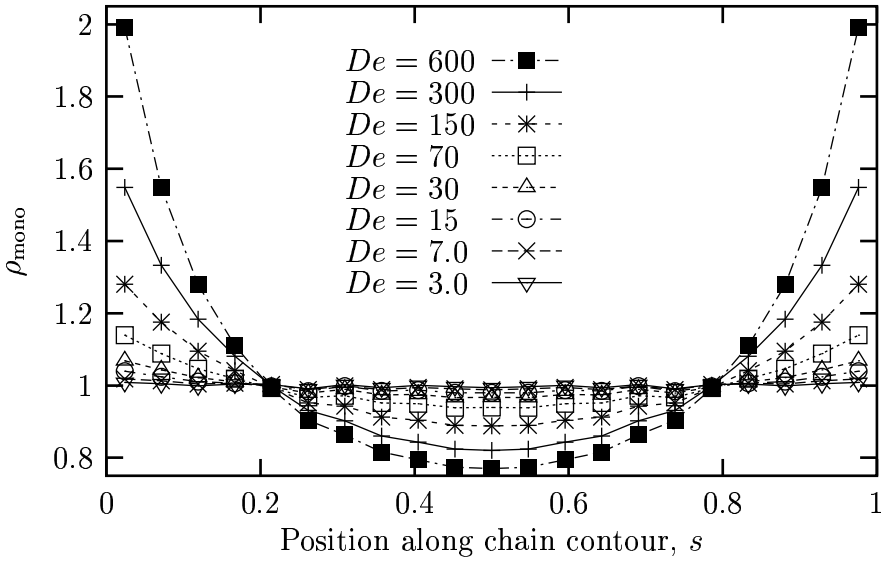

Figure 3.7. Steady state shear. Monomer density plotted against the position along the chain contour, s, for several shear rates. Location of the chain ends: $s = 0, 1$. Location of the middle of the chain: $s = 0.5$.

The resulting non-uniform distribution of monomers may be attributed to relaxation of the segmental orientation rather than the competing processes of molecular stretching and chain retraction. We will later show that retraction occurs simultaneously for all chain segments (see Figure 3.11), and since the source of stretching is affine deformation of the confining tube, inhomogeneous stretching on the molecular level is possible only if the segmental orientation is non-uniform along the chain contour. Brownian forces may also contribute to molecular stretching, but this effect is zero on average. Hence, the non-uniform monomer density seen in Figure 3.7 not only expresses non-uniform stretching but also reveals a non-uniform orientational distribution of segments along the chain contour which in turn is explicable in terms of relaxation of segmental orientation.

The relative high monomer density at the ends confirms the common reptation picture, that orientation relaxes from the ends towards the middle of the chain. The chain ends are readily relaxed due to reptation, retraction and chain-length fluctuations and are thus never far removed from the equilibrium configuration. This is in contrast to the chain middle, which exhibits the largest molecular stretch (the lowest monomer density) that can be relaxed only by the propagating relaxation from the ends or by rarely occurring constraint releases.

The non-uniform distribution of monomers along the chain contour is even more pronounced during the transient prior to reaching steady state flow, which could be expected because of the large overall chain stretching in that phase of the flow. This is seen in Figure 3.8, which shows the de-

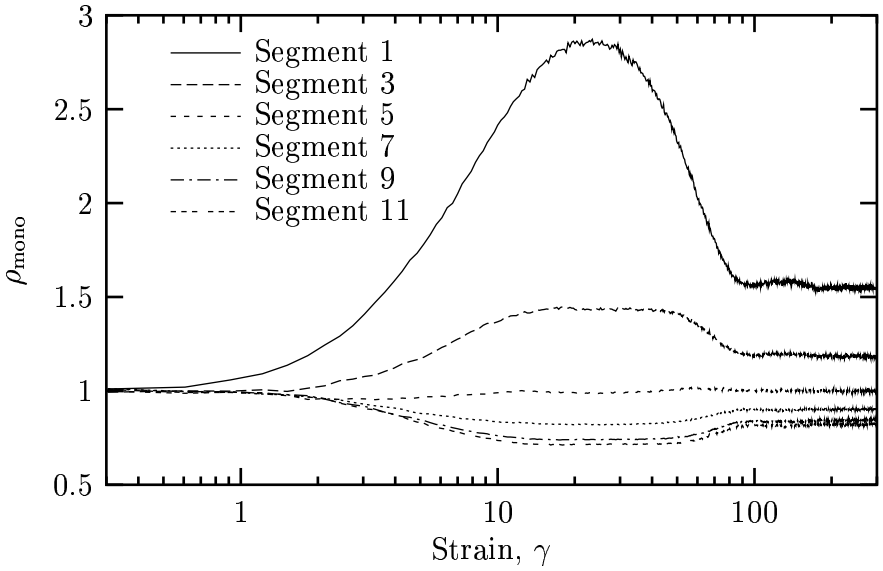

Figure 3.8. Start up of steady shear flow with $De = 300$. Monomer density as a function of shear strain for different chain segments. "Segment 1" is the end segment. "Segment 11" is located at the middle of the chain.

velopment of the monomer density in different chain segments for start up of steady shear with a shear rate of $De = 300$. For $\langle Z \rangle_{\text{eq}} = 7$ discretization of the chain implies $N = 21$ chain segments. Hence, the evolution of ρ_{mono} at the chain end is denoted by "segment 1" in the figure, whereas "segment 11" shows the transient monomer density at the middle of the chain. It is noted that ρ_{mono} for segment number 5 is close to unity at all times during the flow.

The figure provides a detailed view of how the non-uniform distribution of monomers along the contour is developed. Upon start up, all chain segments are uniformly deformed, but soon thereafter the outermost segment begins to exhibit relaxation competing with the flow, and ρ_{mono} increases indicating relative less stretching at the ends, whereas the other segments continue to be deformed in a uniform manner. As the flow proceeds, the relaxation processes competing with deformation reach more segments from the chain end causing these to be stretched less relative to the mid segments where ρ_{mono} continues to decrease, and the non-uniform monomer density is established.

Switching off the constraint release mechanism alters the simulation results quantitatively but *not* qualitatively. That is, the magnitude of overall chain stretching and stresses is affected by enabling or disabling CR, whereas the strain magnitude, at which the extrema for these quantities occur, is not significantly influenced. Contrary to the model considered by Fang *et al.* (2000) and discussed above, we still observe tumbling and undershoot in the extinction angle when CR is switched off, since the

ability of the chain ends to attain orientations in the shear direction is not governed by the CR mechanism. However, as will be shown later (see Figure 3.12) CR not only provides relaxation of orientation, but also aids the process of chain retraction and consequently influences suppression of the tumble-rate too. When CR is absent, tumble-rate suppression is limited until the overall chain stretching peaks, and the undershoot in Ω_z therefore occurs at a higher strain magnitude than in the presence of CR. The shifted occurrence of the tumble-rate minimum in absence of CR causes the minimum in extinction angle to shift accordingly in agreement with the above discussions on the relationship between χ and Ω_z. Hence, all conclusions made to this point concerning the relationships between microscopic dynamics and macroscopic properties are valid regardless of the presence of CR.

At low to moderate shear rates switching off CR results in larger stresses and increases the overall chain stretching both during the initial transient and at steady state. This is expected, since constraint release offers an extra relaxation mechanism in addition to reptation, chain retraction and chain-length fluctuations. The trend is the same during the transient following inception of flow at high shear rates. At steady state and sufficiently high shear rates, however, we observe *more* chain stretching and *higher* stresses when CR is *enabled* (also see Figure 8 of Hua *et al.* (1999)).

That may seem contradictory, since CR provides additional relaxation, but here it must be kept in mind that the orientational relaxation due to

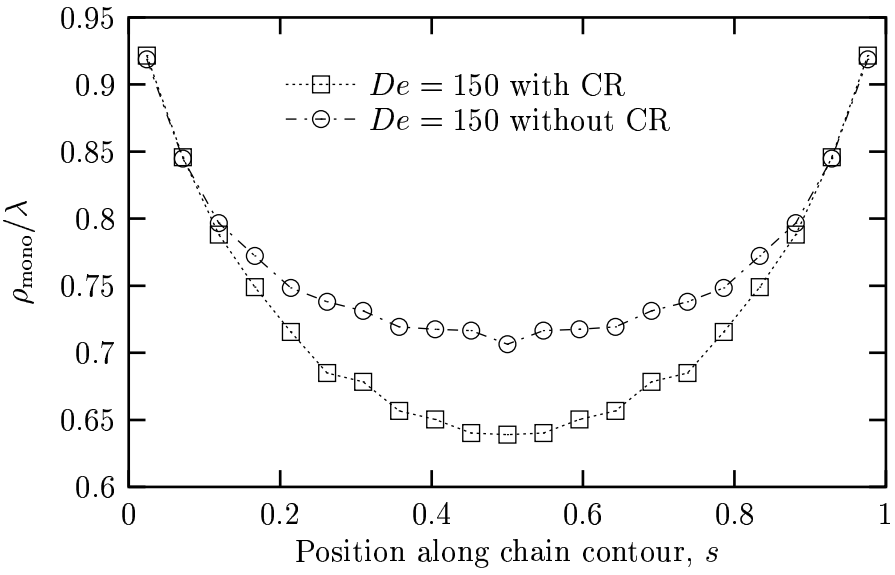

Figure 3.9. Steady state shear flow with $De = 150$. Monomer density divided by overall chain stretching for simulations with and without CR plotted against the position along the chain contour, s. Location of the chain ends: $s = 0, 1$. Location of the middle of the chain: $s = 0.5$.

constraint release, which may occur all along the chain contour, affects the chain in more ways. When taking place at the chain ends, CR simply adds to the rate at which the ends explore new configurations, just like the other relaxation mechanisms. However, a constraint release on an interior tube segment not only partially relaxes the orientation and stretching of the chain fraction in this tube segment, it also enhances the ability of the flow to subsequently stretch the chain even more. Furthermore, the rate, at which CR occurs, grows with increasing shear rate because of the CCR effect (for details of the CR mechanism see Hua and Schieber (1998); Hua *et al.* (1999)). Thus, at high shear rates and steady state, readily occurring constraint releases prevent the chains from aligning too much with the flow, which sustains its ability to stretch the chains. The CR effect therefore leads to an altered distribution of stretching and orientation along the chain contour, which can be seen in Figure 3.9. Here we plot the steady state monomer distribution against the position along the chain contour for simulations with and without CR and a shear rate of $De = 150$. The results are divided by the overall chain stretching for easier comparison.

3.3.2 Cessation of steady shear

In Figure 3.10 we show the transient shear viscosity, η^-, and first normal stress coefficient, Ψ_1^-, normalized by their steady state values, as functions

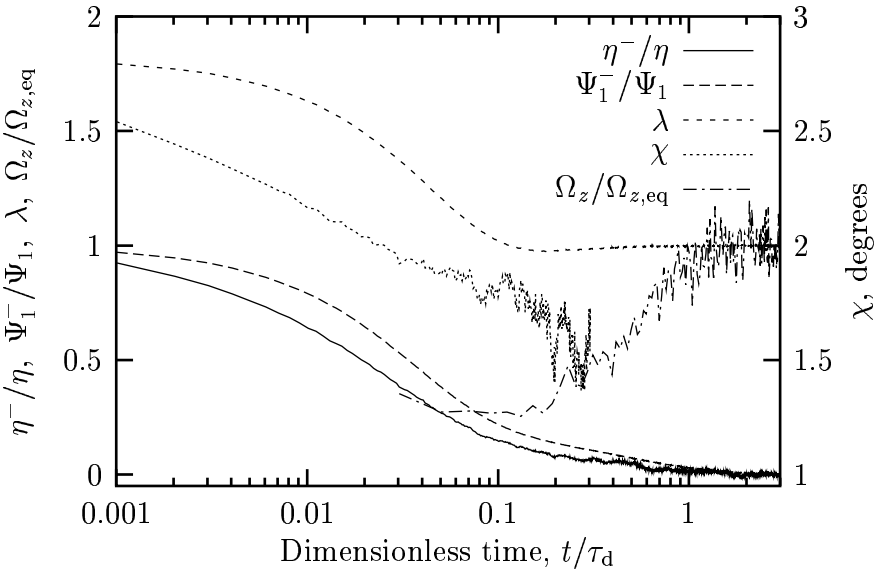

Figure 3.10. Cessation of steady shear flow with $De = 300$. The transient shear viscosity, η^-, and first normal stress coefficient, Ψ_1^-, normalized by their steady state values, are plotted as functions of the time following cessation of flow. Also shown are the extinction angle, χ, the overall chain stretching, λ, and the tumble-rate, Ω_z, normalized by its equilibrium value.

of the time, t, following cessation of steady shear flow with $De = 300$. Furthermore, we plot the extinction angle, χ, the overall chain stretching, λ, and the tumble-rate, Ω_z, normalized by its equilibrium value, to make the analogy with Figure 3.4 complete. The shear rate of the flow preceding the depicted stress relaxation is of less importance though, as analogous plots for other shear rates show exactly the same trends and differ only quantitatively.

In the figure, we first note that while chain retraction occurs (while λ decreases), the stresses relax in a manner such that the extinction angle decreases. This behavior of χ was already observed in the previous paper and is consistent with experimental data (Hua *et al.*, 1999, Figure 16). The decreasing extinction angle upon cessation of steady shear flow can be explained by means of the non-uniform distribution of stretching and orientation along the chain contour at steady state discussed in Figure 3.7 in terms of the non-uniform monomer density. As chain retraction takes place, the outermost, least oriented tube segments are destroyed first, while the chain retracts into tube segments of greater orientation causing χ to drop.

Following completion of chain retraction, suppression of tumbling ceases, and the tumble-rate slowly approaches its equilibrium value. Meanwhile, the extinction angle first levels off before the signal becomes noisy and finally undefined due to the stresses approaching zero (also see Eq. (3.1)).

We proceed to look at the chain retraction process itself in more detail.

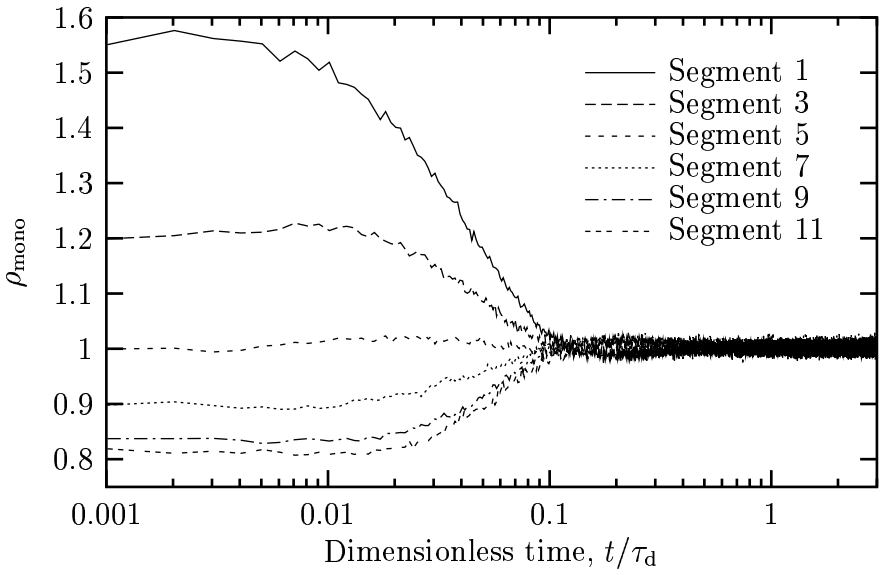

Figure 3.11. Cessation of steady shear flow with $De = 300$. Monomer density for different chain segments as a function of time following cessation of flow. "Segment 1" is the end segment. "Segment 11" is located at the middle of the chain.

Figure 3.11 shows the development of the monomer density in different chain segments following cessation of steady shear with a shear rate of $De = 300$. Like in Figure 3.8, ρ_{mono} at the chain end is denoted by "segment 1", and "segment 11" denotes the transient monomer density at the middle of the chain. Figure 3.11 provides evidence that chain retraction occurs simultaneously for all chain segments despite the non-uniform distribution of stretching along the chain contour prior to the relaxation.

A closer look at the λ-curve in Figure 3.10 reveals an *undershoot* in the overall chain stretching before the equilibrium value, $\lambda = 1$, is reached. The undershoot is seen in Figure 3.12, where we plot the overall chain stretching from Figure 3.10 again, but for simulations both with and without CR. Since no undershoot is observed when constraint release is disabled, the undershoot may be attributed to CR and can be explained as follows. Upon termination of flow there are no processes left to keep the chains stretched. Thus, the chains retract rapidly causing lots of destruction of tube segments by abandonment, which in turn triggers a lot of constraint release. It is this combination of the fast retraction process and additional relaxation provided by CR, which makes the chains shrink excessively and produces the undershoot in λ. The effect, although less pronounced, is also observed for moderate shear rates, where chain stretching is still important.

Presumably, the observed undershoot in chain stretching following cessation of steady shear and the explanation thereof will be encountered

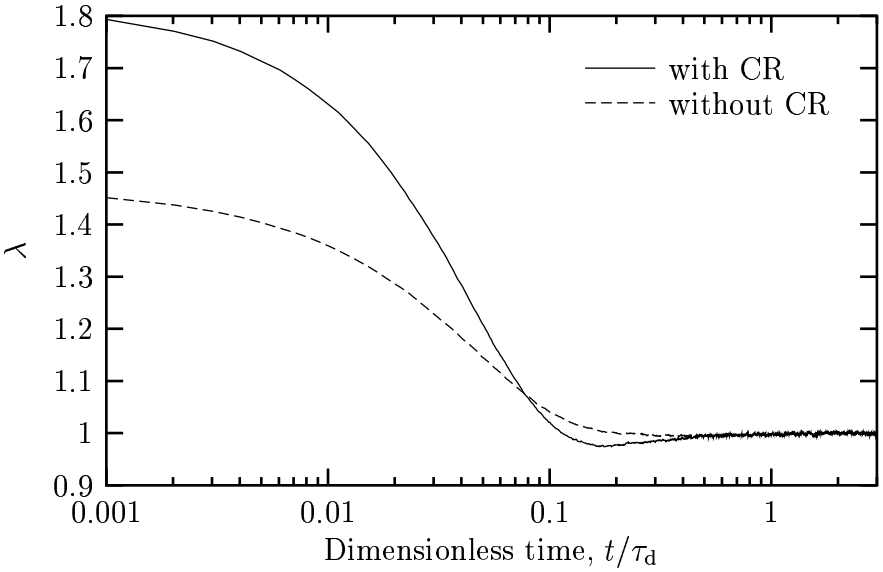

Figure 3.12. Cessation of steady shear flow with $De = 300$. Overall chain stretching, for simulations with and without constraint release (CR), plotted against the time following cessation of flow.

for any implementation of constraint release involving binary chain-chain interactions. It remains an open question, however, whether a different implementation of CR, such as the one utilized by Fang *et al.* (2000), will yield an undershoot in λ as observed here.

In the previous paper it was pointed out that stress relaxation following cessation of steady shear flow exhibits "time-strain-rate" separability, after chain retraction has ceased, by means of a generalized damping function, $h_c(\dot{\gamma})$. The separability resembles the time-strain separability for stress relaxation following a nonlinear step strain, which utilizes the traditional damping function $h(\gamma)$. Furthermore, it was suggested that an estimate of the amount of chain stretching in steady shear could be obtained by comparing $h_c(\dot{\gamma})$ and $h(\gamma)$, since for the latter, λ can be calculated analytically. We make such a comparison in Figure 3.13, which depicts the overall chain stretching at steady shear or immediately after imposing a step shear strain as functions of the generalized and traditional damping functions respectively. In the figure we have used two versions of $h_c(\dot{\gamma})$: one based on relaxation of shear stress, τ_{yx}, and another based on the principal stress, $\tau_p = (4\tau_{yx}^2 + (\tau_{xx} - \tau_{yy})^2)^{1/2}$. Unfortunately, neither of the generalized damping functions exhibit the same functionality of λ as the analytic one for $h(\gamma)$, which renders the proposed method of estimating the amount of chain stretching in steady shear impossible.

The reason why the proposed method fails, despite analogies between

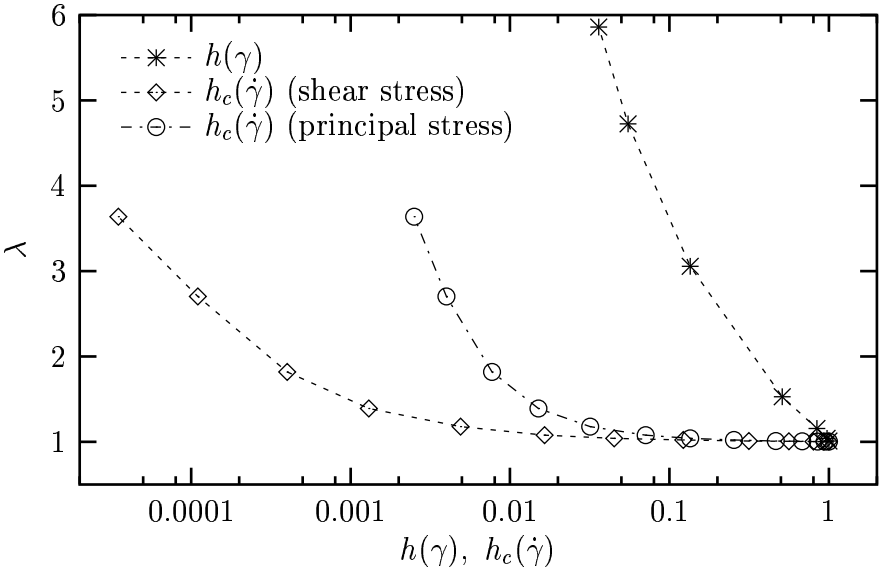

Figure 3.13. Relaxation of stress. Overall chain stretching as a function of various damping functions. $h(\gamma)$ is the damping function obtained from step strain simulations. $h_c(\dot{\gamma})$ is the generalized damping function obtained from cessation of steady shear simulations and based on either τ_{yx}, the shear stress ($\diamond$), or $\tau_p = [4\tau_{yx}^2 + (\tau_{xx} - \tau_{yy})^2]^{1/2}$, the principal stress ($\circ$).

the two cases of relaxation, is the difference in chain configurations immediately after the two types of deformation are terminated. In case of steady shear, we have already shown that the distribution of stretching and orientation is non-uniform along the chain contour (see Figure 3.7). The physical picture is quite different for the case of step strain, however, since the configuration distribution prior to the step is isotropic. Consequently, after applying the step strain, all segments have the same distribution regardless of their position along the chain, and the distribution of stretching and orientation is therefore uniform along the contour. The development of the extinction angle during relaxation reveals the difference between the two cases. Following cessation of steady shear, χ decreases as shown in Figure 3.10, whereas the Lodge-Meissner consistency relation (Lodge and Meissner, 1972), which is satisfied by the model (Hua and Schieber, 1998), implies a constant χ value during relaxation after a step strain.

3.3.3 The stress-optic rule

The empirical stress-optic rule, which constitutes a linear relationship between the stress and refractive index tensors, is generally assumed to be obeyed by entangled systems of linear polymers in shear deformations (Janeschitz-Kriegl, 1983). Violation of the rule may be expected only under conditions involving excessive molecular chain stretching, where finite extensibility becomes important. The model considered here seems suitable for providing an independent check of the validity of the stress-optic rule in shearing flows, because of its ability to predict quantitatively stresses and to capture nearly all viscometric flows while avoiding assumptions such as independent alignment or consistent averaging.

Hence, we perform a check to see whether the model predicts the stress-optic rule during inception of steady shear flow with a high shear rate, which is the case where we have observed the largest amount of chain stretching in this study (see Figure 3.4), and thus the situation where a deviation from the stress-optic rule is most likely to occur. The Kramers type stress tensor for the model reads

$$\underline{\underline{\tau}} \propto -n \left\langle \int_0^1 \frac{HQ(s)}{1-(H/k_{\mathrm{B}}T)Q(s)^2/b} \frac{\underline{u}(s)\underline{u}(s)}{|\underline{u}(s)|^2} ds \right\rangle, \tag{3.3}$$

which is to be compared with the refractive index tensor

$$\underline{\underline{n}} \propto -n \left\langle \int_0^1 HQ(s) \frac{\underline{u}(s)\underline{u}(s)}{|\underline{u}(s)|^2} ds \right\rangle. \tag{3.4}$$

Here, $\underline{u}(s)$ is the orientation vector of a tube segment, n is the number density of polymer, H is the Hookean spring constant, k_{B} is Boltzmann's constant and T is temperature.

The model does indeed predict a violation of the stress-optic rule in the transient start up phase of the flow as seen in Figure 3.14. Here, we plot

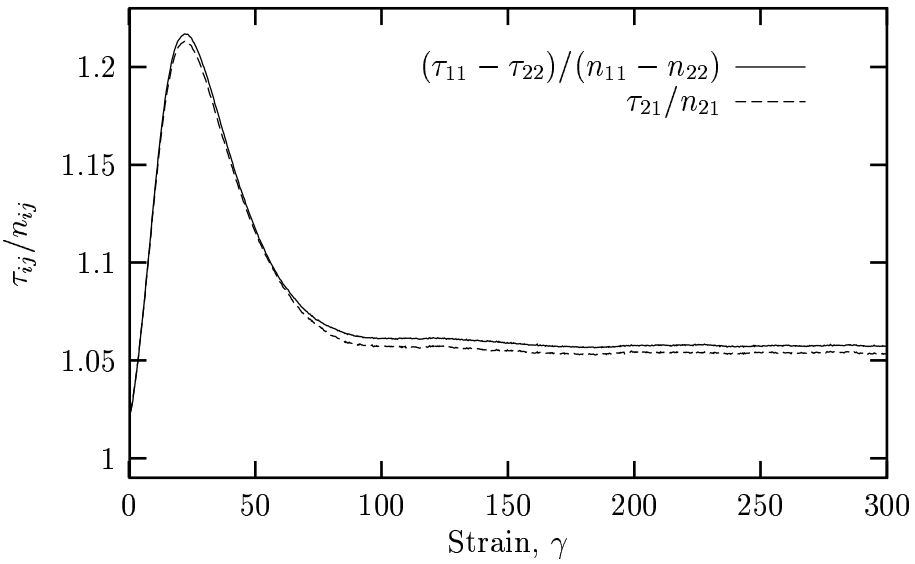

Figure 3.14. Start up of steady shear flow with $De = 300$. Ratios of corresponding components of the stress tensor, $\underline{\underline{\tau}}$, and refractive index tensor, $\underline{\underline{n}}$, are plotted against the shear strain as a check of the stress-optic rule.

the ratio of corresponding components of the stress and refractive index tensors during start up of steady shear with a shear rate of $De = 300$, which reveals a deviation of about 22% for both the shear and first normal difference components during the transient. In the figure we also note that a deviation from the stress-optic rule of 5.5% is predicted even at steady state, where violations of the stress-optic rule are not reported experimentally. However, for all shear rates the predicted deviation at steady state is less than the experimentally achievable standard error, and a violation of the stress-optic rule may therefore not be observed in this case. The predicted deviation during inception of steady shear is strongly dependent on shear rate ranging from only 8.5% for $De = 150$ to as much as 60% for $De = 600$.

The observed error could be explained, at least partially, in terms of one of the few quantitative limitations of the model, which is evident in Figures 1 and 3 of Hua *et al.* (1999). Here, it is seen that while the model captures perfectly the occurrences of transients following inception of flow, the magnitude of the stress transients is somewhat overpredicted. The too large stresses may be attributed to the fact that the chain is modeled as a constant number of beads and springs implying a constant number of friction points between the test chain and the confining tube under all circumstances. Conversely, the physical picture of convective constraint release suggests that the number of contact points between the test chain and its tube decreases with increasing shear rate.

On the other hand, to the best of our knowledge experimental data

has yet to be reported in literature that confirms either the validity or a violation of the stress-optic rule during inception of steady shear flow at high shear rates. Despite the stress overprediction by the model, the predicted deviation from the stress-optic rule seems severe enough that it should be detectable at experimentally accessible shear rates and we encourage such experiments to be made.

3.4 Conclusions

We have studied a previously proposed self-consistent reptation model that includes chain stretching, chain-length fluctuations, segment connectivity and constraint release, and which requires no further assumptions or approximations in order to obtain results. While it was made clear in an earlier paper (Hua *et al.*, 1999) that the model is able to capture nearly all trends observed experimentally in transient and steady shearing flows, the focus of the present work has been entirely on the model. That is, we have studied in detail the physics and underlying dynamics of the model to explain the macroscopically observed rheological properties in terms of chain behavior and dynamics on the molecular level. The main conclusions made during this study can be summarized as follows:

1. The model confirms the idea (Pearson *et al.*, 1991), that the first normal stress difference overshoot following inception of steady shear at moderate and high shear rates is caused by molecular chain stretching (Figures 3.3 – 3.5). No overshoot is observed at low shear rates where chain stretching is unimportant (Figure 3.2).

2. Chain retraction induced by molecular stretching reduces the ability of the chain ends to explore new configurations. Therefore, the presence of chain stretching suppresses the rate at which chains tumble during flow (Figures 3.3, 3.4 and 3.10).

3. The transient undershoot in the extinction angle during start up of steady shear flow at high shear rates may be attributed to chain tumbling (Figures 3.4 and 3.5). The success of the considered model in predicting this undershoot suggests that a full-chain description may be necessary in order to capture this subtle feature quantitatively.

4. Except for low shear rates at steady state, we observe a non-uniform distribution of monomers along the chain contour in steady shear as well as during start up of and following cessation of steady shear (Figures 3.7, 3.8 and 3.11).

   The non-uniform monomer distribution along the chain contour makes stress relaxation following cessation of steady shear fundamentally

different from stress relaxation following a step shear strain (Figure 3.13).

5. During relaxation following cessation of steady shear the overall chain stretching exhibits an undershoot when approaching the equilibrium value (Figure 3.12). The effect is caused by the constraint release mechanism (CR) which does otherwise not influence any of the trends discussed in this work.

Finally, we notice that the model predicts a violation of the stress-optic rule during start up of steady shear with high shear rates. Since we have been unable to find experimental data to either verify or reject this prediction, it remains unclear though, if this violation of the stress-optic rule is real or merely an artifact of the model which overpredicts stresses somewhat under these conditions.

All of the above observations and discussions of microscopic dynamics and their influence on the macroscopic rheological properties are thought of as inspirational guidelines for future modeling based on dynamics on the molecular level.

Acknowledgments

The authors would like to thank Professor David C. Venerus for valuable discussions during the analysis of the results presented in this manuscript. One of the authors (J.N.) would like to thank the Danish government for financial support through the Department of Chemical Engineering at the Technical University of Denmark (DTU).

References

Bird, R. B.; Curtiss, C. F.; Armstrong, R. C. and Hassager, O. (1987). *Dynamics of Polymeric Liquids Vol. II: Kinetic Theory*. Wiley-Interscience, New York, second edition.

des Cloizeaux, J. (1988). Double reptation vs. simple reptation in polymer melts. *Europhys. Lett.*, **5**, 437–442.

Doi, M. (1983). Explanation for the 3.4-power law for viscosity of polymeric liquids on the basis of the tube model. *J. Polym. Sci., Polym. Phys. Ed.*, **21**, 667–684.

Doi, M. and Edwards, S. F. (1978a). Dynamics of concentrated polymer systems part 1. Brownian motions in the equilibrium state. *J. Chem. Soc. Faraday Trans. II*, **74**, 1789–1800.

Doi, M. and Edwards, S. F. (1978b). Dynamics of concentrated polymer systems part 2. Molecular motion under flow. *J. Chem. Soc. Faraday Trans. II*, **74**, 1802–1817.

Doi, M. and Edwards, S. F. (1978c). Dynamics of concentrated polymer systems part 3. The constitutive equation. *J. Chem. Soc. Faraday Trans. II*, **74**, 1818–1832.

Doi, M. and Edwards, S. F. (1979). Dynamics of concentrated polymer systems part 4. Rheological properties. *J. Chem. Soc. Faraday Trans. II*, **75**, 38–54.

Doi, M. and Edwards, S. F. (1986). *The Theory of Polymer Dynamics*. Clarendon Press, Oxford.

Fang, J.; Kröger, M. and Öttinger, H. C. (2000). A thermodynamically admissible reptation model for fast flows of entangled polymers. II. Model predictions for shear and extensional flows. *J. Rheol.*, **44**, 1293–1317.

Ferry, J. L. (1980). *Viscoelastic Properties of Polymers*. John Wiley & Sons, New York, third edition.

Fetters, L. J.; Lohse, D. J. and Colby, R. H. (1996). Chain dimensions and entanglement spacings. In *Physical Properties of Polymers Handbook*. AIP, New York.

Flory, P. J. (1988). *Statistical Mechanics of Chain Molecules*. Hanser, Munich.

Hua, C. C. and Schieber, J. D. (1998). Segment connectivity, chain-length breathing, segmental stretch, and constraint release in reptation models. I. Theory and single-step strain predictions. *J. Chem. Phys.*, **109**(22), 10018–10027.

Hua, C. C.; Schieber, J. D. and Venerus, D. C. (1998). Segment connectivity, chain-length breathing, segmental stretch, and constraint release in reptation models. II. Double-step strain predictions. *J. Chem. Phys.*, **109**(22), 10028–10032.

Hua, C. C.; Schieber, J. D. and Venerus, D. C. (1999). Segment connectivity, chain-length breathing, segmental stretch, and constraint release in reptation models. III. Shear Flows. *J. Rheol.*, **43**(3), 701–717.

Ianniruberto, G. and Marrucci, G. (1996). On compatibility of the Cox-Merz rule with the model of Doi and Edwards. *J. Non-Newtonian Fluid Mech.*, **65**, 241–246.

Janeschitz-Kriegl, H. (1983). *Polymer Melt Rheology and Flow Birefringence*. Springer-Verlag, Berlin.

Ketzmerick, R. and Öttinger, H. C. (1989). Simulation of a non-Markovian process modeling contour length fluctuation in the Doi-Edwards model. *Continuum Mech. Thermodyn.*, **1**, 113.

Lodge, A. S. and Meissner, J. (1972). On the use of instantaneous strains, superposed on shear and elongational flows of polymeric liquids, to test the Gaussian network hypothesis and to estimate segment concentration and variation during flow. *Rheol. Acta*, **11**, 351–352.

Marrucci, G. (1996). Dynamics of entanglements: A nonlinear model consistent with the Cox-Merz rule. *J. Non-Newtonian Fluid Mech.*, **62**, 279–289.

Marrucci, G. and Grizzuti, N. (1988). Fast flows of concentrated polymers: Predictions of the tube model on chain stretching. *Gazzetta Chimica Italiana*, **118**, 179–185.

Mead, D. W. and Leal, L. G. (1995). The reptation model with segmental stretch I. Basic equations and general properties. *Rheol. Acta*, **34**, 339–359.

Mead, D. W.; Yavich, D. and Leal, L. G. (1995). The reptation model with segmental stretch II. Steady flow properties. *Rheol. Acta*, **34**, 360–383.

Mead, D. W.; Larson, R. G. and Doi, M. (1998). A molecular theory for fast flows of entangled polymers. *Macromolecules*, **31**, 7895–7914.

Milner, S. T. and McLeish, T. C. B. (1997). Parameter-Free Theory for Stress Relaxation in Star Polymer Melts. *Macromolecules*, **30**, 2159–2166.

Milner, S. T. and McLeish, T. C. B. (1998). Reptation and Contour-Length Fluctuations in Melts of Linear Polymers. *Phys. Rev. Letters*, **81**(3), 725–728.

Neergaard, J.; Park, K.; Venerus, D. C. and Schieber, J. D. (2000). Exponential Shear Flow of Linear, Entangled Polymeric Liquids. *J. Rheol.*, **44**(5), 1043–1054.

Oberhauser, J. P.; Leal, L. G. and Mead, D. W. (1997). A note on the response of entangled polymer solutions to step changes of shear rate. *J. Polym. Sci., Polym. Phys. Ed.*, **36**(2), 265–280.

Öttinger, H. C. (1994). Modified reptation model. *Phys. Rev. E*, **50**, 4891–4895.

Öttinger, H. C. (1999). A thermodynamically admissible reptation model for fast flows of entangled polymers. *J. Rheol.*, **43**, 1461–1493.

Öttinger, H. C. and Beris, A. N. (1999). Thermodynamically consistent reptation model without independent alignment. *J. Chem. Phys.*, **110**, 6593–6596.

Pearson, D. S.; Herbolzheimer, E. A.; Marrucci, G. and Grizzuti, N. (1991). Transient behavior of entangled polymers at high shear rates. *J. Polym. Sci., Polym. Phys. Ed.*, **29**, 1589–1597.

Tsenoglou, C. (1987). Viscoelasticity of binary homopolymer blends. *Am. Chem. Soc. Polym. Preprints*, **28**, 185.

Venerus, D. C. and Kahvand, H. (1994). Doi-Edwards theory evaluation in double-step strain flows. *J. Polym. Sci., Polym. Phys. Ed.*, **32**, 1531–1542.

4

Exponential Shear Flow of Linear, Entangled Polymeric Liquids

A previously proposed reptation model is used to interpret exponential shear flow data taken on an entangled polystyrene solution. Both shear and normal stress measurements are made during exponential shear using mechanical means. The model is capable of explaining all trends seen in the data, and suggests a novel analysis of the data. This analysis demonstrates that exponential shearing flow is no more capable of stretching polymer chains than is inception of steady shear at comparable instantaneous shear rates. In fact, all exponential shear flow stresses measured are bounded quantitatively by stress measurements taken during inception of steady shear. Information taken from the model about chain stretching suggests that normal stress measurements are strong indications of stretching, whereas shear stress measurements are indicative of both chain stretching and segment orientation. [1]

4.1 Introduction

There has been considerable interest in the exponential shearing flow of viscoelastic liquids during the past fifteen years (Doshi and Dealy, 1987; Zülle *et al.*, 1987; Demarquette and Dealy, 1992; Venerus, 2000). Most interest centers around the desire to stretch chains in a manner similar to that accomplished in elongational flows, which are rather difficult to perform. On the contrary, many shear rheometers can be programmed to accomplish exponential shearing flow.

Arguments supporting the expectation of a similarity between the two flows rely on the same time dependence of the two invariants of the Cauchy strain tensor in the two flows (the third invariant being constant for an incompressible fluid). However, such observations do not take into account the vorticity arising in shearing flows—an effect that has not escaped most researchers, but is difficult to assess quantitatively (Astarita, 1979).

[1] This part of the work has been published in *J. Rheol.*, **44**(5), 1043–1054 (2000).

We argue here that exponential shearing flow *does* indeed stretch chains. However, *chains are equally stretched during inception of steady shear*. To support this argument, we demonstrate the following.

1. Using a successful reptation model with a single adjustable parameter fit using linear viscoelasticity (LVE) (Hua and Schieber, 1998; Hua *et al.*, 1998, 1999), we are able to obtain good agreement with exponential shear flow data.

2. When plotted as a function of the instantaneous shear rate, model predictions show that the segment orientations, as seen in the extinction angle, rapidly approach the steady-state orientations observed in steady shear flow.

3. Model predictions show that chain stretching grows monotonically with time, and follows along a master curve when plotted as a function of shear rate. The master curve is exactly that seen in steady shear flow. Similar results are seen for both the simulated and measured extinction angle.

4. The previous two observations suggest plotting the shear stress and first normal stress difference as functions of instantaneous shear rate in exponential shearing flow. When this is done, we see that both the shear stress and the normal stress follow the steady shear flow stresses, and do not exceed the stresses observed during inception of steady shear.

5. Based on these observations, we conclude that exponential shearing flow stretches entangled, linear polymer chains no more than does inception of steady shear.

These are our conclusions. We describe the experimental details and the simulation methods in Sections 4.2 and 4.3. The results of Sections 4.2 and 4.3 are presented in Section 4.4, and finally, an analysis is given in Section 4.5.

4.2 Experiment

The test fluid is a solution in tricresyl phosphate of nearly monodisperse polystyrene with a molecular weight M_w of 1.9×10^6 (polydispersity index of 1.2) at a polymer concentration n of 0.135 g/cm^3. Extensive data sets in single- and double-step strain flows, inception of steady shear, steady shear, and cessation of steady shear for this fluid have been reported (Venerus and Kahvand, 1994a,b) and were found to be in excellent agreement with predictions from the model considered in this study (Hua and Schieber, 1998; Hua *et al.*, 1998, 1999).

Rheological experiments were made on a Rheometrics Mechanical Spectrometer (RMS-800). Torque and axial thrust data from tests conducted in the cone and plate geometry were converted to values of shear stress σ^{e} and first normal stress difference N_1^{e} using established relations. The effects of transducer compliance on transient normal stress measurements were effectively eliminated by appropriate selection of the cone diameter and cone angle (Venerus and Kahvand, 1994b; Kahvand, 1995), although this limited somewhat the range of available shear strains. All tests were conducted at 23°C and reported data are averages of at least three runs.

For an exponential shear flow, the strain is given by

$$\gamma(t) = \exp(\alpha t) - \exp(-\alpha t), \tag{4.1}$$

where α is a parameter governing the shear acceleration.

The exponential shear history given in Eq. (4.1) was generated by controlling the angular position (dynamic mode) of the actuator in the RMS-800. In this mode, the range of angular rotation of the plate is ± 0.5 rad. The full range of angular rotation was exploited by first rotating the plate to one extreme (-0.5 rad) and holding the strain constant for a period of time (600 s) long enough for the fluid to relax (Venerus, 2000). This angular position established a new zero from which the plate could be rotated (in the positive direction) one full radian.

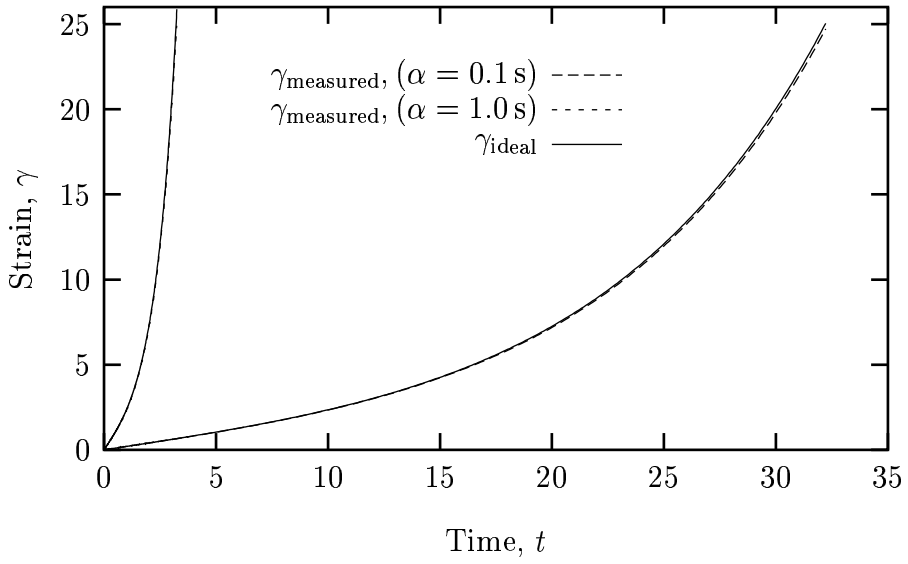

Figure 4.1. Measured strain for two exponential shear experiments.

For shear stress measurements a cone angle of 0.04 rad was used, allowing a maximum strain of 25; for normal stress measurements a cone angle of 0.1 rad was used, making the maximum strain 10. Figure 4.1 shows the measured exponential strain history for two values of α compared to the ideal history given in Eq. (4.1). From this figure it appears that deviations from the ideal strain history are small.

4.3 Theory

The model consists of $N+1$ beads attached by N finitely extendible entropic springs in a constraining tube. Therefore, there are $N+1$ dynamic variables describing the monomer density in the tube, and $3Z$ dynamic variables describing the length and orientation of each tube segment. The beads experience frictional forces with the affinely deforming tube, entropic spring forces, and Brownian forces. Dynamics of the chain ends determine death and creation of the tube segments according to the standard reptation picture. In addition, a mean-field constraint release (CR) mechanism similar to that pictured by Tsenoglou (1987) and des Cloizeaux (1988) weakly couples the chains. A Kramers-type expression is used to relate chain dynamics and macroscopic stress. The resulting expression is closely related to that derived for networks. The reader is referred to articles by Hua and Schieber (1998) and by Hua *et al.* (1998) for more details of the model.

Before simulations begin it is necessary to specify three parameters in the model: $\langle Z\rangle_{\rm eq}$, the average number of entangled chain segments at equilibrium; $N+1$, the number of beads; and b, the finite extensibility parameter. The first depends upon the chemistry of the chain, and may be found in standard texts (Ferry, 1980), based upon molecular weight M and entanglement molecular weight $M_{\rm e}$ of the system studied. The second parameter is found from the first as $N = 3\langle Z\rangle_{\rm eq}$, as before. The third parameter may also be found from standard references, and depends upon molecular weight and stiffness of the chain.

In this work, we use $\langle Z\rangle_{\rm eq} = 7$, which is reasonably consistent with the value estimated for the entangled polystyrene solution discussed above. The finite extensibility parameter, b, is picked to be 150 in all simulations. For $N/\langle Z\rangle_{\rm eq} = 3$, this value corresponds to 150 Kuhn steps per entanglement molecular weight $M_{\rm e}$, or 17 monomers per Kuhn step. This value of b is consistent with the experimental system considered (Flory, 1988, p.39). Too small of a value was used by Hua *et al.* (1999); however, the results given previously were not sensitive to finite extensibility, as a comparison with $b = \infty$ results showed.

From a single equilibrium simulation, the final adjustable parameter can be found: the disengagement time, $\tau_{\rm d}$. Therefore, for all nonlinear flow comparisons (previously, or in this article), no adjustable parameters have been used.

The simulated flow field is $v_y = v_z = 0$, and $v_x = \dot\gamma(t)y$, where the dot indicates a time derivative. Because the shear rate can change rather dramatically during exponential shear, an adaptive time-step-size algorithm was adopted during the simulation. The time-step size was chosen to always be the minimum of two criteria. The first criterion was a constant size ranging from $0.4\lambda_{\rm H}$ for the lowest α value to $0.05\lambda_{\rm H}$ for the highest ($\lambda_{\rm H} = \pi^2\tau_{\rm d}/2N^3$ is the Hookean time constant associated with a single

elastic chain segment). The choice was found to show convergent stress calculations during inception of steady shearing flow for low to moderate Deborah numbers, respectively. The second criterion prevented the total strain increment during a time step from exceeding 0.02. Simulation results showed no discernible sensitivity to further restrictions in the time-step-size criterion.

4.4 Results

Time const, λ_i/τ_d	Weight, g_i/G_N	Standard error
0.00066667	0.39876	0.017037
0.0021082	0.047667	0.015275
0.0066667	0.088504	0.011750
0.021082	0.113591	0.011750
0.066667	0.109303	0.011750
0.21082	0.088596	0.010869
0.66667	0.130553	0.006756
2.1082	0.022917	0.002144
6.6667	0.0001034	0.0002232

Table 4.1. Discrete relaxation spectrum fit to $G^*(\omega)$ experiments.

To characterize the linear viscoelastic properties of the polystyrene solution, small-amplitude oscillatory shear flow measurements were performed, and these data were used to fit the relaxation modulus to a discrete spectrum of relaxation times (Venerus and Kahvand, 1994a). The resulting spectrum is given in Table 4.1, in which the weights, g_i, are normalized by the plateau modulus, $G_N = \sum_i g_i \approx 3400\,\text{Pa}$. To find the linear viscoelastic predictions of the model, an equilibrium Brownian dynamics simulation exploiting linear response theory (Résibois and Leener, 1977, p.302) was used to calculate the relaxation modulus directly. The results are shown in Figure 4.2. These results were used to fit the discrete spectrum shown in Table 4.2. Also shown in the figure is the result of this fit, and the resulting residuals. All linear viscoelastic (LVE) results shown

Time const, λ_i/τ_d	Standard error	Weight, $g_i/nkTN$	Standard error
0.0030954	0.0004732	0.01726	0.00162
0.047955	0.0010604	0.04132	0.00050
0.51891	0.003926	0.12490	0.00063
2.2252	0.09639	0.01461	0.00082

Table 4.2. Discrete relaxation spectrum fit to the $G(t)$ simulation results shown in Figure 4.2.

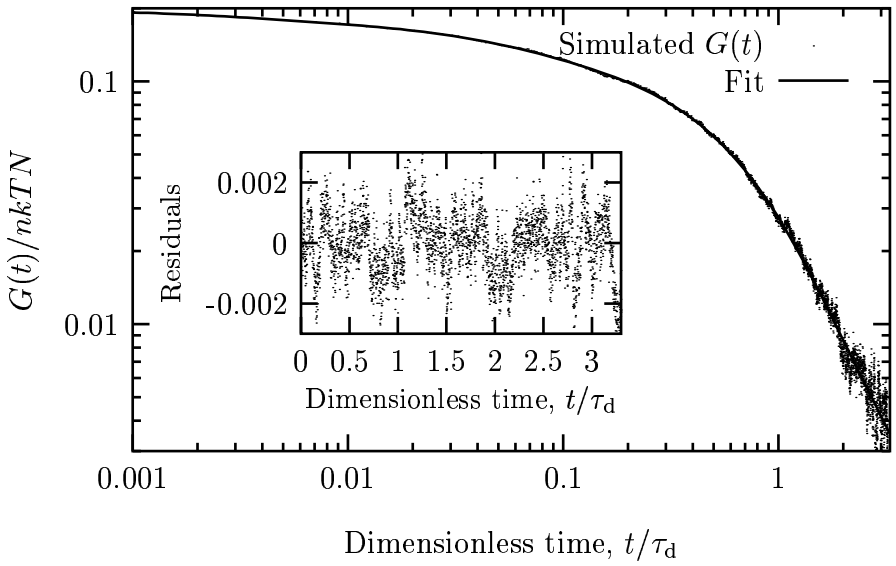

Figure 4.2. Relaxation modulus simulated using linear response theory for the reptation model. Shown in the inset are the residuals for the fit, $[G_{\rm sim}(t) - G_{\rm fit}(t)]/nkTN$.

below are taken from the experimental and simulated spectra in Tables 4.1 and 4.2 respectively.

From the simulated spectrum in Table 4.2 we obtain $\eta_0 = \sum_i g_i\lambda_i \approx 0.0994\tau_{\rm d}nkTN$ and $\Psi_{1,0} = 2\sum_i g_i\lambda_i^2 \approx 0.212\tau_{\rm d}^2nkTN$. This provides an estimate for the mean relaxation time $\tau_{\rm m} = \Psi_{1,0}/2\eta_0 \approx 1.068\tau_{\rm d}$, which can be compared with the corresponding experimental value. The weighted averages of the relaxation time constants found for the polystyrene solution yield $\eta_0 = 8400\,{\rm Pa\,s}$, $\Psi_{1,0} = 260000\,{\rm Pa\,s^2}$ and $\tau_{\rm m} = \Psi_{1,0}/2\eta_0 \approx 15{\rm s}$. Therefore, from linear viscoelastic measurements alone we fit the only adjustable parameter in the model: $\tau_{\rm d} \approx 15\,{\rm s}$. It is noticed that the experimental results found here are slightly different from previously reported values (Venerus and Kahvand, 1994a), probably because of slight evaporation of solvent.

4.4.1 Shear stress

At least three different exponential-shear-flow viscosities have been proposed to date. Each of these material functions is intended to test for strain hardening in a material. The most demanding criterion for strain hardening of these three material functions, suggested by Doshi and Dealy (1987),

$$\eta^{\rm e} = \frac{\sigma^{\rm e}(\alpha, t)}{2\dot{\gamma}(t)}, \tag{4.2}$$

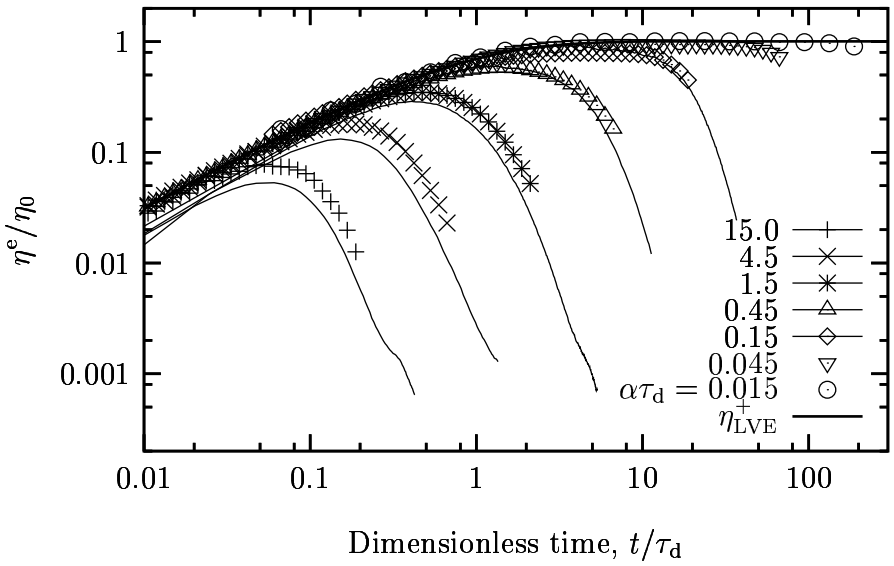

Figure 4.3. Viscosity function suggested by Doshi and Dealy (1987) for exponential shearing flow. Simulation results are shown as solid lines and data as symbols. The bold line is viscosity during inception of steady shear for zero shear rate.

is shown in Figure 4.3. The figure shows why this material function is so demanding: the shear stress must grow faster than the ever-accelerating shear rate to exhibit an upturn in the curves. Similar results were seen by Demarquette and Dealy (1992). For normalization of the theoretical predictions, the zero-shear-rate viscosity is estimated from inception of steady shear flow to be approximately $0.1292\ \tau_d nkTN$.

We first note that the model is able to capture this material function reasonably well, although the shapes of the curves are not particularly demanding. We also note that the simulations are able to obtain arbitrarily large shear rates and strains, whereas the experimental data are limited by the capabilities of the rheometer.

The ability of the model to extend beyond the data to longer times is more important in the second material function, $\sigma^e/2\alpha$, which was first considered by Zülle *et al.* (1987), and is shown in Figure 4.4.

Here we find that the model captures several subtle features of the data, such as the dependence of the position of the local maximum on α. Interestingly, the model shows a further increase in shear stress at strains currently inaccessible experimentally. These results will be made clear in Section 4.5.

4.4.2 Normal stress

The first normal stress difference N_1^e normalized by $4\alpha^2$ is shown in Figure 4.5. Using birefringence Demarquette and Dealy (1992) measured

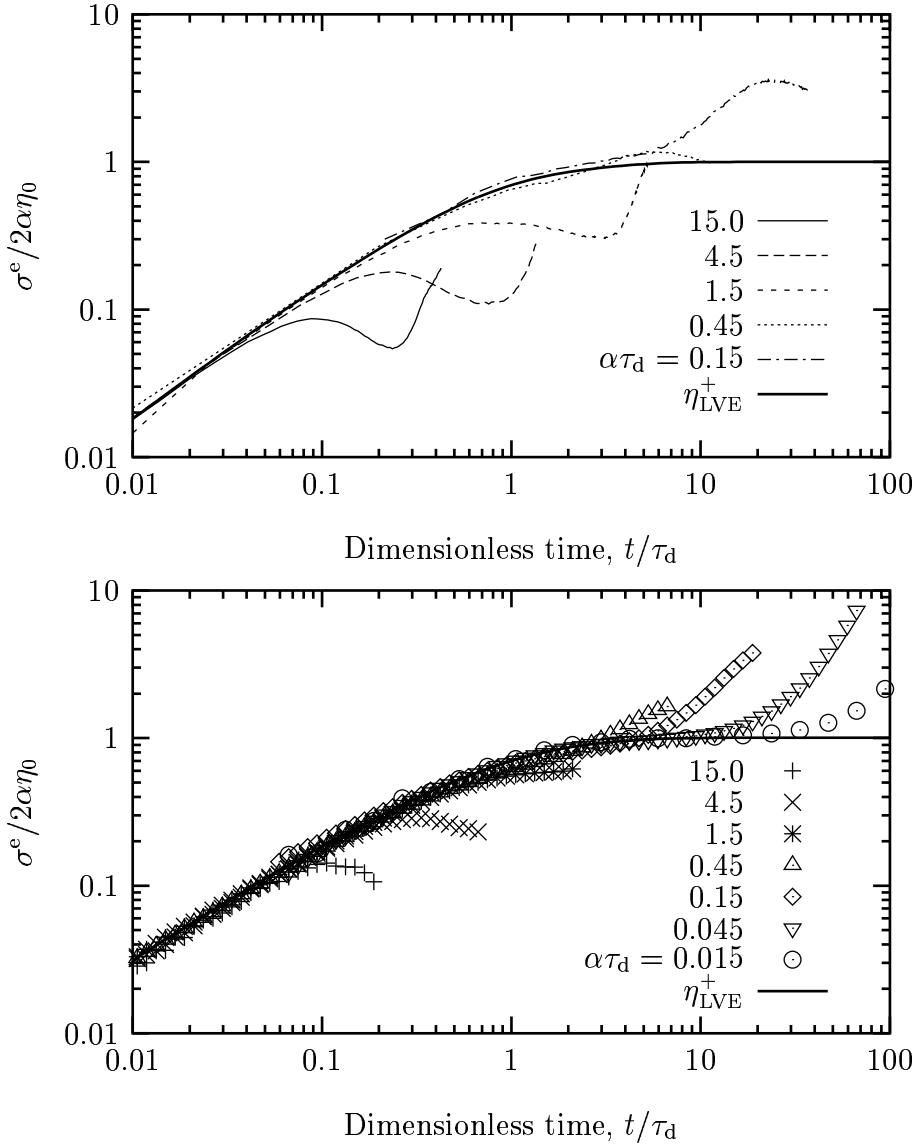

Figure 4.4. Dimensionless shear stress as a function of dimensionless time. The simulations are on the top, and the data are on the bottom.

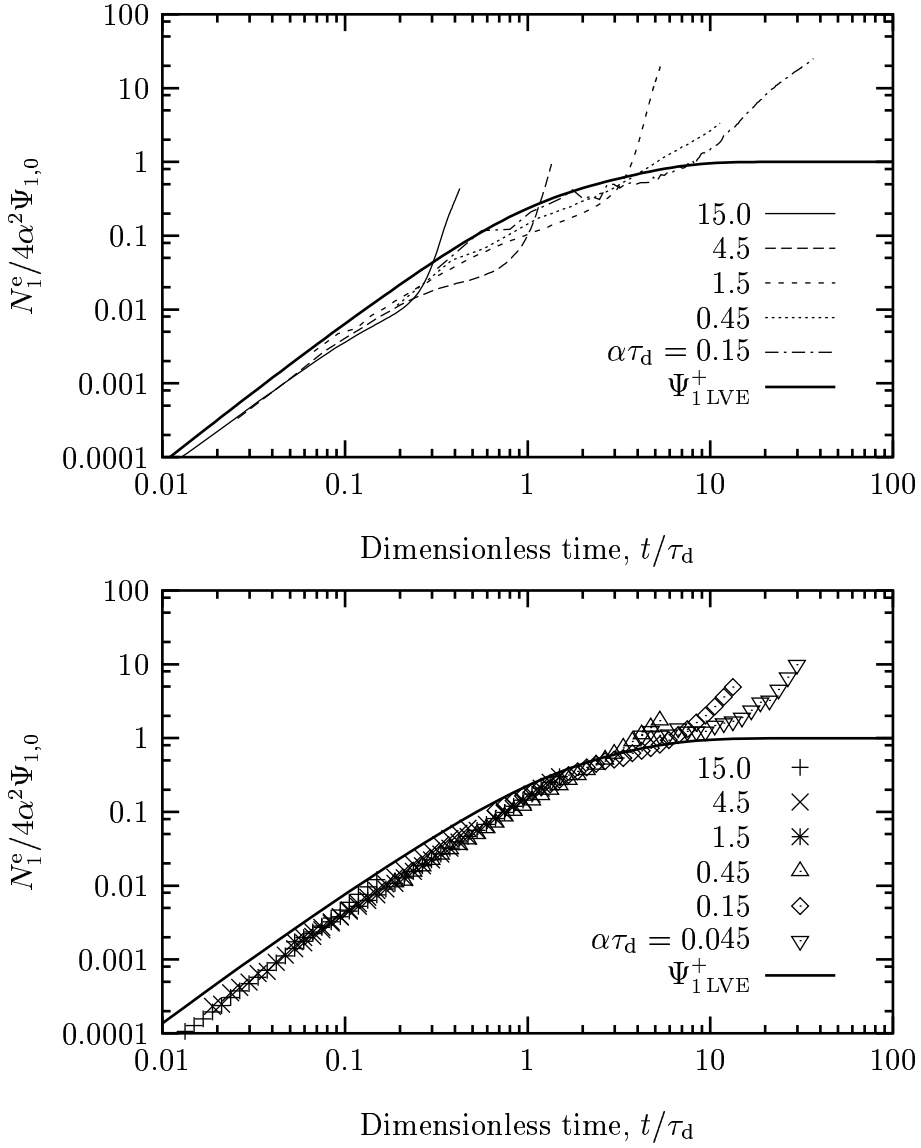

Figure 4.5. Dimensionless first normal stress as a function of dimensionless time. The simulations are on the top, and the data are on the bottom.

the third normal stress difference. The normal stress data shown here appear to be the first of their kind in exponential shear for an entangled polymer solution. To normalize the theoretical curves, the zero-shear-rate first normal stress coefficient was estimated from steady shear flow results to be approximately $0.403\ \tau_{\mathrm{d}}^2 nkTN$.

Except at the lowest values for α, the data show little deviation from the LVE curve, whereas the model predicts rather large upturns at the experimentally inaccessible longer times. These upturns are important indications of chain stretching, as is shown below.

For the time being we may conclude that the reptation model is able to capture the measured stresses well. However, in Section 4.5 we show that the model captures important connections to steady shear flow.

4.5 Analysis

The key to understanding the data shown in Section 4.4 lies in understanding how vorticity affects chain-segment orientation and chain stretching. A reasonable measure of the average orientation of chains is the extinction angle, χ, as estimated from stresses

$$\chi = \frac{1}{2}\tan^{-1}(2\sigma^{e}/N_1^{e}). \tag{4.3}$$

The angle χ, which could also be measured from birefringence, gives us an idea of how closely the chain segments are aligned with the flow direction. Such an angle is important, among other reasons, because the ability of shear flow to stretch the chains is proportional to how closely the chains are aligned at 45°. As the chains align more strongly with the flow ($\chi \to 0$), they are stretched less strongly by the flow. However, for any given orientation they are pulled more strongly by increasing shear rate. Hence, the flow field causes competing effects: stretching by shear rate, and vorticity tending to align the chains in the flow direction.

Figure 4.6 shows the extinction angle as a function of instantaneous shear rate for several values of α. Since the chains begin at equilibrium, their initial extinction angle must be isotropic: 45°. Hence, every curve begins at ($\dot{\gamma} = 2\alpha$, $\chi = 45°$) in this plot. We see that the model captures the shapes of these curves nicely. But most interesting is the observation that the extinction angle approaches the steady-state extinction angle found

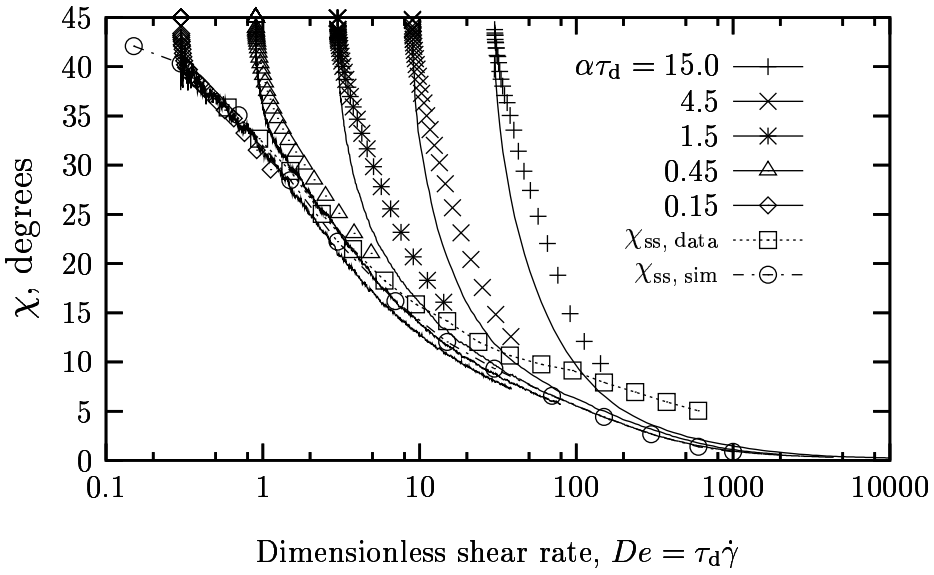

Figure 4.6. Extinction angle as a function of shear rate for several values of the shear acceleration α. As before, simulations are shown as solid lines and data as symbols. Also shown is the steady-state extinction angle χ_{ss} found in steady shearing flow (simulation: circles; data: squares).

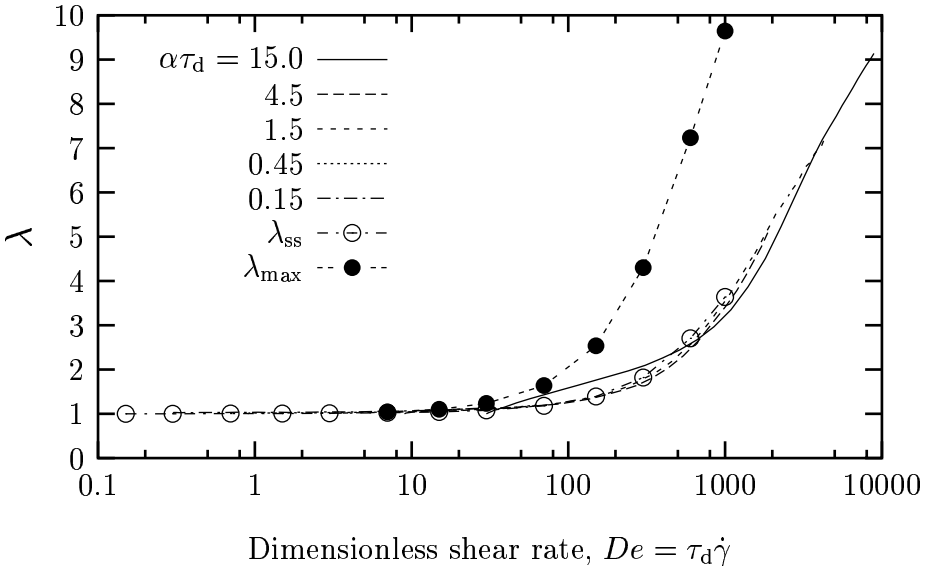

Figure 4.7. Normalized average chain stretching as a function of shear rate for several values of the shear acceleration as predicted by the model. Also shown are the predictions for chain stretching in steady shear (○), and the maximum stretching seen during inception of steady shear (●).

from steady shear in an overdamped fashion. This approach is not too surprising, since the extinction angle during inception of steady shear is only slightly underdamped (Hua *et al.*, 1999), and here the shear rate keeps accelerating.

Unfortunately, there are insufficient normal stress data to test the model's predictions completely. However, the lower values of α are clearly in agreement with the model, and the higher values are at least consistent.

Since the chains' orientations are well described by the steady shear observations, we might expect the stretching of the chains to exhibit similar behavior. Indeed, Figure 4.7 shows the model's predictions of average chain stretching (relative to equilibrium) as a function of instantaneous shear rate for several values of α. Again, we find that the simulation results follow along a master curve determined by steady shear flow results. However, just as during inception of steady shear, the largest α exhibits an overshoot in stretching, relative to the stretching at steady shear. Unfortunately, no experimental measure of stretching is available to test these results.

On the other hand, this physical picture does suggest a simple comparison of the stresses to test our hypothesis: plot both unadulterated shear stress and first normal stress difference as functions of shear rate (aside from a possible time scale factor and a stress factor), and include the steady shear stress data. These comparisons are made in Figures 4.8 and 4.9.

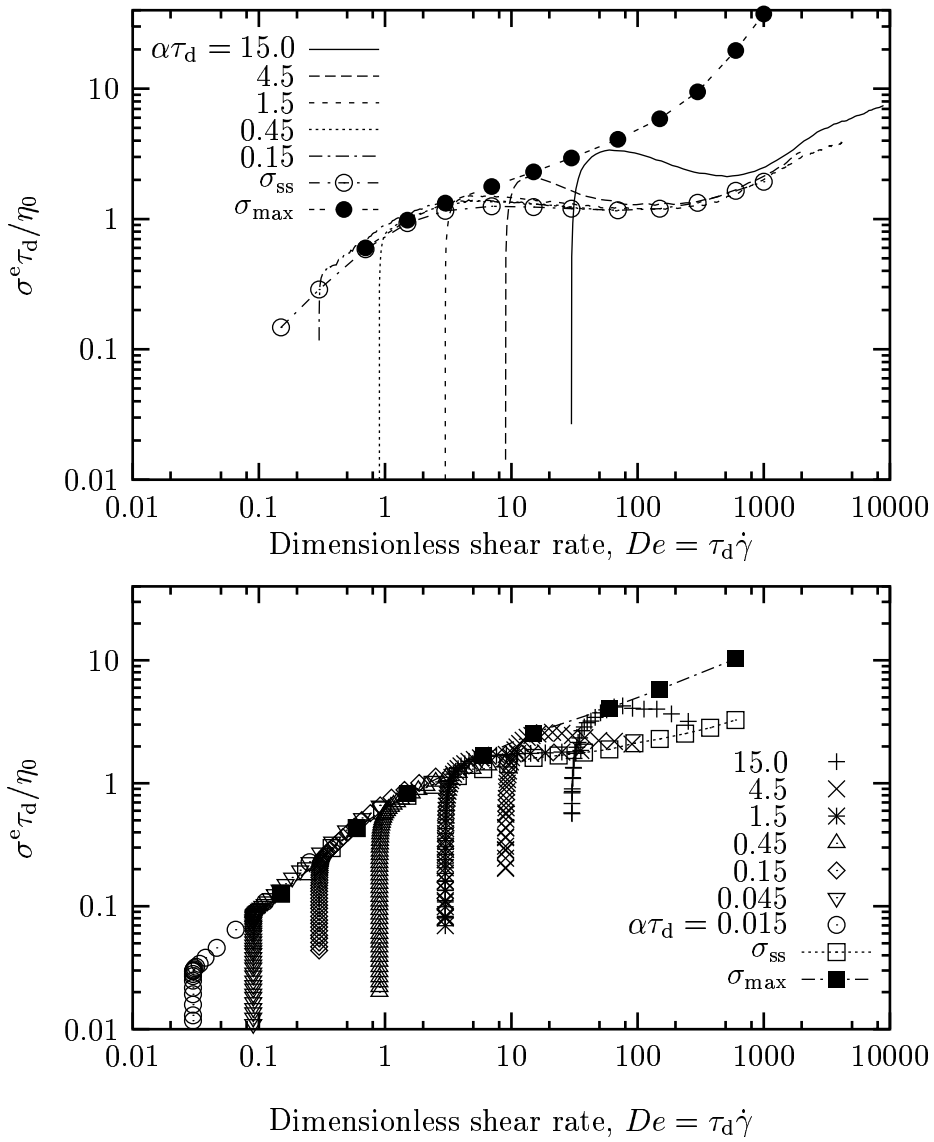

Figure 4.8. Shear stress (made dimensionless by LVE properties) as a function of instantaneous dimensionless shear rate for several values of the shear acceleration. Also shown are the curves for steady shear stress σ_{ss} and maximum shear stress σ_{max} during inception of steady shearing flow. The simulation results are on the top, and the data are on the bottom.

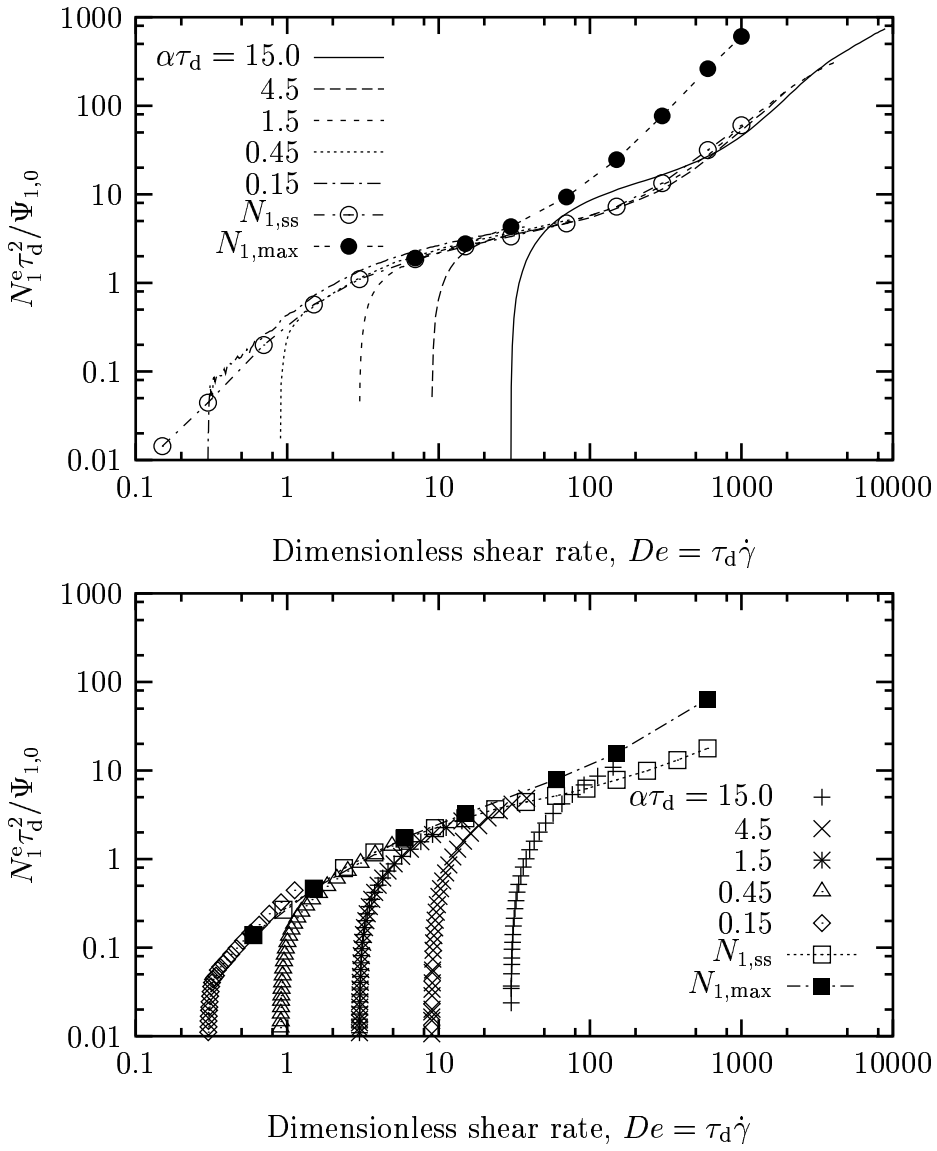

Figure 4.9. Normal stress (made dimensionless by LVE properties) as a function of dimensionless shear rate for several values of the shear acceleration. Also shown are the curves for steady normal stress $N_{1,ss}$, and maximum normal stress $N_{1,max}$ during inception of steady shearing flow. The simulation results are on the top, and the data are on the bottom.

The model shows that the shear stress rises very quickly to follow the master curve determined by the steady shear curve. It also shows that large values of α exhibit an overshoot. However, the magnitude of the overshoot is enveloped by the overshoot that is exhibited during inception of steady shear. The simulations are again in good agreement with the experimental data. Similar behavior is seen in the normal stress, although there is somewhat less experimental data to confirm the model.

We therefore conclude that exponential shearing flow stretches chains no greater than does inception of steady shear. Neither does it give rise to any greater stresses.

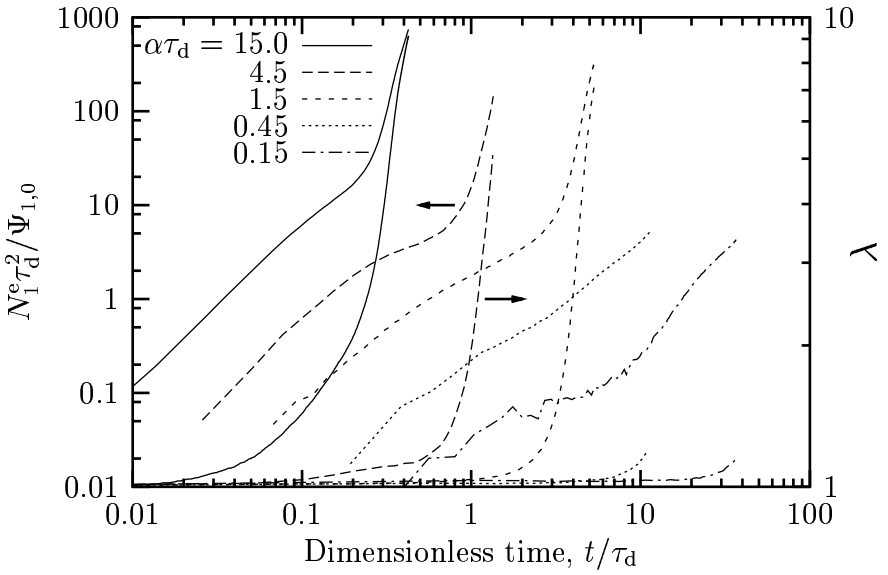

Figure 4.10. Simulated normal stress as a function of dimensionless time for several values of the shear acceleration. Also shown is the corresponding average chain stretching normalized by the equilibrium chain length.

It may also be of practical importance to experimentalists to be able to estimate when chain stretching is important. It is clear from the above figures that shear stress is not a reasonable measure. However, Figure 4.10 shows that the model exhibits a strong correlation between normal stress and stretch for exponential shear. Also, note that the rapid upturn in stretch, and hence also N_1^e, occurs when the instantaneous shear rate becomes large compared to the Rouse relaxation time: $\dot{\gamma}\tau_R = \dot{\gamma}\tau_d/N \gg 1$. Similar observations were made for inception of steady shear (Hua *et al.*, 1999).

Finally, we consider the viscosity proposed by Doshi and Dealy (1987) for exponential shearing flow, which is the difference in the principal stresses over the instantaneous shear rate,

$$\eta_1^e(\alpha, t) = \frac{\sqrt{4\sigma^e(\alpha, t)^2 + N_1^e(\alpha, t)^2}}{2\dot{\gamma}(\alpha, t)}. \tag{4.4}$$

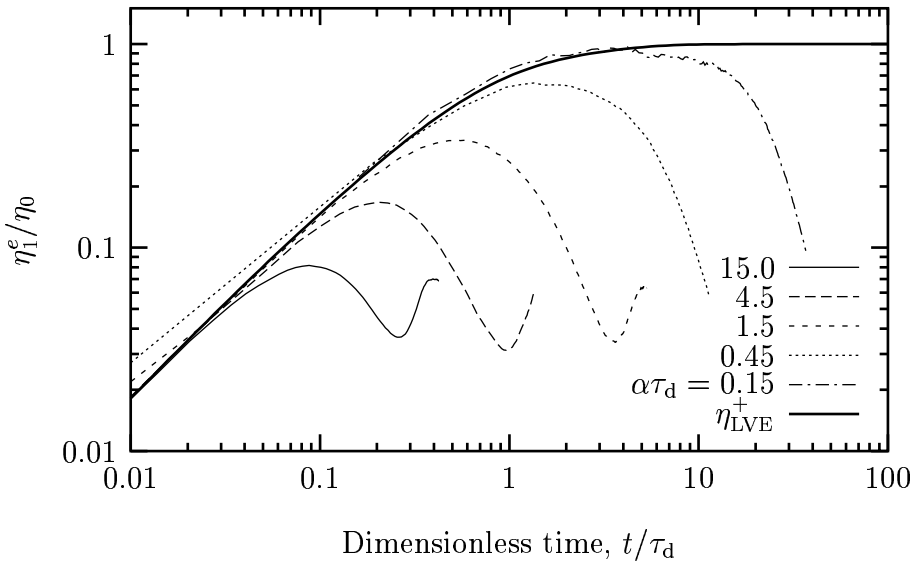

Figure 4.11. Viscosity based on the principal stress difference as predicted by the model for several values of the shear acceleration parameter α.

The normal stress data do not extend far enough in strain to examine whether this material function ever grows larger than the LVE curve. However, the model may be simulated for much greater times. Figure 4.11 shows the model predictions for $\eta_1^e(\alpha, t)$ versus time. Although the viscosity does begin to rise again, it never reaches the LVE predictions, even for strains up to 2900 for $\tau_d\alpha = 1.5$! In fact, at these large strains, the material function appears to reach a plateau or downturn. This lack of "strain-rate hardening" occurs despite the fact that the chains are stretching very dramatically.

The model therefore predicts that the proposed viscosity will never exhibit strain-rate hardening behavior in any practicable experiment for linear, entangled polymer chains in shear flow.

Acknowledgments

One of the authors (J.N.) would like to thank the Danish government for financial support through the Technical University of Denmark (DTU), and the Kaj and Hermilla Ostenfeld fund.

References

Astarita, G. (1979). Objective and generally applicable criteria for flow classification. *J. Non-Newtonian Fluid Mech.*, **6**, 69–76.

Demarquette, N. R. and Dealy, J. M. (1992). Nonlinear viscoelasticity of concentrated polystyrene solutions: Sliding plate rheometer studies. *J. Rheol.*, **36**(6), 1007–1032.

des Cloizeaux, J. (1988). Double reptation vs. simple reptation in polymer melts. *Europhys. Lett.*, **5**, 437–442.

Doshi, S. R. and Dealy, J. M. (1987). Exponential Shear: A Strong Flow. *J. Rheol.*, **31**(7), 563–582.

Ferry, J. L. (1980). *Viscoelastic Properties of Polymers*. John Wiley & Sons, New York, third edition.

Flory, P. J. (1988). *Statistical Mechanics of Chain Molecules*. Hanser, Munich.

Hua, C. C. and Schieber, J. D. (1998). Segment connectivity, chain-length breathing, segmental stretch, and constraint release in reptation models. I. Theory and single-step strain predictions. *J. Chem. Phys.*, **109**(22), 10018–10027.

Hua, C. C.; Schieber, J. D. and Venerus, D. C. (1998). Segment connectivity, chain-length breathing, segmental stretch, and constraint release in reptation models. II. Double-step strain predictions. *J. Chem. Phys.*, **109**(22), 10028–10032.

Hua, C. C.; Schieber, J. D. and Venerus, D. C. (1999). Segment connectivity, chain-length breathing, segmental stretch, and constraint release in reptation models. III. Shear Flows. *J. Rheol.*, **43**(3), 701–717.

Kahvand, H. (1995). *Strain Coupling Effects in Polymer Rheology*. Ph.D. thesis, Illinois Institute of Technology.

Résibois, P. and Leener, M. D. (1977). *Classical Kinetic Theory of Fluids*. John Wiley and Sons, New York.

Tsenoglou, C. (1987). Viscoelasticity of binary homopolymer blends. *Am. Chem. Soc. Polym. Preprints*, **28**, 185.

Venerus, D. C. (2000). Exponential Shear Flow of Polymer Melts. *Rheol. Acta*, **39**, 71–79.

Venerus, D. C. and Kahvand, H. (1994a). Doi-Edwards theory evaluation in double-step strain flows. *J. Polym. Sci., Polym. Phys. Ed.*, **32**, 1531–1542.

Venerus, D. C. and Kahvand, H. (1994b). Normal stress relaxation in reversing double-step strain flows. *J. Rheol.*, **38**, 1297–1315.

Zülle, B.; Linster, J. J.; Meissner, J. and Hürlimann, H. P. (1987). Deformation Hardening and Thinning in Both Elongation and Shear of a Low Density Polyetyhylene Melt. *J. Rheol.*, **31**(7), 583–598.

5

A Full-Chain, Temporary Network Model with Sliplinks, Chain-length Fluctuations, Chain Connectivity and Chain Stretching

A full-chain, temporary network model is proposed for nonlinear flows of linear, entangled polymeric liquids. The model is inspired by the success of a recent reptation model, but contains no tubes. Instead, each chain uses a different (and smaller) set of dynamic variables: the location of each entanglement, and the number of Kuhn steps in chain strands between entanglements. However, the model requires only a single phenomenological parameter that is fit by linear viscoelasticity. The entanglements are assumed to move affinely, whereas the number of Kuhn steps varies stochastically from tension imbalances and Brownian forces. In the language of reptation, the model exhibits chain connectivity, chain-length fluctuations, chain stretching, and tube dilation. Constraint release is not considered in this version of the model, but it is straight forward to subsequently include this concept in the theory. A simulation algorithm is described in detail, and some linear viscoelastic predictions of the model are made. Finally, we make a few flow simulations and consider possible future generalizations of the proposed model.

5.1 Introduction

A recently proposed reptation model (Hua and Schieber, 1998) has been shown to make good quantitative comparison with stresses in double-step strains (Hua *et al.*, 1998), inception and relaxation of steady shearing flows, steady shearing flows (Hua *et al.*, 1999), and exponential shear flows (Neergaard *et al.*, 2000). In fact, the model was essential in guiding our understanding of exponential shear flows and their connection to steady shearing flows (see Chapter 4 of this thesis).

This previous model incorporates chain connectivity, chain-length fluctuations, chain stretching and constraint release; this last effect is incorporated in a self-consistent, mean-field way, but the other effects follow in a self-consistent manner from the mechanical model proposed. The model uses one phenomenological parameter: a monomeric friction coefficient that is fixed from equilibrium data. All nonlinear viscoelastic predictions are then made without adjustable parameters.

Despite the good agreement with experiments on an entangled polystyrene solution, some drawbacks remain. First, the model is somewhat expensive computationally, prohibiting its use in most complex geometry calculations. Secondly, there are still some discrepancies with data: the steady-state extinction angle approaches zero with increasing shear rate instead of reaching a plateau, and the magnitude of the overshoots in viscosity and normal stress during inception of steady shear is overpredicted.

The physical implications of these discrepancies with experiment are not yet clear. The discrepancy in overshoot magnitude may be related to excessive stretching of the chain during the transient flow. This extra stretching may be related to the existence in the model of artificial Brownian particles, or beads in the chain. Surprisingly, models containing very similar physics, but on a lower level of description do not show this problem (Mead *et al.*, 1998; Öttinger, 1999; Fang *et al.*, 2000).

In this work, we propose a new mean-field model which incorporates the useful features of the earlier tube model, but avoids these drawbacks. In the following section we describe the dynamical model proposed. The evolution equation for the model is found, and in Section 5.3 explicit expressions for the chain free energies are considered. We describe a simulation algorithm in Section 5.4, and using this algorithm we investigate some linear viscoelastic properties of the model in Section 5.5. A problem with the free energy expressions is discussed in Section 5.6. An alternative expression for the free energy is suggested, and some shear flow simulations are made. Finally, in Section 5.7 we discuss options for future work and possible generalizations of the proposed theory.

5.2 Model Description

The model uses the following dynamical variables for a single mean-field chain.

- There are $Z(t)$ entanglements in the chain. Hence, there exist $Z-1$ entangled strands, and a total of $Z+1$ strands in the network. This value can fluctuate, but has an equilibrium value $Z_{\mathrm{eq}} \equiv \langle Z \rangle_{\mathrm{eq}}$ given by the molecular weight M divided by the entanglement molecular weight M_{e}. Usually it is more convenient to use the labels for the front and back strands, $i_{\mathrm{f}}(t)$ and $i_{\mathrm{b}}(t)$, which are allowed to fluctuate among integer values such that $i_{\mathrm{f}} \geq i_{\mathrm{b}}$ and $Z = i_{\mathrm{f}} - i_{\mathrm{b}}$.

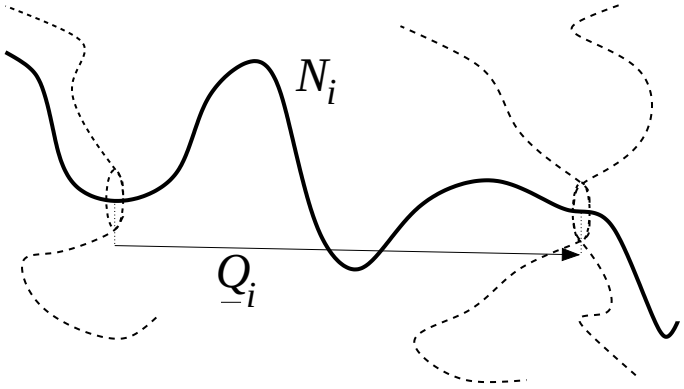

Figure 5.1. Schematic of the dynamic variables in the model. The curves indicate the positions of each of the Kuhn steps in the strands, but such information is averaged out in the model. Instead, only the positions of the entanglements and the number of Kuhn steps in each strand are known, and the strands are assumed to sample available configurations on the time scale $N_e\,\tau_e$, the time scale of a single strand at equilibrium conditions.

- Strand i has $N_i(t)$ Kuhn steps.
- Each entanglement point on the chain has position $\boldsymbol{R}_i(t)$, $i = i_\mathrm{b}, \ldots, i_\mathrm{f}-1$, and the ends of the chain have positions $\boldsymbol{R}_{i_\mathrm{b}-1}$ and $\boldsymbol{R}_{i_\mathrm{f}}$. However, it is typically more convenient to keep track of the vectors connecting these entanglements along the chain $\boldsymbol{Q}_i(t) := \boldsymbol{R}_i - \boldsymbol{R}_{i-1}$, $i = i_\mathrm{b}, \ldots, i_\mathrm{f}$.

The physical picture described by the model is shown in Figure 5.1.

5.2.1 Statics

We wish the chain to have an equilibrium distribution given by

$$p^\mathrm{eq}(\Omega) = J^{-1} \exp\left[-\frac{F(\Omega)}{k_\mathrm{B}T}\right], \tag{5.1}$$

where the chain configuration is given by the shorthand notation $\Omega := \{\boldsymbol{Q}_i, N_i\}_{i_\mathrm{b}}^{i_\mathrm{f}} \equiv \boldsymbol{Q}_{i_\mathrm{b}}, \ldots, \boldsymbol{Q}_{i_\mathrm{f}}, N_{i_\mathrm{b}}, \ldots, N_{i_\mathrm{f}}$, J is a normalization constant, k_B is Boltzmann's constant, T is temperature, and F is the chain free energy

$$F = \sum_{i=i_\mathrm{b}+1}^{i_\mathrm{f}-1} F_\mathrm{S}(\boldsymbol{Q}_i, N_i) + F_\mathrm{E}(\boldsymbol{Q}_{i_\mathrm{b}}, N_{i_\mathrm{b}}) + F_\mathrm{E}(\boldsymbol{Q}_{i_\mathrm{f}}, N_{i_\mathrm{f}}), \tag{5.2}$$

where the free energies of an entangled strand F_S and end strand F_E must be specified. Examples for these are given in Section 5.3, but for the time being we may assume that they are Gaussian strands derived from a coarse-grained random walk (see Eq. (5.38)).

We now show that this *static, equilibrium* requirement greatly restricts the possible *dynamics* of the model. In other words, if we generalize the classical network picture in order to allow the chain to slide through the entanglements, we necessarily obtain the equilibrium model below (without constraint release). Generalization of the equilibrium model to affine motion is possible.

5.2.2 Dynamics

As in classical network theory, the entanglement points are assumed to move affinely. Therefore, we write the deterministic evolution of the entangled strand conformations as

$$\frac{d}{dt}\boldsymbol{Q}_i = \boldsymbol{\kappa}\cdot\boldsymbol{Q}_i, \quad i = i_\mathrm{b}+1,\ldots,i_\mathrm{f}-1, \tag{5.3}$$

where $\boldsymbol{\kappa} := (\boldsymbol{\nabla v})^\dagger$ is the transpose of the velocity gradient.

The free ends of the chain are assumed to diffuse from Brownian motion, and are not significantly oriented by the flow field. Hence, we write the stochastic differential equation (SDE) for the free ends as

$$d\boldsymbol{Q}_{i_\mathrm{b}} = -\frac{a_\mathrm{K}^2}{k_\mathrm{B}T\tau_e}\left(\frac{\partial F_\mathrm{E}}{\partial \boldsymbol{Q}_{i_\mathrm{b}}}\right)_{T,N_{i_\mathrm{b}}} dt + \sqrt{\frac{2a_\mathrm{K}^2}{\tau_e}}d\boldsymbol{W}_{i_\mathrm{b}}\ , \tag{5.4}$$

where $\boldsymbol{W}_{i_\mathrm{b}}(t)$ is a three dimensional vector of independent Wiener processes (Gardiner, 1982), and a_K is the length of a Kuhn step. This form of the SDE satisfies the fluctuation-dissipation theorem, and is necessary to guarantee satisfaction of Eq. (5.1). In Eq. (5.4), we have also introduced the single phenomenological parameter in the model, a characteristic time τ_e, which is the time scale associated with the motion of a single Kuhn step of a chain strand. This time scale, or rather $N_e\,\tau_e$ (N_e being the number of Kuhn steps corresponding to the entanglement molecular weight M_e), is already implied by the coarse-grained information used. Namely, when we assume that the free energy of the chain is given by $\Omega := \{\boldsymbol{Q}_i, N_i\}_{i_\mathrm{b}}^{i_\mathrm{f}}$, we assume that the strands can sample most of the configuration space available to them on the time interval $N_e\,\tau_e$, which becomes the smallest time scale resolved by the model.

Entanglements are created and destroyed only at the ends of the chains. During the periods of no entanglement creation or destruction, Kuhn steps may pass through the entanglement points (similar to sliplinks in the tube picture) because of Brownian forces or tension imbalances in the strands. These processes are assumed to be jump processes, instantaneous on the time scales resolved by the model.

Jump processes may be described using a differential Chapman-Kolmogorov equation (Gardiner, 1982). Incorporating these jump dynamics with

the diffusion and deterministic dynamics described above, we can completely specify the dynamics of the model in the following equation:

$$\begin{aligned}\frac{\partial p(\Omega;t)}{\partial t} &= -\sum_{i=i_\mathrm{b}+1}^{i_\mathrm{f}-1}\frac{\partial}{\partial \boldsymbol{Q}_i}\cdot[\boldsymbol{\kappa}\cdot\boldsymbol{Q}_i]\,p(\Omega)\\ &+\frac{\partial}{\partial \boldsymbol{Q}_{i_\mathrm{b}}}\cdot\left\{\frac{a_\mathrm{K}^2}{k_\mathrm{B}T\tau_e}\left[\left(\frac{\partial F_\mathrm{E}(\boldsymbol{Q}_{i_\mathrm{b}},N_{i_\mathrm{b}})}{\partial \boldsymbol{Q}_{i_\mathrm{b}}}\right)p(\Omega)+k_\mathrm{B}T\frac{\partial p(\Omega)}{\partial \boldsymbol{Q}_{i_\mathrm{b}}}\right]\right\}\\ &+\frac{\partial}{\partial \boldsymbol{Q}_{i_\mathrm{f}}}\cdot\left\{\frac{a_\mathrm{K}^2}{k_\mathrm{B}T\tau_e}\left[\left(\frac{\partial F_\mathrm{E}(\boldsymbol{Q}_{i_\mathrm{f}},N_{i_\mathrm{f}})}{\partial \boldsymbol{Q}_{i_\mathrm{f}}}\right)p(\Omega)+k_\mathrm{B}T\frac{\partial p(\Omega)}{\partial \boldsymbol{Q}_{i_\mathrm{f}}}\right]\right\}\\ &+\frac{1}{\tau_e}\int\left[W(\Omega|\Omega')p(\Omega')-W(\Omega'|\Omega)p(\Omega)\right]d\Omega',\end{aligned}\tag{5.5}$$

where $p(\Omega;t)\equiv p(\boldsymbol{Q}_{i_\mathrm{b}},\ldots,\boldsymbol{Q}_{i_\mathrm{f}},N_{i_\mathrm{b}},\ldots,N_{i_\mathrm{f}};t)$ is the probability density for a chain to have configuration Ω. We also use the vector notation, $\boldsymbol{N}$, for the number of Kuhn steps and the shorthand notation

$$\int\ldots d\Omega' := \sum_{i'_\mathrm{b}=i_\mathrm{b}-1}^{i_\mathrm{b}+1}\sum_{i'_\mathrm{f}=i_\mathrm{f}-1}^{i_\mathrm{f}+1}\sum_{\boldsymbol{N}'}\int\int\int\ldots d\{\boldsymbol{Q}'\}.\tag{5.6}$$

The first term on the right side of Eq. (5.5) is the affine entanglement deformation consistent with Eq. (5.3). The second and third terms are the Fokker-Planck-like terms equivalent to the SDEs, Eq. (5.4). The remaining terms are associated with the chain-end "boundary conditions" and "Kuhn step shuffling" between strands. Roughly speaking, the transition probability $\frac{1}{\tau_e}W(\Omega|\Omega')$ is the probability per unit time that a chain with configuration Ω' jumps to configuration Ω.

To specify the transition probability $W(\Omega|\Omega')$, it is useful to introduce the matrix $\bar{\boldsymbol{B}}$, whose elements are defined by (Bird *et al.*, 1987a, Eq. (11.6–5))

$$\bar{B}_{ij} := \delta_{i+1,j}-\delta_{ij},\tag{5.7}$$

where δ_{ij} is the Kronecker delta. We also introduce the vector $\boldsymbol{n}$ of $Z+2$ elements, whose ith element is the number of Kuhn steps that move from strand i to strand $i+1$. This vector also includes elements $n_{i_\mathrm{b}-1}$ and n_{i_f}, which are the number of Kuhn steps that can move into a newly created entanglement at the end. In a jump, only one Kuhn step is allowed to pass through an entanglement

$$n_i=\begin{cases}-1,0 & ,i=i_\mathrm{b}-1\\ -1,0,+1 & ,i=i_\mathrm{b},\ldots,i_\mathrm{f}-1\\ 0,+1 & ,i=i_\mathrm{f}\\ 0, & ,\text{otherwise.}\end{cases}\tag{5.8}$$

From the current configuration, it is possible to find the end labels i_b and i_f from the definitions

$$i_\mathrm{b} := \sum_{i\in\mathbb{Z}} iH(N_i)\delta_{0,N_{i-1}},\qquad i_\mathrm{f} := \sum_{i\in\mathbb{Z}} iH(N_i)\delta_{0,N_{i+1}},\tag{5.9}$$

where $H()$ is the Heaviside step function. Finally, we introduce the notation

$$\delta(\boldsymbol{N},\boldsymbol{N}') := \prod_{i=i_\mathrm{b}}^{i_\mathrm{f}} \delta_{N_i,N_i'}. \tag{5.10}$$

With these definitions, it is possible to write the transition probabilities in compact form

$$\begin{aligned} W(\Omega|\Omega') &= \sum_{\boldsymbol{n}} \delta(\boldsymbol{N},\boldsymbol{N}'-\bar{\boldsymbol{B}}\cdot\boldsymbol{n}) \prod_{i=i_\mathrm{b}}^{i_\mathrm{f}} \delta(\boldsymbol{Q}_i-\boldsymbol{Q}_i') \times \\ &\quad \exp\left[-\frac{F(\Omega)}{2k_\mathrm{B}T}+\frac{F(\Omega')}{2k_\mathrm{B}T}\right]. \end{aligned} \tag{5.11}$$

The first delta function above guarantees conservation of Kuhn steps in the chain by shuffling n_i Kuhn steps from strand i to strand $i+1$. The product of Dirac delta functions ensures that the strand conformations are unchanged by the shuffling of Kuhn steps. The exponential term is very important for two reasons. First, it guarantees detailed balance, so that Eq. (5.1) is satisfied. Secondly, it yields the physically reasonable mechanism of shuffling Kuhn steps from strands of low tension to strands of high tension on average. This point is made clearer in Section 5.2.3.

5.2.3 The continuous limit

In typical cases, the number of Kuhn steps in a chain is very large. Hence, we can approximate such a chain in the limit of a continuous number of N_i. To consider this limit, we focus on the master-equation-like portion of the differential Chapman-Kolmogorov equation, Eq. (5.5), which accounts for the shuffling of Kuhn steps between adjacent strands, and which may be written

$$\begin{aligned} \frac{\partial p}{\partial t} &= \frac{1}{\tau_e}\sum_{\boldsymbol{n}} \left\{ W_{\boldsymbol{n}}(\boldsymbol{N}|\boldsymbol{N}-\bar{\boldsymbol{B}}\cdot\boldsymbol{n}) p(\boldsymbol{N}-\bar{\boldsymbol{B}}\cdot\boldsymbol{n}) \right. \\ &\quad \left. - W_{\boldsymbol{n}}(\boldsymbol{N}-\bar{\boldsymbol{B}}\cdot\boldsymbol{n}|\boldsymbol{N}) p(\boldsymbol{N}) \right\}, \end{aligned} \tag{5.12}$$

where we have suppressed dependence on the strand orientation vectors $\{\boldsymbol{Q}_i\}$. We momentarily neglect the terms for entanglement creation and destruction. In the above, the transition probabilities are then written

$$W_{\boldsymbol{n}}(\boldsymbol{N}|\boldsymbol{N}-\bar{\boldsymbol{B}}\cdot\boldsymbol{n}) = \frac{\exp\left[-F(\boldsymbol{N})/2k_\mathrm{B}T\right]}{\exp\left[-F(\boldsymbol{N}-\bar{\boldsymbol{B}}\cdot\boldsymbol{n})/2k_\mathrm{B}T\right]}. \tag{5.13}$$

We can expand this probability in a Taylor's series around $\boldsymbol{n}=0$ to obtain

$$\begin{aligned} W_{\boldsymbol{n}}(\boldsymbol{N}|\boldsymbol{N}-\bar{\boldsymbol{B}}\cdot\boldsymbol{n}) &= 1+\frac{1}{2k_\mathrm{B}T}\left[-(\bar{\boldsymbol{B}}\cdot\boldsymbol{n})\cdot\left(\frac{\partial F}{\partial \boldsymbol{N}}\right)\right. \\ &\quad + \left.\frac{1}{2}(\bar{\boldsymbol{B}}\cdot\boldsymbol{n})(\bar{\boldsymbol{B}}\cdot\boldsymbol{n}) : \left(\frac{\partial^2 F}{\partial \boldsymbol{N}\partial \boldsymbol{N}}\right) - \ldots\right] \end{aligned} \tag{5.14}$$

to second order. Similarly, the expansion for the jump in the opposite direction is

$$W_{\boldsymbol{n}}(\boldsymbol{N}-\bar{\boldsymbol{B}}\cdot\boldsymbol{n}|\boldsymbol{N}) = 1-\frac{1}{2k_{\mathrm{B}}T}\left[-(\bar{\boldsymbol{B}}\cdot\boldsymbol{n})\cdot\left(\frac{\partial F}{\partial \boldsymbol{N}}\right)\right. + \left.\frac{1}{2}(\bar{\boldsymbol{B}}\cdot\boldsymbol{n})(\bar{\boldsymbol{B}}\cdot\boldsymbol{n}):\left(\frac{\partial^2 F}{\partial\boldsymbol{N}\partial\boldsymbol{N}}\right)-\ldots\right] \quad (5.15)$$

We can also expand the distribution function in $\boldsymbol{N}$ to obtain, to second order

$$p(\boldsymbol{N}-\bar{\boldsymbol{B}}\cdot\boldsymbol{n}) = p(\boldsymbol{N})-(\bar{\boldsymbol{B}}\cdot\boldsymbol{n})\cdot\left(\frac{\partial p}{\partial \boldsymbol{N}}\right) + \frac{1}{2}(\bar{\boldsymbol{B}}\cdot\boldsymbol{n})(\bar{\boldsymbol{B}}\cdot\boldsymbol{n}):\left(\frac{\partial^2 p}{\partial\boldsymbol{N}\partial\boldsymbol{N}}\right)-\ldots. \quad (5.16)$$

If we insert these expansions into the master equation, Eq. (5.12), and keep terms only to second order, we obtain the approximate expression

$$\begin{aligned}\frac{\partial p}{\partial t} = \frac{1}{\tau_e}\sum_{\boldsymbol{n}}\left\{\frac{p}{k_{\mathrm{B}}T}\left[-(\bar{\boldsymbol{B}}\cdot\boldsymbol{n})\cdot\left(\frac{\partial F}{\partial\boldsymbol{N}}\right)+\frac{1}{2}(\bar{\boldsymbol{B}}\cdot\boldsymbol{n})(\bar{\boldsymbol{B}}\cdot\boldsymbol{n}):\left(\frac{\partial^2 F}{\partial\boldsymbol{N}\partial\boldsymbol{N}}\right)\right]+\right.\\ (\bar{\boldsymbol{B}}\cdot\boldsymbol{n})\cdot\left(\frac{\partial p}{\partial\boldsymbol{N}}\right)\left[\frac{1}{2k_{\mathrm{B}}T}(\bar{\boldsymbol{B}}\cdot\boldsymbol{n})\cdot\left(\frac{\partial F}{\partial\boldsymbol{N}}\right)-1\right]+\\ \left.\frac{1}{2}(\bar{\boldsymbol{B}}\cdot\boldsymbol{n})(\bar{\boldsymbol{B}}\cdot\boldsymbol{n}):\left(\frac{\partial^2 p}{\partial\boldsymbol{N}\partial\boldsymbol{N}}\right)\right\}. \quad (5.17)\end{aligned}$$

Keeping in mind that element n_j in $\boldsymbol{n}$ is the number of Kuhn steps moving from strand j to $j+1$, conservation of the total number of Kuhn steps in the chain yields $\sum_j n_j = 0$, and since n_j can take values of $-1, 0$, or $+1$ only, $\sum_{j,k} n_j n_k = 2\delta_{jk}$. Hence, the sums occurring in the expansion above are

$$\sum_{\boldsymbol{n}}\bar{\boldsymbol{B}}\cdot\boldsymbol{n} = \sum_{ij}\boldsymbol{\delta}_i\bar{B}_{ij}\left(\sum_j n_j\right)=0, \quad (5.18)$$

$$\sum_{\boldsymbol{n}}(\bar{\boldsymbol{B}}\cdot\boldsymbol{n})(\bar{\boldsymbol{B}}\cdot\boldsymbol{n}) = \sum_{ijkm}\boldsymbol{\delta}_i\boldsymbol{\delta}_j\bar{B}_{ik}\bar{B}_{jm}\left(\sum_{k,m} n_k n_m\right)=2\boldsymbol{A}, \quad (5.19)$$

where $\boldsymbol{A}$ is a tensorial form of the Rouse matrix (Bird *et al.*, 1987a), defined as

$$A_{ij} = \begin{cases} +2 & , i=j \\ -1 & , i=j\pm 1 \\ 0 & , \text{otherwise.}\end{cases} \quad (5.20)$$

Therefore, we find, in the continuous limit that the master-equation (5.12) can be approximated by the Fokker-Planck equation

$$\frac{\partial p}{\partial t} = \frac{1}{k_{\mathrm{B}}T\tau_e}\sum_{ij}\frac{\partial}{\partial N_i}A_{ij}\left[\left(\frac{\partial F}{\partial N_j}\right)_{T,\{\boldsymbol{Q}_i\}}p + k_{\mathrm{B}}T\frac{\partial p}{\partial N_j}\right], \quad (5.21)$$

which has an equivalent stochastic differential equation given by Eq. (5.51). In this form, the presence of the Brownian forces and the nature of the drift terms are made clear as differences in chemical potentials $\{\mu_j\}$ between the strands, since

$$\mu_j := \left(\frac{\partial F}{\partial N_j}\right)_{T,\{\boldsymbol{Q}_i\}}. \tag{5.22}$$

Hence, the evolution equation for the continuous model can be written

$$\begin{aligned}
\frac{\partial p(\Omega;t)}{\partial t} &= -\sum_{i=i_\mathrm{b}+1}^{i_\mathrm{f}-1} \frac{\partial}{\partial \boldsymbol{Q}_i}\cdot[\boldsymbol{\kappa}\cdot\boldsymbol{Q}_i]\,p(\Omega) \\
&\quad + \frac{\partial}{\partial \boldsymbol{Q}_{i_\mathrm{b}}}\cdot\left\{\frac{a_\mathrm{K}^2}{k_\mathrm{B}T\tau_e}\left[\left(\frac{\partial F_\mathrm{E}(\boldsymbol{Q}_{i_\mathrm{b}},N_{i_\mathrm{b}})}{\partial \boldsymbol{Q}_{i_\mathrm{b}}}\right)p(\Omega) + k_\mathrm{B}T\frac{\partial p(\Omega)}{\partial \boldsymbol{Q}_{i_\mathrm{b}}}\right]\right\} \\
&\quad + \frac{\partial}{\partial \boldsymbol{Q}_{i_\mathrm{f}}}\cdot\left\{\frac{a_\mathrm{K}^2}{k_\mathrm{B}T\tau_e}\left[\left(\frac{\partial F_\mathrm{E}(\boldsymbol{Q}_{i_\mathrm{f}},N_{i_\mathrm{f}})}{\partial \boldsymbol{Q}_{i_\mathrm{f}}}\right)p(\Omega) + k_\mathrm{B}T\frac{\partial p(\Omega)}{\partial \boldsymbol{Q}_{i_\mathrm{f}}}\right]\right\} \\
&\quad + \frac{1}{k_\mathrm{B}T\tau_e}\sum_{ij}\frac{\partial}{\partial N_i}A_{ij}\left[\mu_j p + k_\mathrm{B}T\frac{\partial p}{\partial N_j}\right] \\
&\quad + \frac{1}{\tau_e}\int\left[W(\Omega|\Omega')p(\Omega') - W(\Omega'|\Omega)p(\Omega)\right]d\Omega',
\end{aligned} \tag{5.23}$$

where the transition probability is now just the sum of the creation and destruction probabilities

$$W(\Omega|\Omega') = W_\mathrm{b}^\mathrm{c}(\Omega|\Omega') + W_\mathrm{f}^\mathrm{c}(\Omega|\Omega') + W_\mathrm{b}^\mathrm{d}(\Omega|\Omega') + W_\mathrm{f}^\mathrm{d}(\Omega|\Omega'). \tag{5.24}$$

In Eq. (5.24), superscript "c" denotes creation and superscript "d" destruction, whereas subscripts "b" and "f" refer to the back and front ends of the chain respectively. These transition probabilities are further described in Section 5.2.4 below.

The stochastic process described by the governing Eq. (5.5) is Markovian. Thus, it can be solved numerically in a straightforward way by simulating an ensemble of identically prepared chains. However, in Sections 5.4 and 5.5, we show a simulation method and results for the model in the limit of a large number of Kuhn steps based on the evolution equation Eq. (5.23). This approximate model may be simulated using standard, higher-order Brownian dynamics algorithms.

5.2.4 Entanglement creation and destruction

The transition probabilities governing creation and destruction of entanglements in Eq. (5.5) are determined merely by differences in free energies according to Eq. (5.11). However, entanglement creation and destruction must be handled differently in the continuous limit. This is accomplished by treating entanglement destruction as a boundary condition in $N_{i_\mathrm{b,f}}$. Namely, if the number of Kuhn steps in the end strand decreases to zero,

we destroy the entanglement (shown here for destruction at the back end of the chain)

$$W_{\rm b}^{\rm d}(\Omega|\Omega') = \delta(N'_{i'_{\rm b}})\delta_{i_{\rm b},i'_{\rm b}+1}\,\delta_{i_{\rm f},i'_{\rm f}}\,\delta(N_{i'_{\rm b}+1}-N'_{i'_{\rm b}}-N'_{i'_{\rm b}+1})\times \delta(\boldsymbol{Q}_{i_{\rm b}}-\boldsymbol{Q}'_{i_{\rm b}})\prod_{i=i_{\rm b}+1}^{i_{\rm f}}\delta(N_i-N'_i)\delta(\boldsymbol{Q}_i-\boldsymbol{Q}'_i). \quad (5.25)$$

In Eq. (5.25) the first delta function provides destruction when there are zero Kuhn steps left in the end strand, the two Kronecker deltas increase the strand index by one at the back end while keeping the index for the front end (decreasing Z by one overall), and the next delta function puts the Kuhn steps of the previous end and last entangled strands into the new end strand. The terms in the second line ensure that the orientation of the new end strand and the $(\boldsymbol{Q}, N)$ configurations of the other strands remain unchanged.

The transition probability for entanglement creation at the chain back end $W_{\rm b}^{c}$ is determined by detailed balance

$$\begin{aligned} W_{\rm b}^{\rm c}(\Omega|\Omega') &= W_{\rm b}^{\rm d}(\Omega'|\Omega)p^{\rm eq}(\Omega)\,/\,p^{\rm eq}(\Omega') \\ &= \delta(N_{i_{\rm b}}-1)\delta_{i_{\rm b},i'_{\rm b}-1}\,\delta_{i_{\rm f},i'_{\rm f}}\,\delta(N_{i_{\rm b}+1}+N_{i_{\rm b}}-N'_{i_{\rm b}+1})\times \\ &\quad \delta(\boldsymbol{Q}_{i_{\rm b}+1}-\boldsymbol{Q}'_{i_{\rm b}+1})\prod_{i=i_{\rm b}+2}^{i_{\rm f}}\delta(N_i-N'_i)\delta(\boldsymbol{Q}_i-\boldsymbol{Q}'_i)\times \\ &\quad w_{\rm b}^{\rm c}(\boldsymbol{Q}'_{i_{\rm b}+1},N'_{i_{\rm b}+1}), \end{aligned} \quad (5.26)$$

where the terms in the two middle lines are analogous to the terms in Eq. (5.25) explained above, and in which $w_{\rm b}^{\rm c}(\boldsymbol{Q}, N)$ is the probability that a dangling end with N Kuhn steps and conformation $\boldsymbol{Q}$ becomes entangled. Similar expressions exist for entanglement creation and destruction at the front end of the chain.

To simplify the notation, we suppress in the following all orientation arguments, $\boldsymbol{Q}$. The creation probability $w_{\rm b}^{\rm c}$ may be found from detailed balance

$$w_{\rm b}^{\rm c}\exp\left[-\frac{F_{\rm E}(N)}{k_{\rm B}T}\right] = w_{\rm b}^{\rm d}\exp\left[-\frac{F_{\rm S}(N-1)+F_{\rm E}(1)}{k_{\rm B}T}\right], \quad (5.27)$$

where $w_{\rm b}^{\rm d}(\boldsymbol{Q}, N)$ denotes the probability that the last entanglement is destroyed turning the last entangled strand with orientation $\boldsymbol{Q}$ and N Kuhn steps into a dangling end. The destruction probability can be determined by extrapolation to zero Kuhn steps for the dangling end in Eq. (5.11)

$$w_{\rm b}^{\rm d} = \exp\left[\frac{F_{\rm S}(N-1)-F_{\rm S}(N)+F_{\rm E}(1)-F_{\rm E}(0)}{2k_{\rm B}T}\right], \quad (5.28)$$

which upon insertion in Eq. (5.27) yields

$$w_{\rm b}^{\rm c} = \exp\left[\frac{-\left[F_{\rm S}(N-1)+F_{\rm S}(N)+F_{\rm E}(0)+F_{\rm E}(1)-2F_{\rm E}(N)\right]}{2k_{\rm B}T}\right]. \quad (5.29)$$

Introducing the Taylor expansions

$$\begin{aligned} F_{\mathrm{S}}(N-1)+F_{\mathrm{S}}(N) &\approx 2F_{\mathrm{S}}(N-1/2)+\frac{1}{4}\frac{\partial}{\partial N}\mu_{\mathrm{S}}(N-1/2)+\ldots \\ F_{\mathrm{E}}(0)+F_{\mathrm{E}}(1) &\approx 2F_{\mathrm{E}}(1/2)+\frac{1}{4}\frac{\partial}{\partial N}\mu_{\mathrm{E}}(1/2)+\ldots \end{aligned} \tag{5.30}$$

to first order in Eq. (5.29), we arrive at

$$w_{\mathrm{b}}^{\mathrm{c}} \approx \exp\left[-\frac{F_{\mathrm{S}}(N-1/2)}{k_{\mathrm{B}}T}-\frac{F_{\mathrm{E}}(1/2)}{k_{\mathrm{B}}T}+\frac{F_{\mathrm{E}}(N)}{k_{\mathrm{B}}T}\right], \tag{5.31}$$

which is valid for any choice of the free energies F_{S} and F_{E}. Recalling the relationships $p_{\mathrm{S}} \sim \exp\left[-F_{\mathrm{S}}/k_{\mathrm{B}}T\right]$ and $p_{\mathrm{E}} \sim \exp\left[-F_{\mathrm{E}}/k_{\mathrm{B}}T\right]$ between the probability densities and free energies for entangled and end strands respectively (see Section 5.2.1), it is easily seen that the expression for $w_{\mathrm{b}}^{\mathrm{c}}$ above provides the correct distribution for newly created entangled strands, since from Eq. (5.31) it follows that

$$w_{\mathrm{b}}^{\mathrm{c}}(\boldsymbol{Q},N) \sim \frac{p_{\mathrm{S}}(\boldsymbol{Q},N)}{p_{\mathrm{E}}(\boldsymbol{Q},N)}, \tag{5.32}$$

assuming $N \gg 1/2$, which is almost always the case for a dangling end about to become entangled.

A specific relationship between the distribution of Kuhn steps in the dangling end and the number in the entangled strands has been suggested by Öttinger (2000), who argued that the end strand distribution at equilibrium should be the distribution created by entanglements at the end. Such an argument leads to the relation

$$p_{\mathrm{E}}(\boldsymbol{Q},N) \sim 1-\mathbb{P}_{\mathrm{S}}(\boldsymbol{Q},N), \tag{5.33}$$

where $\mathbb{P}_{\mathrm{S}}(\boldsymbol{Q},N)$ is the cumulative of $p_{\mathrm{S}}(\boldsymbol{Q},N)$. Employing this relationship, which we shall do later (see Section 5.3), Eq. (5.32) yields

$$w_{\mathrm{b}}^{\mathrm{c}}(\boldsymbol{Q},N) \sim \frac{\mu_{\mathrm{E}}(\boldsymbol{Q},N)}{k_{\mathrm{B}}T}. \tag{5.34}$$

5.2.5 Stress tensor

The polymer contribution to the stress tensor is assumed to be that for rubber elasticity

$$\boldsymbol{\tau}^{\mathrm{p}} = -n\sum_{j=i_{\mathrm{b}}+1}^{i_{\mathrm{f}}-1}\sum_{\boldsymbol{N}}\int\int\int \boldsymbol{Q}_j\left(\frac{\partial F}{\partial \boldsymbol{Q}_j}\right)_{T,\{N_i\}} p(\{\boldsymbol{Q}_i,N_i\}_{i_{\mathrm{b}}}^{i_{\mathrm{f}}};t)d\boldsymbol{Q}_j, \tag{5.35}$$

where n is the number density of polymer chains. Thus, for a given expression of the free energy, stress predictions of the model are completely specified. In Eq. (5.35) it is noted that the unentangled end strands of a chain do *not* contribute to the stress.

5.3 Free Energy of a Chain

With the derivation in Section 5.2.2 of the evolution equation Eq. (5.5) (or for the continuous limit Eq. (5.23) found in Section 5.2.3, combined with the entanglement creation and destruction probabilities discussed in Section 5.2.4), the dynamical framework of the model is now complete. Since a relation between chain configurations and the macroscopic stress has also been derived in Section 5.2.5, the only task remaining, in order to complete the model formulation, is to specify the free energies, $F_{\mathrm{S}}(\boldsymbol{Q}, N)$ and $F_{\mathrm{E}}(\boldsymbol{Q}, N)$.

We determine the free energy of the chain by specifying the equilibrium probability density. This distribution may be constructed from separate distributions for the entangled strands, p_{S}, and the dangling ends, p_{E},

$$p^{\mathrm{eq}}(\Omega) = \delta(N_{\mathrm{K}} - \sum_{i=i_{\mathrm{b}}}^{i_{\mathrm{f}}} N_i) p_{\mathrm{E}}(\boldsymbol{Q}_{i_{\mathrm{b}}}, N_{i_{\mathrm{b}}}) p_{\mathrm{E}}(\boldsymbol{Q}_{i_{\mathrm{f}}}, N_{i_{\mathrm{f}}}) \prod_{i=i_{\mathrm{b}}+1}^{i_{\mathrm{f}}-1} p_{\mathrm{S}}(\boldsymbol{Q}_i, N_i), \quad (5.36)$$

where N_{K} is the total number of Kuhn steps in the chain.

First, we consider the distribution for an entangled strand which is simplest to construct as the product of two densities: a conditional density, $p_{\mathrm{Q}}(\boldsymbol{Q}|N)$, providing the distribution of the strand orientation $\boldsymbol{Q}$ for a given number of Kuhn steps, and a distribution for the Kuhn steps, $p_{\mathrm{N}}(N)$,

$$p_{\mathrm{S}}(\boldsymbol{Q}, N) = J^{-1} p_{\mathrm{Q}}(\boldsymbol{Q}|N) p_{\mathrm{N}}(N), \quad (5.37)$$

where J is a normalization constant. For flows that are not sufficiently strong to violate the stress-optic rule (*e.g.,* all shear flows except for very high shear rate deformations), it should be sufficient to assume that the chain strands are Gaussian and entropic (derived from a coarse-grained random walk), in which case we may write the orientation distribution for a strand as (for example, see Treloar (1958))

$$p_{\mathrm{Q}}(\boldsymbol{Q}|N) = \exp\left[-\frac{3Q^2}{2Na_{\mathrm{K}}^2}\right]. \quad (5.38)$$

On the other hand, strongly aligning and stretching flows (*e.g.,* simple elongation) may require a free energy that does not permit the number of Kuhn steps in a strand to decrease below the physically meaningful limit $|\boldsymbol{Q}|/Na_{\mathrm{K}}$. Such an expression is given shortly (see Section 5.3.1).

The distribution of Kuhn steps in the entangled strands must be equal, and evenly distributed for long chains, which is ensured by making the distribution $p_{\mathrm{N}}(N)$ binomial with moments

$$\langle N \rangle = N_e := N_{\mathrm{K}}/Z_{\mathrm{eq}}\,, \quad \langle N^2 \rangle - \langle N \rangle^2 = N_e \left(1 - \frac{1}{Z_{\mathrm{eq}}}\right). \quad (5.39)$$

Forcing the average number of Kuhn steps to be N_e in the free energy is similar to the tube concept in reptation.

When N_{K} is large, we may well approximate the binomial distribution by a Poissonian

$$p_{\mathrm{N}}(N) \approx \frac{N_e^N \exp(-N_e)}{N!}. \tag{5.40}$$

Because the Poisson distribution is for a semi-infinite domain in N, the normalization factor here is incorrect. However, the errors are less than one part in 10^9 for a typical value of $N_{\mathrm{K}} \approx 1000$.

To obtain the distribution for the end strand, we now make use of Eq. (5.33), which gives

$$p_{\mathrm{E}}(\boldsymbol{Q}, N) = J_{\mathrm{E}}^{-1} \left[1 - \sum_{M=1}^{N} \exp\left(-\frac{3Q^2}{2Ma_{\mathrm{K}}^2} \right) \frac{N_e^M}{M!} \exp(-N_e) \right], \tag{5.41}$$

where J_{E} is a normalization factor. We have used the Poisson distribution Eq. (5.40) for the entangled strands to obtain Eq. (5.41). Putting together the results Eqs. (5.36)–(5.41), and taking the negative logarithm of each side of Eq. (5.36) yields the strand and end free energies

$$\frac{F_{\mathrm{S}}(\boldsymbol{Q}, N)}{k_{\mathrm{B}}T} = \frac{3Q^2}{2Na_{\mathrm{K}}^2} + \log(N!) - (N-1)\log(N_e) - \frac{3}{2} \tag{5.42}$$

$$\frac{F_{\mathrm{E}}(\boldsymbol{Q}, N)}{k_{\mathrm{B}}T} = -\log \left[\frac{1 - \sum_{M=1}^{N} \exp\left(-\frac{3Q^2}{2Ma_{\mathrm{K}}^2} \right) \frac{N_e^M}{M!} \exp(-N_e)}{1 - N_e \exp\left(-N_e - \frac{3}{2} \right)} \right] \tag{5.43}$$

The constants at the end of Eq. (5.42) and in the denominator of Eq. (5.43) are to guarantee that the entropies are zero when a strand has only one available conformation: $F_{\mathrm{S}}(Q = a_{\mathrm{K}}, N = 1) = F_{\mathrm{E}}(Q = a_{\mathrm{K}}, N = 1) = 0$.

5.3.1 Finite extensibility

If we wish to include "minimum monomer density" (similar to finite extensibility), the obvious choice for the orientation distribution would be the Langevin distribution (Treloar, 1958). However, this distribution is not analytic, and therefore difficult to work with. Instead, we may use Cohen's Padé approximation to the inverse Langevin distribution (Cohen, 1991). In this case Eq. (5.38) is replaced by

$$p_{\mathrm{Q}}(\boldsymbol{Q}|N) = \left[1 - \left(\frac{Q}{Na_{\mathrm{K}}} \right)^2 \right]^N \exp\left[-\frac{Q^2}{2Na_{\mathrm{K}}^2} \right], \tag{5.44}$$

and the free energy expressions become

$$\begin{aligned}\frac{F_{\rm S}(\boldsymbol{Q},N)}{k_{\rm B}T} &= N\left[\frac{Q^2}{2N^2a_{\rm K}^2}-\log\left(1-\frac{Q^2}{N^2a_{\rm K}^2}\right)\right]\\ &\quad+\log(N!)-(N-1)\log\left(N_e\right)-\frac{3}{2} \qquad (5.45)\\ \frac{F_{\rm E}(\boldsymbol{Q},N)}{k_{\rm B}T} &= -\log\left[\frac{1-\sum_{M=1}^{N}\left[1-\left(\frac{Q}{Ma_{\rm K}}\right)^2\right]^M\exp\left(-\frac{Q^2}{2Ma_{\rm K}^2}-N_e\right)\frac{N_e^M}{M!}}{1-N_e\exp\left(-N_e-\frac{3}{2}\right)}\right].\end{aligned}$$

5.3.2 Free energy in the continuous limit

For the continuous model, expressions for the free energy must be modified. The orientation distribution for an entangled (Gaussian) strand is still given by the Gaussian in Eq. (5.38), while in the continuous limit, the binomial distribution, $p_{\rm N}(N)$, also becomes a Gaussian with the same moments as in Eq. (5.39). It was found necessary, however, to slightly modify the moments of $p_{\rm N}(N)$ in order to make the entangled strand distribution $p_{\rm S}(\boldsymbol{Q},N)$ yield the desired moments

$$\langle N\rangle = N_e\,,\quad \langle N^2\rangle-\langle N\rangle^2\sim N_e\,,\quad \langle Q^2\rangle_N = N_e, \qquad (5.46)$$

where $\langle Q^2\rangle_N$ denotes the second moment of $\boldsymbol{Q}$ for a given N. Hence, the free energy for an entangled strand becomes

$$\frac{F_{\rm S}(\boldsymbol{Q},N)}{k_{\rm B}T} = \frac{3}{2}\left(\frac{Q^2}{Na_{\rm K}^2}-1\right)+\frac{\left(N-N_e+\frac{3}{2}\right)^2-\left(\frac{5}{2}-N_e\right)^2}{2\left(N_e+\frac{3}{2}\right)\left(1+\frac{1}{Z_{\rm eq}}\right)}. \qquad (5.47)$$

This leads to a chemical potential in the entangled strand of

$$\frac{\mu_{\rm S}(\boldsymbol{Q},N)}{k_{\rm B}T} = -\frac{3Q^2}{2N^2a_{\rm K}^2}+\frac{N-N_e+\frac{3}{2}}{\left(N_e+\frac{3}{2}\right)\left(1+\frac{1}{Z_{\rm eq}}\right)}. \qquad (5.48)$$

Similarly, an end strand still has an equilibrium distribution given by one minus the cumulative probability of an entangled strand, as suggested in Eq. (5.33). Thus, the dangling end has free energy

$$\begin{aligned}\frac{F_{\rm E}(\boldsymbol{Q},N)}{k_{\rm B}T} &= -\log\left\{\int_{N'=N}^{N_{\rm K}}\exp\left(\frac{-3Q^2}{2N'a_{\rm K}^2}\right)\exp\left[\frac{-\left(N'-N_e+\frac{3}{2}\right)^2}{2\left(N_e+\frac{3}{2}\right)\left(1-\frac{1}{Z_{\rm eq}}\right)}\right]dN'\right\}\\ &\quad+\log\left\{\int_{N'=1}^{N_{\rm K}}\exp\left(\frac{-3}{2N'}\right)\exp\left[\frac{-\left(N'-N_e+\frac{3}{2}\right)^2}{2\left(N_e+\frac{3}{2}\right)\left(1-\frac{1}{Z_{\rm eq}}\right)}\right]dN'\right\}, \qquad (5.49)\end{aligned}$$

which results in a chemical potential for the end strand of

$$\frac{\mu_{\mathrm{E}}(\boldsymbol{Q},N)}{k_{\mathrm{B}}T} = \frac{\exp\left(\frac{-3Q^2}{2Na_{\mathrm{K}}^2}\right)\exp\left[\frac{-\left(N-N_e+\frac{3}{2}\right)^2}{2\left(N_e+\frac{3}{2}\right)\left(1-\frac{1}{Z_{\mathrm{eq}}}\right)}\right]}{\int_{N'=N}^{N_{\mathrm{K}}}\exp\left(\frac{-3Q^2}{2N'a_{\mathrm{K}}^2}\right)\exp\left[\frac{-\left(N'-N_e+\frac{3}{2}\right)^2}{2\left(N_e+\frac{3}{2}\right)\left(1-\frac{1}{Z_{\mathrm{eq}}}\right)}\right]dN'}$$
$$\approx \frac{\exp\left[\frac{-\left(N-N_e+\frac{3}{2}\right)^2}{2\left(N_e+\frac{3}{2}\right)\left(1-\frac{1}{Z_{\mathrm{eq}}}\right)}\right]}{\sqrt{\frac{\pi}{2}\left(N_e+\frac{3}{2}\right)\left(1-\frac{1}{Z_{\mathrm{eq}}}\right)}\,\mathrm{erfc}\left[\frac{N-N_e+\frac{3}{2}}{\sqrt{2\left(N_e+\frac{3}{2}\right)\left(1-\frac{1}{Z_{\mathrm{eq}}}\right)}}\right]}. \quad (5.50)$$

A simulation with the full expression in the first line of Eq. (5.50) has confirmed the validity of the approximate expression in the second line for the entire range of $(\boldsymbol{Q},N)$ values exploited by the simulations.

The complete evolution of the continuous model is described by Eqs. (5.23) – (5.26), (5.34), (5.48), and (5.50). In the following section, a simulation algorithm for this model is derived.

5.4 Simulation Algorithm

The dynamics prescribed by Eq. (5.23) is equivalent to $Z+1$ SDEs for the number of Kuhn steps in each strand; two three-dimensional SDEs for the conformations of the dangling ends; $Z-1$ deterministic equations for the affine deformation of the interior strands; a boundary condition for the destruction of entanglements; and a probabilistic jump process for the creation of entanglements. We handle the simulation of each of these processes in turn.

The SDEs equivalent to the Fokker-Planck-like portion of Eq. (5.23), namely Eq. (5.21), for the Kuhn steps are

$$dN_i = \frac{1}{k_{\mathrm{B}}T\tau_e}\left(\mu_{i+1}-2\mu_i+\mu_{i-1}\right)dt + \sqrt{\frac{2}{\tau_e}}\left(dW_{i-1}-dW_i\right), \quad i=i_b,\ldots,i_f. \quad (5.51)$$

We integrate these equations over a small time-step Δt, and approximate the drift terms for the entangled strands semi-implicitly over the time interval

$$N_i(t+\Delta t) = N_i(t) - \frac{\Delta t}{2k_{\mathrm{B}}T\tau_e}\sum_j A_{ij}\left\{\mu_j[\boldsymbol{Q}_j(t+\Delta t),N_j(t+\Delta t)] + \mu_j[\boldsymbol{Q}_j(t),N_j(t)]\right\} + \sqrt{\frac{2}{\tau_e}}\sum_j \bar{\boldsymbol{B}}_{ij}\Delta W_j, \quad i=i_{\mathrm{b}+1},\ldots,i_{\mathrm{f}-1}, \quad (5.52)$$

where $\Delta W_i(t)$ is a Wiener increment with zero mean, and variance Δt. The formulation in Eq. (5.52) guarantees conservation of Kuhn steps, and helps ensure that the algorithm is stable, since the number of Kuhn steps cannot become negative. However, this expression represents $Z-1$ coupled nonlinear algebraic equations in the unknown $\{N_i(t+\Delta t)\}$, which cannot be solved analytically. Hence, we solve these by an iterative technique at every time step. Inserting the chemical potential (Eq. (5.48)) and rearranging Eq. (5.52) yields

$$\begin{aligned} N_i - \frac{3\Delta t}{2N_i^2} Q_i^2(t+\Delta t) \;+\; & \frac{\left(N_i - N_e + \frac{3}{2}\right)\Delta t}{\left(N_e + \frac{3}{2}\right)\left(1 - \frac{1}{Z_{\mathrm{eq}}}\right)} \\ = \; & f_i(t) + \frac{\Delta t}{2}\left[\mu^\circ_{i+1} + \mu^\circ_{i-1}\right], \end{aligned} \tag{5.53}$$

where $N_i \equiv N_i(t+\Delta t)$, μ°_{i+1} is the chemical potential of strand $i+1$ found from the last iteration, and

$$f_i(t) := N_i(t) - \frac{\Delta t}{2k_{\mathrm{B}}T\tau_e}\sum_j A_{ij}\mu_j[N_j(t), \boldsymbol{Q}_j(t)] + \sqrt{\frac{2}{\tau_e}}\sum_j \bar{\boldsymbol{B}}_{ij}\Delta W_j. \tag{5.54}$$

The initial value of μ_i° is that from the beginning of the time step. At each iteration, the above equation is cubic in the unknown N_i, which has a well-known analytic solution.

The above technique is used for the interior strands, whereas the end strands are integrated simply as explicit Euler forward. The algorithm is second order in time-step size for the interior strands, but more importantly, it is stable. It is also found to converge very quickly, for even a small tolerance in the iteration steps.

The SDEs for the conformation of the dangling ends is just like a dumbbell, Eq. (5.4). For a Gaussian free energy, this expression is identical to that for a Hookean dumbbell, which has an analytic solution. However, in our case, the number of Kuhn steps during the time step is fluctuating. Therefore, we combine the analytic expression for the Hookean dumbbell with a semi-implicit approximation for the number of Kuhn steps

$$\begin{aligned} \boldsymbol{Q}_{i_{b,f}}(t+\Delta t) \;=\; & \boldsymbol{Q}_{i_{b,f}}(t)\exp\left[-\frac{6\Delta t}{\tau_e[N_{i_{b,f}}(t) + N_{i_{b,f}}(t+\Delta t)]}\right] + \\ \boldsymbol{\eta}\left[\frac{N_{i_{b,f}}(t+\Delta t)a_{\mathrm{K}}^2}{3}\left\{1 - \exp\left(-\frac{12\Delta t}{\tau_e[N_{i_{b,f}}(t) + N_{i_{b,f}}(t+\Delta t)]}\right)\right\}\right]^{1/2} & \end{aligned} \tag{5.55}$$

where $\boldsymbol{\eta}$ is a three dimensional vector of Gaussian-distributed, independent random numbers. Such an expression is high order in time-step size, and stable.

Affine deformation of the interior strands is expressed by evolution equation (5.3), which has the exact solution

$$\boldsymbol{Q}_i(t+\Delta t) = \boldsymbol{E}(t+\Delta t, t)\cdot\boldsymbol{Q}_i(t), \quad i = i_{\mathrm{b}+1}, \ldots, i_{\mathrm{f}-1}, \tag{5.56}$$

in which $\boldsymbol{E}(t,t')$ is the finite strain tensor (Bird *et al.*, 1987a).

Destruction of the entanglements at the end of the chain is determined by the boundary condition, Eq. (5.25). In other words, whenever the number of Kuhn steps in the dangling end becomes less than or equal to one, the entanglement is destroyed. However, such an algorithm is only order $1/2$ in Δt. The situation may be improved by considering the probability of a hidden absorption in $N_{i_{\mathrm{b,f}}}$. To include this in the simulation algorithm, we adopt an analogous technique recently used by Öttinger (1996), which yields the probability of encountering a hidden reflection, P_{hidden}, as

$$P_{\mathrm{hidden}} = \exp\left[\frac{\left(N_{i_{b,f}}-1\right)\left(1-\tilde{N}_{i_{b,f}}\right)\tau_e}{\Delta t}\right], \tag{5.57}$$

where N_i is the number of Kuhn steps in the end strand at the end of the time step, and $\tilde{N}_i$ is the same quantity but without the contribution from the Brownian forces. If a hidden absorption is observed, the orientation of the end strand is simply renewed according to Eq. (5.38).

Entanglement creation is accomplished by drawing a random number from a uniform distribution $[0,1]$. If this number is less than $w^{\mathrm{c}}(\boldsymbol{Q},N)$ for a dangling strand, an entanglement at the end is imposed, creating a new dangling end with a single Kuhn step.

The above algorithm is performed on an ensemble of chains and averages are taken over this ensemble. Such an algorithm provides a numerical estimate of averages taken over a probability density whose evolution is described by Eq. (5.23). This evolution equation should provide an excellent approximation to the discrete model, Eq. (5.5) when the number of Kuhn steps in the chain is large.

5.5 Linear Viscoelastic Results

Using the simulation algorithm just described, we look into some predictions of the model in the linear viscoelastic regime. However, extracting simulation results for small-amplitude oscillatory shear flow is difficult because of the very large ensemble sizes needed to avoid excessive statistical noise. Instead, we utilize linear response theory (Résibois and Leener, 1977) which allow us to find the relaxation modulus directly from an equilibrium simulation. Namely, $G(t)$ is found from the autocorrelation function of the shear stress at equilibrium

$$G(t) = \frac{1}{nkT}\left\langle \tau_{yx}(0)\tau_{yx}(t)\right\rangle_{\mathrm{eq}}, \tag{5.58}$$

where $\langle\ldots\rangle_{\mathrm{eq}}$ indicates taking an average over a large ensemble of chains at equilibrium. Using this technique, ensemble sizes of $1000-5000$ chains are sufficient to provide the needed signal to noise ratio, which would

otherwise require an ensemble size on the order of 10000 chains if $G(t)$ was to be simulated as the stress relaxation following a small-strain shear step. Comparison with step strain simulations confirms the results using Eq. (5.58) though.

In the model it is necessary to specify two parameters describing the chain chemistry before simulations begin: Z_{eq}, the average number of chain strands at equilibrium; and N_{K}, the total number of Kuhn steps in the chain. The first of these is found from the molecular weight, M_w, and the entanglement molecular weight, M_{e}, while the latter can be estimated from M_w, and static properties of the chain under theta conditions (Rault, 1987; Fetters *et al.*, 1999). First, we use $Z_{\mathrm{eq}} = 7$ and $N_{\mathrm{K}} = 1000$ in the simulations, which correspond to the parameter values for the entangled, nearly monodisperse polystyrene/TCP system with which the previous reptation model has been thoroughly compared in a variety of shearing deformations (Hua *et al.*, 1998, 1999; Neergaard *et al.*, 2000). In particular, comparisons have been made in the linear viscoelastic regime (Chapter 2 of this thesis), and the reader is referred to this part of the thesis and references therein for more details on estimation of parameters, and on the fluid, which has a mean relaxation time of $\tau_{\mathrm{m}} = 15$ s.

In order to determine the phenomenological parameter τ_e for the system considered, we relate it to the reptation time, τ_{d}, by means of Eq. (6.19) of Doi and Edwards (1986)

$$\tau_{\mathrm{d}} = \frac{\zeta N_{\mathrm{K}}^3 a_{\mathrm{K}}^2}{\pi^2 N_e k_{\mathrm{B}} T} = c_1 \frac{N_{\mathrm{K}}^3}{\pi^2 N_e}\, \tau_e, \tag{5.59}$$

in which we have substituted $\zeta = c_1 \frac{k_{\mathrm{B}} T}{a_{\mathrm{K}}^2} \tau_e$, the friction coefficient when the test chain slips through an entanglement, and where c_1 is a numerical coefficient of order unity. It remains to determine c_1 which is obtained by comparing the simulated relaxation modulus with linear viscoelastic experiments. The comparison is made by following the same procedure as outlined for the earlier model (Chapter 2 of this thesis): A discrete relaxation spectrum $\{g_i, \lambda_i\}$ is fit to the simulated $G(t)$, and the zero-shear-rate properties are extracted as $\eta_0 = \sum_i g_i \lambda_i$ and $\Psi_{1,0} = \sum_i g_i \lambda_i^2$ respectively. τ_{d} is then estimated as $\tau_{\mathrm{d}} = \frac{\Psi_{1,0}}{2\eta_0}$, and c_1 is fixed by equating τ_{d} with τ_{m} for the fluid. Using this approach, we obtain $c_1 \approx 0.6906$, which completely specifies the time scales of the model. The simulated relaxation modulus was found to converge using a time step size of $\Delta t = 0.3 N_e \tau_e$ as simulations with smaller time steps showed no discernible differences in $G(t)$.

We notice that the expression in Eq. (5.59) predicts a dependence of τ_{d} on molecular weight (given by the number of Kuhn steps in the chain N_{K}) of M_w^3, whereas a power law exponent of 3.3 – 3.5 for the same scaling relationship is commonly found for experiments on polymer melts (for example see Figure 3.6–4 of Bird *et al.* (1987b)). This discrepancy can be explained by means of contour-length fluctuations (Doi, 1983; Ketzmerick

and Öttinger, 1989), which are not accounted for in the model by Doi and Edwards leading to Eq. (5.59) but are included in the new model considered here. Hence, the scaling relationship for the present model is not exactly that of the Doi-Edwards model, and therefore we may expect some weak dependence on M_w of the numerical coefficient c_1 upon comparison of the model with a series of polymer systems with identical chemistry but varying molecular weight.

Next, we look at how the model predicts the scaling with molecular weight of the zero-shear-rate viscosity, η_0. This is done by repeating the equilibrium simulation described above for several different molecular weights or equivalently different values of Z_{eq} while maintaining the same chain architecture as in the original system considered. That is, we change Z_{eq} and N_{K} simultaneously in such a way that N_e, the number of Kuhn steps equivalent with the entanglement molecular weight, is kept constant, $N_e = \frac{N_{\text{K}}}{Z_{\text{eq}}} \approx 142.86$. Figure 5.2 shows the zero-shear-rate viscosity normalized by the value for $Z_{\text{eq}} = 7$, and plotted as a function of the molecular weight (expressed in terms of the equilibrium number of entanglements). A fit to the simulations, which are performed over an entire decade of Z_{eq} values, reveals a power law exponent of $\alpha_\eta = 3.18 \pm 0.03$, which is slightly lower than the expected value of 3.3 – 3.5.

A closer look at the results in Figure 5.2 is obtained by plotting versus Z_{eq} the quantity η_0/Z_{eq}^3 rather than the viscosity alone. This plot is made in Figure 5.3, where η_0/Z_{eq}^3 has been normalized by its value for $Z_{\text{eq}} = 7$. The figure suggests that the dependence on molecular weight of

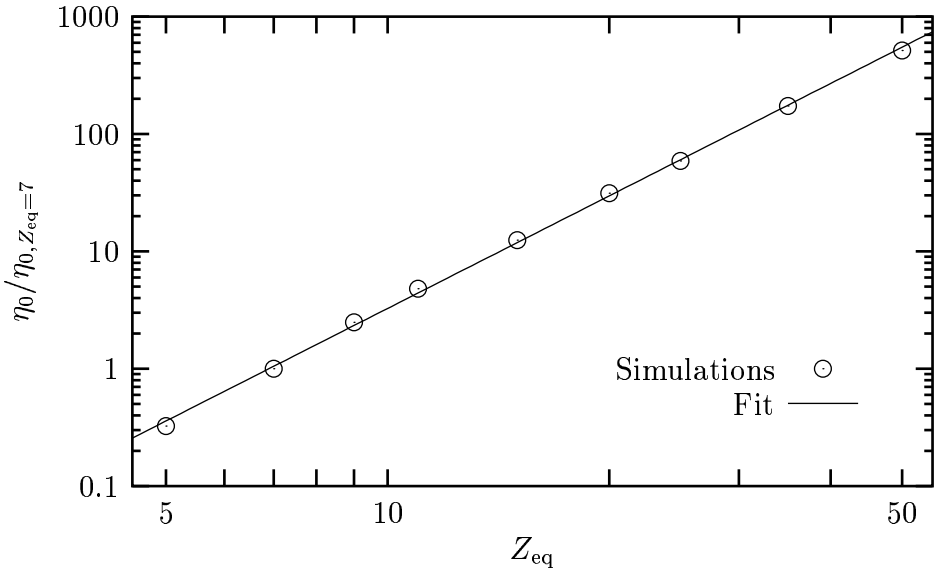

Figure 5.2. Scaling of η_0 with molecular weight (expressed as the equilibrium number of entanglements, Z_{eq}). The viscosity is normalized by its value for $Z_{\text{eq}} = 7$. The power law exponent of the fit is $\alpha_\eta = 3.18 \pm 0.03$.

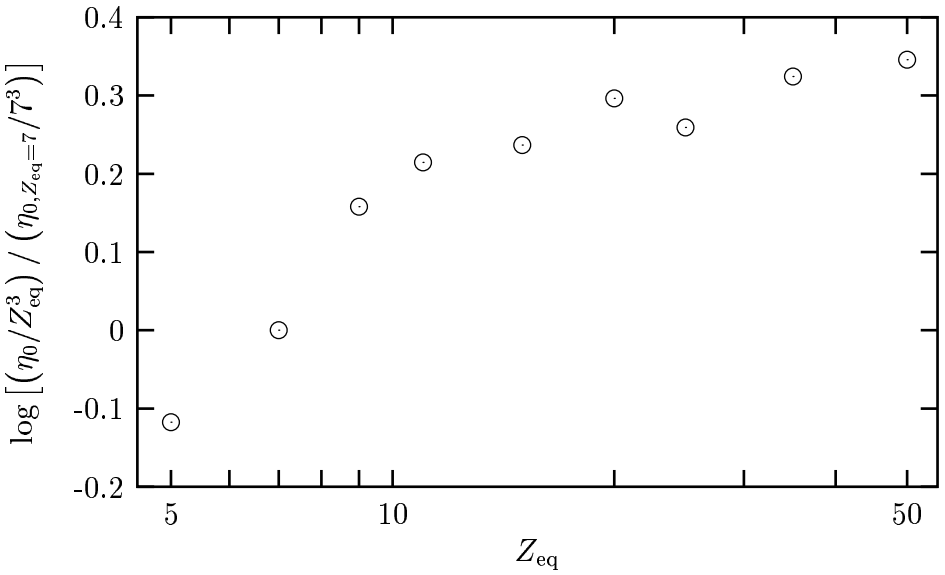

Figure 5.3. Scaling of η_0 with molecular weight (expressed as the equilibrium number of entanglements, Z_{eq}). The viscosity is divided by Z_{eq}^3 in order to emphasize the deviation of the power law exponent from the value of 3. The plotted quantity η_0/Z_{eq}^3 is normalized by the value for $Z_{\mathrm{eq}} = 7$.

the simulated zero-shear-rate viscosity is part of a transition to a power law behavior with a scaling exponent of 3 for large molecular weights (revealed as a zero slope in Figure 5.3). Indeed, linear viscoelastic simulations by Milner and McLeish (1998) confirm that for $\eta_0(M_w)$ such a transition from the experimentally observed power law exponent of 3.3 – 3.5 to an asymptotic value of 3 does occur, which could be expected since the importance of contour-length fluctuations decreases as the chains become longer. However, Milner and McLeish found that the onset of the transition does not occur until the chains become *very* long ($Z_{\mathrm{eq}} > 100$), whereas the present simulations predict the occurrence of the transition at much lower molecular weights, where it has never been observed experimentally. This discrepancy might be due to the fact that the chain architecture in all simulations in Figures 5.2 and 5.3 originates from the polystyrene solution discussed above, which implies a rather large entanglement spacing ($N_e \approx 142.86$). For an undiluted melt N_e is much lower, and the predicted occurrence of the transition to a M_w^3 dependence of the viscosity might be rather different. Also, it should be mentioned that including the concept of constraint release in the model could possibly influence the scaling relationship between η_0 and M_w too.

5.6 Flow simulations

Surprisingly, inception of steady shear simulations with the continuous limit model considered in Sections 5.4 and 5.5 do not yield results anywhere close to those observed experimentally. For both low and high shear rates, the stresses increase upon inception of flow, but they rise to a too high steady state value, and neither the shear stress nor the first normal stress difference exhibit overshoot in the transient.

These observations suggest that only little chain retraction (if any at all) is taking place in the presence of flow. We can show that this is indeed the case using a simple thermodynamic argument, where we consider Eq. (5.47), the free energy expression for an interior strand. The drift terms of the evolution equation (third line of Eq. (5.23)) will tend to drive the interior strands towards the $(\boldsymbol{Q}, N)$ configuration providing the minimum of the free energy, which can be found as $\mu_{\mathrm{S}}(\boldsymbol{Q}, N) = 0$ using Eq. (5.48). During flow $\boldsymbol{Q}$ is affinely deformed by means of Eq. (5.3), and from $\mu_{\mathrm{S}}(\boldsymbol{Q}, N) = 0$ we can therefore calculate the number of Kuhn steps, which will provide the minimum free energy of a strand.

The result of such a calculation, based on Eq. (5.47), is shown in Figure 5.4 (solid line), where we have normalized $\boldsymbol{Q}$ and N by $\sqrt{N_e}a_{\mathrm{K}}$ and N_e respectively. Hence, in absence of flow the equilibrium condition would be in the neighborhood of $(1, 1)$ in the figure, and as $\boldsymbol{Q}$ is increased by affine deformation, we would expect N to rise accordingly (for example as seen in the dashed line in the figure). When looking at Figure 5.4 it

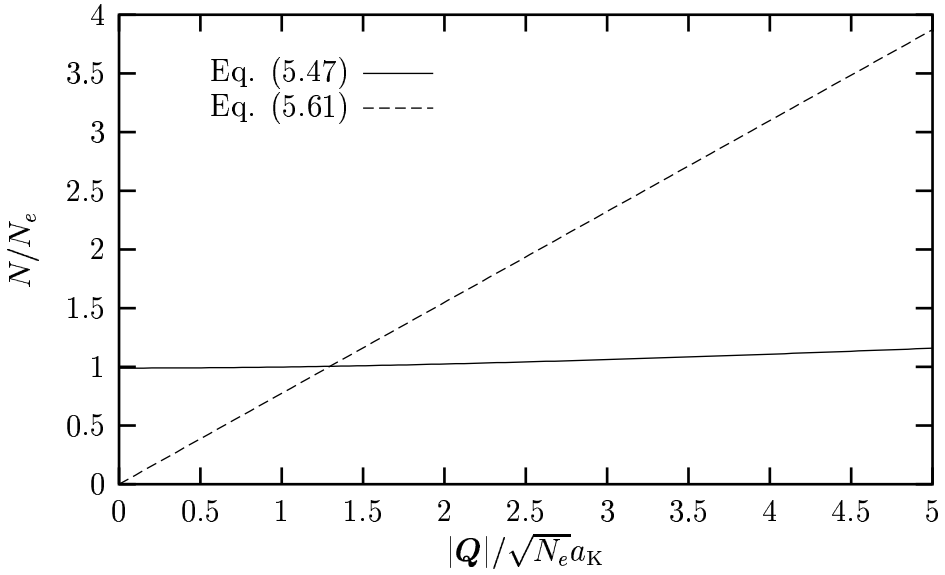

Figure 5.4. The number of Kuhn steps N in an entangled strand, which provides the minimum free energy as a function of the strand length $|\boldsymbol{Q}|$ imposed by affine deformation. Two different free energy expressions are considered in the figure.

should be kept in mind that the depicted equilibrium condition may never be reached due to the dynamic processes continuously taking place. When the free energy is given by Eq. (5.47), the expected increase of N with increasing $\boldsymbol{Q}$ does clearly not occur. If a strand is stretched to four times its equilibrium length, the "equilibrium condition" would still only yield $1.15N_e$ Kuhn steps in the strand, which implies significant stretching.

Therefore, a different free energy expression for the interior strands is required. Fortunately, exchanging the free energy within the model is easily done, since all the model equations in Section 5.2 are valid for any expression of the free energy. A wide variety of free energy expressions are possible, although certain restrictions do apply. The first term of Eq. (5.47) originates from classic network theory assuming the strands to be Gaussian and entropic. Hence, it seems unwise to change this term unless one wants to account for finite extensibility as outlined in Section 5.3.1.

Furthermore, it is noted that anything but a quadratic dependence of the free energy on $\boldsymbol{Q}$ will lead to a complicated stress tensor expression (see Section 5.2.5) and imply a violation of the stress-optic rule. Thus, still specifying the free energy in terms of the distribution $p_{\mathrm{S}}(\boldsymbol{Q}, N)$ as given by Eq. (5.37), we maintain the orientation distribution Eq. (5.38).

This leaves the probability density $p_{\mathrm{N}}(N)$, or equivalently the second term of Eq. (5.47), as the only option for making changes of the free energy expression. We still want to specify the distribution $p_{\mathrm{N}}(N)$, which represents the tube effect in the model, such that $p_{\mathrm{S}}(\boldsymbol{Q}, N)$ satisfies the first and last moment criteria given in Eq. (5.46), whereas the second one of those criteria is probably less important. Even, with these requirements there are many possibilities for $p_{\mathrm{N}}(N)$. We choose one, which leads to a term in the free energy that is linear in N. This implies complete retraction of the chain to its equilibrium length, which is also assumed in the Doi-Edwards model and leads to the correct damping function in step strain deformations. The free energy for an interior strand then reads

$$\frac{F_{\mathrm{S}}(\boldsymbol{Q}, N)}{k_{\mathrm{B}}T} = \frac{3}{2}\left(\frac{Q^2}{Na_{\mathrm{K}}^2} - 1\right) + \frac{5(N-1)}{2N_e} \,, \tag{5.60}$$

which leads to a chemical potential in the entangled strand of

$$\frac{\mu_{\mathrm{S}}(\boldsymbol{Q}, N)}{k_{\mathrm{B}}T} = -\frac{3Q^2}{2N^2a_{\mathrm{K}}^2} + \frac{5}{2N_e} \,, \tag{5.61}$$

and yields the dashed line in Figure 5.4, confirming that chain retraction will take place with this expression for $F_{\mathrm{S}}(\boldsymbol{Q}, N)$.

Before doing simulations with the modified free energy expression, we introduce another change in the model that concerns destruction and creation of entanglements. That is, instead of determining creation of new entanglements by a creation probability, we treat creation as a simple boundary condition, creating a new entanglement when the number of Kuhn steps in the end strand exceeds N_e. The new entangled strand

is given a random orientation vector of length $\sqrt{N_e}$ and gets exactly N_e Kuhn steps, while the remaining Kuhn steps go into the new end strand. This boundary condition for entanglement creation closely resembles that of the full-chain reptation model.

The boundary condition for destruction is the same as before, such that the entanglement is destroyed when the chain slips out of it (when the number of Kuhn steps reaches zero). However, we abandon the relationship between the free energies in the entangled and end strands (Eq. (5.33)), and specify the free energy of an end strand to be

$$\frac{F_{\mathrm{S}}(\boldsymbol{Q}, N)}{k_{\mathrm{B}}T} = \frac{5(N-1)}{2N_e} \,, \tag{5.62}$$

which is merely the tube part of the entangled strand free energy.

Equilibrium simulations with the modified model confirm that yet another simplifying change of the model can be made, while still satisfying the fundamental equilibrium distribution Eq. (5.1). With this change we switch off the dynamics of the end strands, implying that the ends become dangling and are able to explore all available orientations. Since the ends no longer have any specific orientation, the number of dynamic variables for a chain is reduced, and the evolution equation for the continuous limit simplifies to

$$\begin{aligned} \frac{\partial p(\Omega;t)}{\partial t} \;=\; & -\sum_{i=i_{\mathrm{b}}+1}^{i_{\mathrm{f}}-1} \frac{\partial}{\partial \boldsymbol{Q}_i} \cdot [\boldsymbol{\kappa} \cdot \boldsymbol{Q}_i]\, p(\Omega) \\ & + \frac{1}{k_{\mathrm{B}}T\tau_e} \sum_{ij} \frac{\partial}{\partial N_i} A_{ij} \left[\mu_j p + k_{\mathrm{B}}T \frac{\partial p}{\partial N_j} \right] \\ & + \frac{1}{\tau_e} \int \left[W(\Omega|\Omega')p(\Omega') - W(\Omega'|\Omega)p(\Omega) \right] d\Omega' . \end{aligned} \tag{5.63}$$

Note, that with the latest modifications, it is now possible to eliminate N_e from the equation set by means of suitable dimensionless variables. However, we choose to keep the dimensional equations in this work.

In the shear simulations that are to follow, we use $Z_{\mathrm{eq}} = 7$ and $N_{\mathrm{K}} = 1000$, the same parameter set as used in the study of linear viscoelasticity with the unmodified model (see Section 5.5). The same parameter values were also used for shear simulations with the full-chain reptation model (Hua *et al.*, 1999), with which we want to compare the predictions of the new model in addition to experiments. The ensemble size is in all cases 10000 chains, and all simulations are found to converge for a time step size of $\Delta t = 0.15 N_e \tau_e$.

An equilibrium simulation is made to fix the lone adjustable parameter as outlined in Section 5.5. This gives $c_1 \approx 0.239$, which is somewhat lower than the value found for the unmodified model ($c_1 \approx 0.6906$). Using $c_1 = 0.239$, simulations of transient shear flow show that the zero-shear

viscosity η_0, as predicted by the equilibrium simulation, provides the expected upper bound for all steady state shear viscosities $\eta(\dot{\gamma})$. However, some of the results for the steady state first normal stress differences $\Psi_1(\dot{\gamma})$ in flow exceed significantly the value of $\Psi_{1,0}$ extracted from the equilibrium simulation, which is inconsistent. This suggests that the equilibrium simulation estimate of $\Psi_{1,0}$ and consequently also the value of $c_1 = 0.239$ are incorrect.

To circumvent the inconsistency we use instead the steady state predictions of a shear flow simulation with a very low shear rate ($De = 0.07$) to obtain better estimates of η_0, $\Psi_{1,0}$ and the adjustable parameter c_1. This gives $c_1 \approx 0.18525$ which is used in all shear flow simulations considered below.

Figure 5.5 shows η^+, the shear viscosity, as a function of time during inception of steady shear for several shear rates (expressed by the Deborah number for the flow, $De := \dot{\gamma}\tau_d$). The curves, which are normalized by η_0, appear very similar to the corresponding curves for the full-chain reptation model (see Figure 2 of Hua *et al.* (1999)), although they seem to be more underdamped. The same trend is seen in Figure 5.6, where we repeat the plots in Figure 5.5, but for Ψ_1^+, the first normal stress difference. It is seen that the onset of overshoot for the normal stress occurs at a higher shear rate than for the viscosity in agreement with experiments.

In Figures 5.7 and 5.8 we again plot the viscosity and first normal stress difference respectively versus time for start up of steady shear at three different shear rates. The plots are normalized by the steady state values in order to focus on the magnitude of the overshoots in the transient phase.

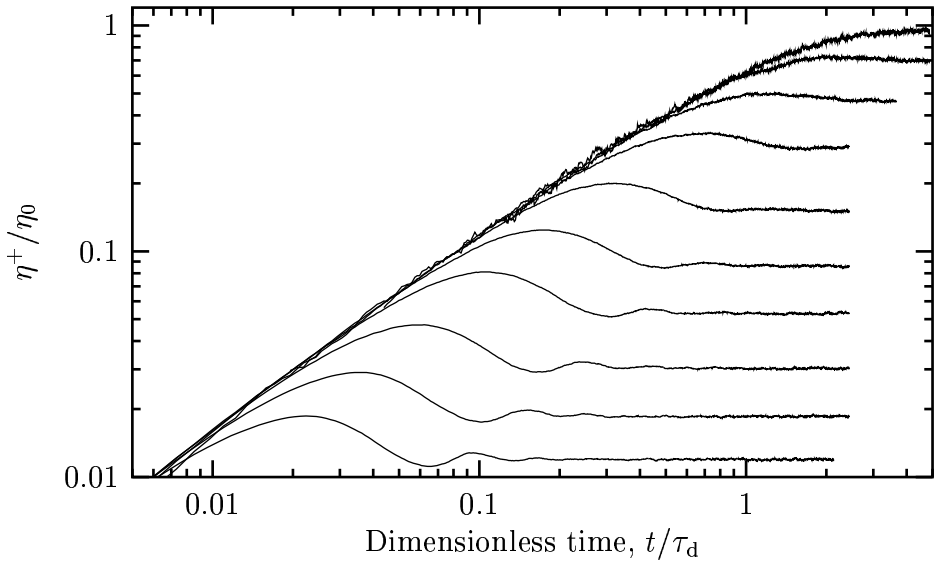

Figure 5.5. Transient viscosities as functions of dimensionless time under start up of steady shear flow for several shear rates. The Deborah numbers used are $De = \dot{\gamma}\tau_d = 0.3, 0.7, 1.5, 3, 7, 15, 30, 70, 150, 300$.

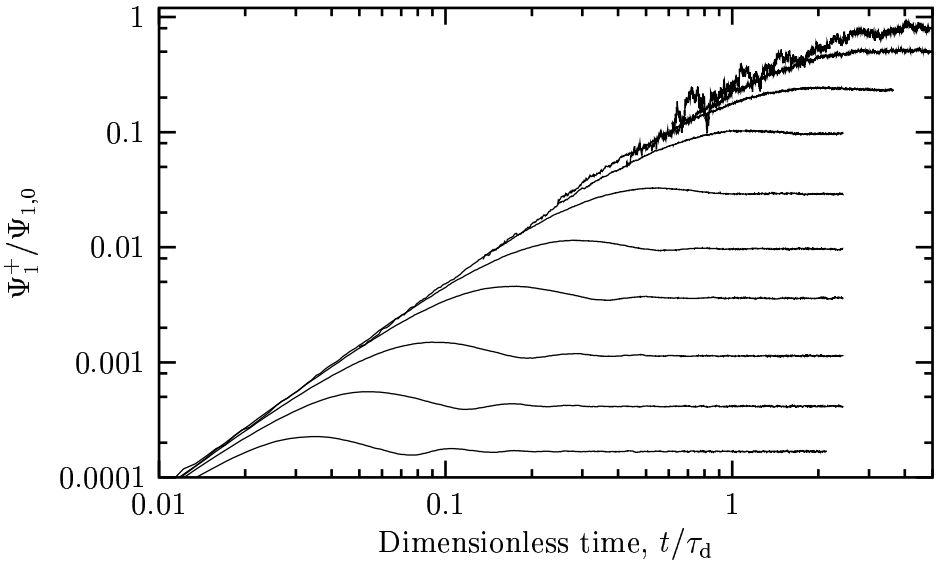

Figure 5.6. Transient normal first differences as functions of dimensionless time under start up of steady shear flow for several values of the Deborah number. ($De = \dot{\gamma}\tau_d = 0.3, 0.7, 1.5, 3, 7, 15, 30, 70, 150, 300$).

The predictions of the new model (solid lines) are denoted "sliplink model" in the figures, which also contain the experimental results (symbols) and the predictions of the full-chain reptation model (shown as dashed lines and denoted "tube model") for comparison.

It is seen that at low shear rates, where no overshoots occur, the results of the two models are almost identical and describe the experimental

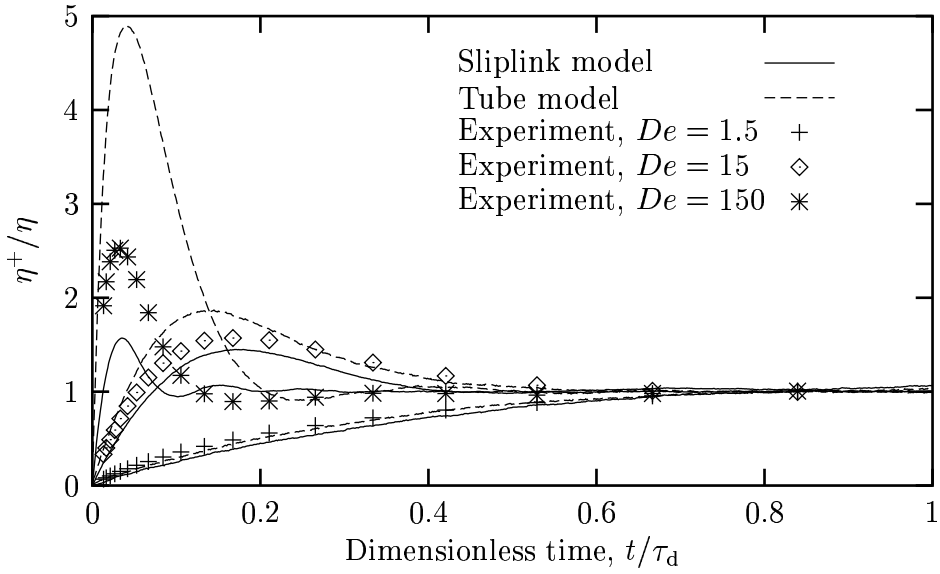

Figure 5.7. Transient viscosities normalized by their steady state values as functions of dimensionless time under start up of steady shear.

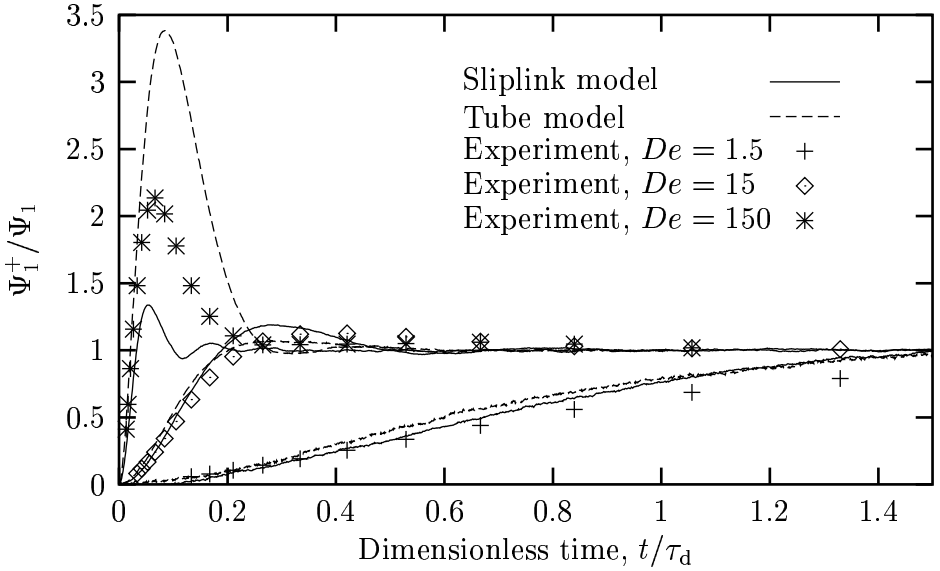

Figure 5.8. Transient normal first differences normalized by their steady state values as functions of dimensionless time under start up of steady shear.

data very well, whereas at higher shear rates we recall that the full-chain reptation model overpredicts the magnitude of the stress overshoots. On the contrary, it is evident that the new model predicts overshoots of too small a magnitude, and that it predicts a too underdamped evolution of the stresses at high shear rates.

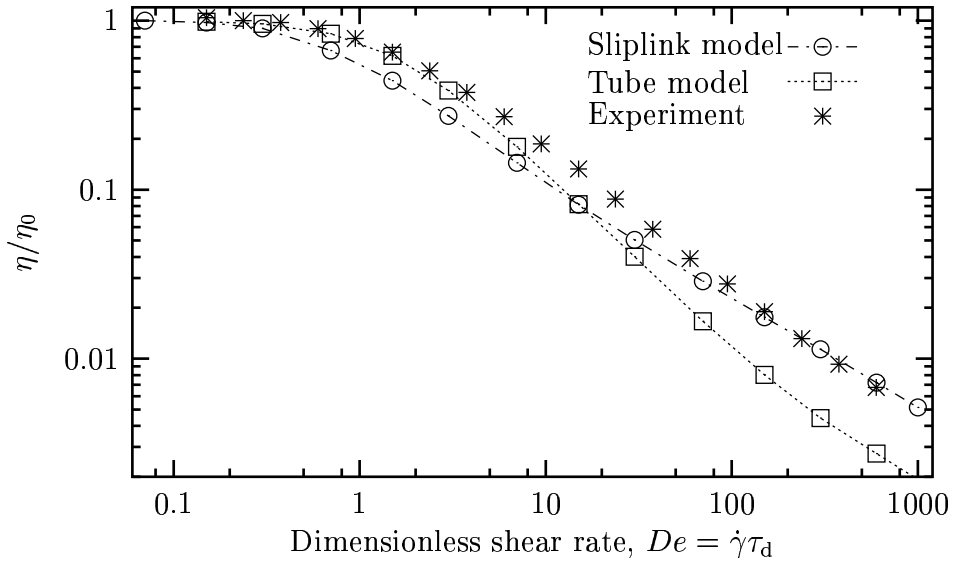

Figure 5.9. Steady state viscosity normalized by the zero-shear viscosity as function of dimensionless shear rate. A fit to the power law region predicted by the sliplink model yields an exponent of -0.683 ± 0.008.

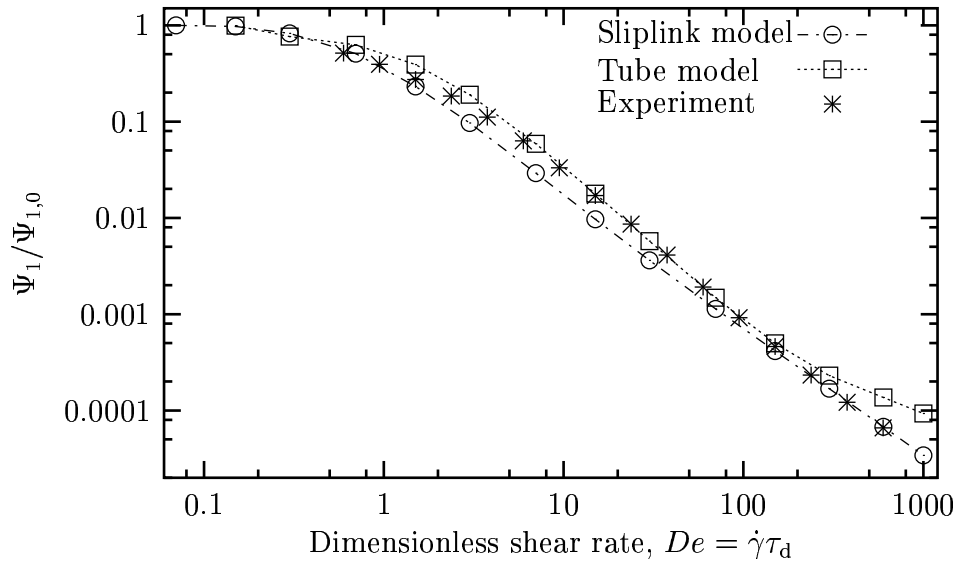

Figure 5.10. Steady state normal first differences, as functions of dimensionless shear rate. A fit to the power law region predicted by the sliplink model yields an exponent of -1.365 ± 0.008.

The steady state viscosity is shown as a function of shear rate in Figure 5.9. A fit of the power law behavior as predicted by the new model yields a power law exponent of -0.683 ± 0.008, which is surprising, yet encouraging, since it implies a monotonic dependence of shear stress on shear rate. In the theory of reptation it is generally believed that the mechanism of convective constraint release (CCR) is necessary to obtain a monotonic shear rate dependence of the shear stress, but CCR has not been incorporated in the new model in its present form. A comparison with the experimental data shows that the full-chain reptation model predicts too steep a slope of the power law region, whereas the new model predicts a power law region with a slope that appears to be too weak.

The analogous plot for the first normal stress difference is seen in Figure 5.10. Here, the power law regime of the curve resulting from the new model gives a power law exponent of -1.365 ± 0.008, and it appears that both models describe the experimental data very well.

We move on to consider the transient extinction angle during start up of steady shear. Figure 5.11 depicts χ, the extinction angle for inception of steady shear at two different shear rates. It is seen that the χ curves exhibit an undershoot except at low shear rates (not shown), which is consistent with experimental observations. However, at high shear rates it appears that the undershoot is too abrupt and that χ approaches its steady state value in a too underdamped fashion, like it was observed for the transient stress curves in Figures 5.5 – 5.8. It is noted that the tube model exhibits an undershoot only at the highest shear rate.

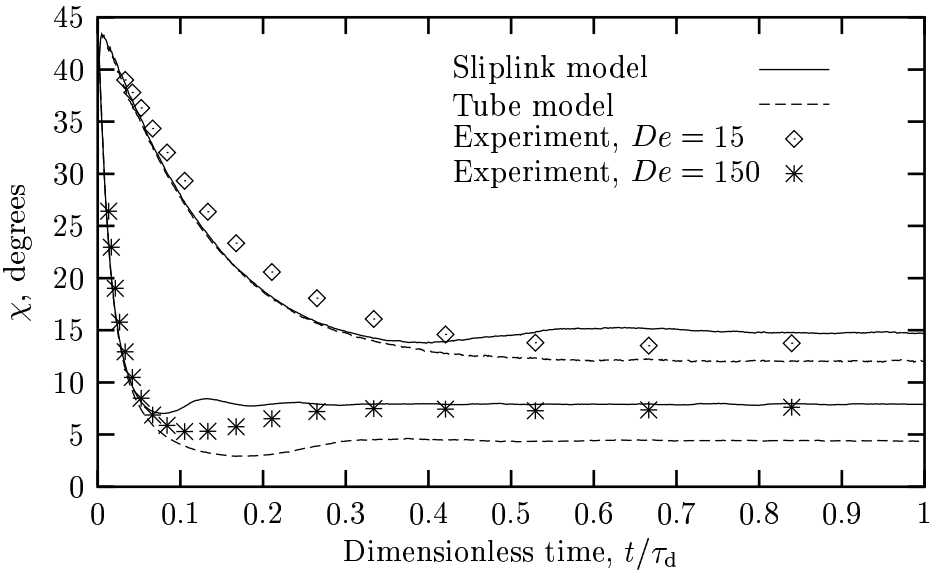

Figure 5.11. Transient extinction angle as function of dimensionless time under start up of steady shear for a moderate and a high shear rate.

Finally, in Figure 5.12 we plot the steady state extinction angle as a function of shear rate. With a steady state extinction angle of 4.26° for a very high shear rate of $De = 1000$, it is evident that the model predicts a non-zero value of χ at steady state for all experimentally accessible shear rates and provides a good description of the experimental data. This is an improvement over the full-chain reptation model, which predicts the steady state value of χ to approach zero for high shear rates.

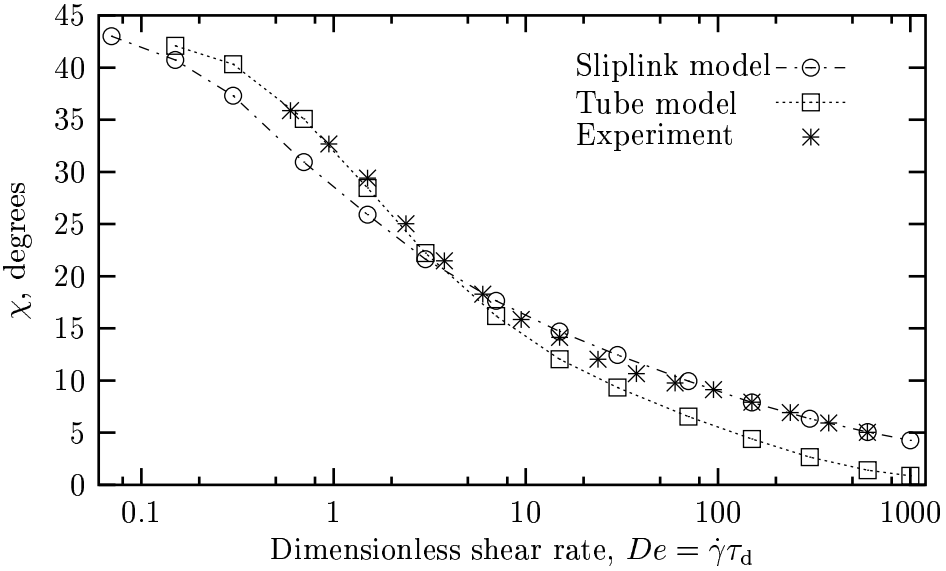

Figure 5.12. Steady state extinction angle as function of dimensionless shear rate.

Overall we can summarize this qualitative evaluation of the model in inception of steady shear and steady state shear, by noting that the steady state predictions are very encouraging. The shear stress is a monotonic function of shear rate, and at high shear rates the extinction angle is predicted to approach a non-zero plateau. Both of these results are improvements over the full-chain reptation model. The transient results reveal too much underdamping for both the extinction angle and the stresses. Also, the magnitude of the stress overshoots during start up of steady shear is too small as opposed to the full-chain reptation model, which overpredicts these overshoots.

5.7 Outlook

The study presented in this chapter has been focused on the derivation of the new full-chain temporary network model. Although the potential of the model has been demonstrated by consideration of its linear viscoelastic behavior in Section 5.5 and some nonlinear properties in Section 5.6, some questions of immediate interest remain.

First of all, it would be interesting to repeat the flow simulations from the previous section while assigning the end strands an orientation and letting these strands be deformed with the flow like the interior strands. This treatment of the ends closely resembles that of the full-chain reptation model and could possibly affect the transient behavior of the new model in a desirable way. As discussed in Chapter 3, too abrupt stress transients may be attributed to tumbling on a too small time scale, and since tumbling is largely governed by the dynamics of the chain ends, it is likely that different treatment of the chain ends in the new model may alter the transient predictions significantly.

It has already been demonstrated in Section 5.6 that alternative expressions for the free energy are possible within the framework of the model. It is possible that the small stress undershoots, which are observed during inception of steady shear in the above simulations, are an indication of too little chain stretching or rather too much chain retraction. If that is the case, it may be possible to introduce a new expression for $F_{\mathrm{S}}(\boldsymbol{Q}, N)$ as some kind of hybrid of Eq. (5.47) and Eq. (5.60), since the former expression allows only little chain retraction as seen in Figure 5.4.

Generalizations of advanced reptation models, such as those proposed by Mead *et al.* (1998); Hua and Schieber (1998); Öttinger (1999), are hard to make because of the tube confining the test chain. However, the model proposed here involves no tubes, and a number of generalizations might therefore be considered.

An obvious extension of the theory is to include constraint release, which is also part of the reptation models just mentioned. For the implementation of constraint release in the model, more options could be considered. An earlier proposed implement could be adopted, such as the one con-

sidered by Hua and Schieber (1998) (a random constraint on a random chain is released whenever the test chain abandons an entanglement) or by Öttinger (1999) (a noise term is added to the governing equation for orientation, which mimics continuous release and imposition of constraints). The latter mechanism could be implemented more rigorously in the new model in terms of probabilities of constraint release and imposition based on differences in free energy.

Generalization of the model to describe polymers with branched architecture could be obtained in the same manner. Namely, free energy differences could be used to determine the probability of moving a branch point through an entanglement point, the physical event equivalent with branch point withdrawal in the Pom-Pom model (McLeish and Larson, 1998).

Finally, extension of the theory to account for non-affine deformation should be considered. This could be incorporated in the model by means of force balances on the entanglements as recently suggested by Marrucci *et al.* (2000, 2001).

Acknowledgments

J.N. would like to thank the Danish government for financial support through the Technical University of Denmark (DTU).

J.D.S. would like to thank Professors M. Doi, T. Kawakatsu, and J. Takimoto for useful discussions during a visit to Nagoya University funded by the Doi Project, and for useful discussions with Professor Hans Christian Öttinger during a visit to ETH-Zurich.

References

Bird, R. B.; Curtiss, C. F.; Armstrong, R. C. and Hassager, O. (1987a). *Dynamics of Polymeric Liquids Vol. II: Kinetic Theory*. Wiley-Interscience, New York, second edition.

Bird, R. B.; Hassager, O.; Armstrong, R. C. and Curtiss, C. F. (1987b). *Dynamics of Polymeric Liquids Vol I: Fluid Mechanics*. Addison-Wesley, New York, second edition.

Cohen, A. (1991). A Padé approximant to the inverse Langevin function. *Rheol. Acta*, **30**, 270–273.

Doi, M. (1983). Explanation for the 3.4-power law for viscosity of polymeric liquids on the basis of the tube model. *J. Polym. Sci., Polym. Phys. Ed.*, **21**, 667–684.

Doi, M. and Edwards, S. F. (1986). *The Theory of Polymer Dynamics*. Clarendon Press, Oxford.

Fang, J.; Kröger, M. and Öttinger, H. C. (2000). A thermodynamically admissible reptation model for fast flows of entangled polymers. II. Model predictions for shear and extensional flows. *J. Rheol.*, **44**, 1293–1317.

Fetters, L. J.; Lohse, D. J.; Milner, S. and W.Graessley, W. (1999). Packing Length Influence in Linear Polymer Melts on the Entanglement, Critical and Reptation Molecular Weights. *Macromolecules*, **32**, 6847–6851.

Gardiner, C. W. (1982). *Handbook of Stochastic Methods for Physics, Chemistry and the Natural Sciences*. Springer-Verlag, Berlin, second edition.

Hua, C. C. and Schieber, J. D. (1998). Segment connectivity, chain-length breathing, segmental stretch, and constraint release in reptation models. I. Theory and single-step strain predictions. *J. Chem. Phys.*, **109**(22), 10018–10027.

Hua, C. C.; Schieber, J. D. and Venerus, D. C. (1998). Segment connectivity, chain-length breathing, segmental stretch, and constraint release in reptation models. II. Double-step strain predictions. *J. Chem. Phys.*, **109**(22), 10028–10032.

Hua, C. C.; Schieber, J. D. and Venerus, D. C. (1999). Segment connectivity, chain-length breathing, segmental stretch, and constraint release in reptation models. III. Shear Flows. *J. Rheol.*, **43**(3), 701–717.

Ketzmerick, R. and Öttinger, H. C. (1989). Simulation of a non-Markovian process modeling contour length fluctuation in the Doi-Edwards model. *Continuum Mech. Thermodyn.*, **1**, 113.

Marrucci, G.; Greco, F. and Ianniruberto, G. (2000). Simple strain measure for entangled polymers. *J. Rheol.*, **44**, 845–854.

Marrucci, G.; Greco, F. and Ianniruberto, G. (2001). Integral and differential constitutive equations for entangled polymers with simple version of CCR and force balance on entanglements. *Rheol. Acta*, **40**, 98–103.

McLeish, T. C. B. and Larson, R. G. (1998). Molecular constitutive equations for a class of branched polymers: The pom-pom model. *J. Rheol.*, **42**(1), 81–110.

Mead, D. W.; Larson, R. G. and Doi, M. (1998). A molecular theory for fast flows of entangled polymers. *Macromolecules*, **31**, 7895–7914.

Milner, S. T. and McLeish, T. C. B. (1998). Reptation and Contour-Length Fluctuations in Melts of Linear Polymers. *Phys. Rev. Letters*, **81**(3), 725–728.

Neergaard, J.; Park, K.; Venerus, D. C. and Schieber, J. D. (2000). Exponential Shear Flow of Linear, Entangled Polymeric Liquids. *J. Rheol.*, **44**(5), 1043–1054.

Öttinger, H. C. (1996). *Stochastic Processes in Polymeric Fluids*. Springer, Berlin.

Öttinger, H. C. (1999). A thermodynamically admissible reptation model for fast flows of entangled polymers. *J. Rheol.*, **43**, 1461–1493.

Öttinger, H. C. (2000). Personal communications.

Rault, J. (1987). Space filling an entanglements in polymeric systems. *J. Non-Newtonian Fluid Mech.*, **23**, 229–247.

Résibois, P. and Leener, M. D. (1977). *Classical Kinetic Theory of Fluids*. John Wiley and Sons, New York.

Treloar, L. R. G. (1958). *The Physics of Rubber Elasticity*. Clarendon Press, Oxford, second edition.

Appendices

A

Review of the Full-Chain Reptation Model

An essential part of this thesis is the full-chain reptation model recently proposed by Hua and Schieber (1998). Therefore, for the sake of completeness, we provide here a detailed description of the model and the simulation algorithm used to obtain numerical results as it appears in the original literature (Hua and Schieber, 1998; Hua *et al.*, 1999).

A.1 Model Description

Construction of the model consists of two parts: the first part describes the chain motion, which is governed by a set of stochastic differential equations; the second part prescribes the tube motion, which consists of two superimposed motions: a simple, deterministic, convection process, and a random, instantaneous constraint release process. The tube, which confines the motions of the polymer chain, is assumed to be convected with flow and be deformed affinely by the flow field. In addition, the tube can undergo a constraint release process anywhere along its contour. Its orientation is described by a finite set of connector vectors $\{\boldsymbol{u}_k\}$, whose number is stochastic. The chain is described by $N+1$ position *scalars* $\{s_k\}$, which describe the location of all beads within the tube. These scalars indicate the distance of each bead along the contour length measured along the path of the tube from an arbitrarily chosen origin.

The orientation of a polymer chain, which is modeled as a FENE bead-and-spring chain, is defined by the orientation of its confining tube. The only way a chain can escape from its confining tube is by random motion, or reptation, at the two ends. The length of the chain is determined by a stochastic differential equation. Note that, whereas the tube deforms affinely, the chains are not convected affinely with the flow because of the assumed frictional force with the tube. Thus, to find the length and orientation of a chain, one must solve the equations of motion for both the chain and the tube simultaneously.

First, we write the stochastic equation of motion (Langevin equation)

for the $N+1$ elastic chain beads:

$$\begin{aligned} 0 &= -\zeta\left[\dot{s}_0 - v_{\mathrm{T}}\left(s_0\right)\right] + F_1^{\mathrm{S}} + F_0^{\mathrm{EV}} + F_0^{\mathrm{B}}, \\ 0 &= -\zeta\left[\dot{s}_\nu - v_{\mathrm{T}}\left(s_\nu\right)\right] + F_{\nu+1}^{\mathrm{S}} - F_\nu^{\mathrm{S}} + F_\nu^{\mathrm{EV}} + F_\nu^{\mathrm{B}}, \quad \nu = 1, \ldots N-1 \\ 0 &= -\zeta\left[\dot{s}_N - v_{\mathrm{T}}\left(s_N\right)\right] - F_N^{\mathrm{S}} + F_N^{\mathrm{EV}} + F_N^{\mathrm{B}}, \end{aligned} \tag{A.1}$$

where s_ν is the position of the νth bead measured along the contour length of the tube from an arbitrarily chosen origin on the tube; $v_{\mathrm{T}}(s_\nu)$ is the tube velocity in the tangential direction along the tube relative to the chosen origin at the location of bead ν; ζ is the friction coefficient between an elastic-chain bead and the tube;

$$F_\nu^{\mathrm{S}} := \frac{H\left(s_\nu - s_{\nu-1}\right)}{1 - \frac{H}{k_{\mathrm{B}}T}\frac{\left(s_\nu - s_{\nu-1}\right)^2}{b}}$$

is the FENE spring force connecting the $(\nu-1)$th and the νth beads, where H denotes the Hookean spring constant, $k_{\mathrm{B}}T$ is the Boltzmann constant times the absolute temperature, and b is the square of the maximum dimensionless length that a chain segment can be stretched, or three times the number of Kuhn steps in the chain segment;

$$F_\nu^{\mathrm{B}} = \sqrt{2k_{\mathrm{B}}T\zeta}\, dW_\nu/dt$$

is the Brownian force acting on bead ν; W_ν describes the Wiener process for bead ν and satisfies $\langle W_\nu \rangle = 0$ and $\langle W_\nu(t) W_\mu(t') \rangle = \min(t, t')\delta_{\nu\mu}$; F_ν^{EV} is the excluded volume force that prevents the beads from passing through one another in the tube, and $N+1$ is the number of beads in the elastic chain. Here we assume that the excluded-volume potential is a hard-sphere well, and treat it with a reflecting boundary condition.

We subtract the $\nu = (n-1)$th equation from the $\nu = n$th one to construct another set of equations:

$$\begin{aligned} 0 &= -\zeta\left[\dot{s}_0 - v_{\mathrm{T}}\left(s_0\right)\right] + F_1^{\mathrm{S}} + F_0^{\mathrm{EV}} + F_0^{\mathrm{B}}, \\ 0 &= -\zeta\left[\dot{Q}_1 - \left(v_{\mathrm{T}}(s_1) - v_{\mathrm{T}}(s_0)\right)\right] + \left(F_2^{\mathrm{S}} - 2F_1^{\mathrm{S}}\right) + \left(F_1^{\mathrm{B}} - F_0^{\mathrm{B}}\right), \\ 0 &= -\zeta\left[\dot{Q}_n - \left(v_{\mathrm{T}}(s_n) - v_{\mathrm{T}}(s_{n-1})\right)\right] + \left(F_{n+1}^{\mathrm{S}} - 2F_n^{\mathrm{S}} + F_{n-1}^{\mathrm{S}}\right) \\ &\quad + \left(F_n^{\mathrm{B}} - F_{n-1}^{\mathrm{B}}\right), \qquad n = 2, \ldots., N-1, \\ 0 &= -\zeta\left[\dot{Q}_N - \left(v_{\mathrm{T}}(s_N) - v_{\mathrm{T}}(s_{N-1})\right)\right] + \left(-2F_N^{\mathrm{S}} + F_{N-1}^{\mathrm{S}}\right) \\ &\quad + \left(F_N^{\mathrm{B}} - F_{N-1}^{\mathrm{B}}\right), \end{aligned} \tag{A.2}$$

where $Q_i := s_i - s_{i-1}$ is the connecting scalar for the ith spring. Conceptually, Eq. (A.2) can be divided into two parts: the first equation describes the chain motion relative to the tube at one end, and the remaining equations describe the motion of the springs connecting two adjacent beads.

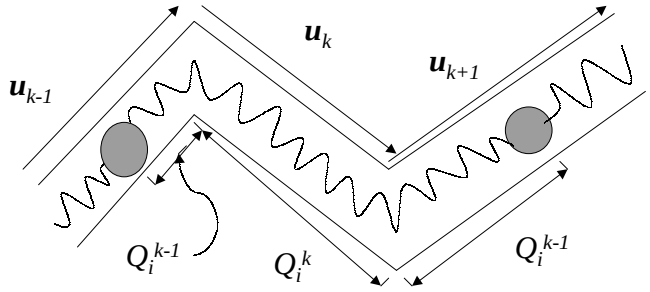

Figure A.1. Illustrative sketch where a chain segment is distributed over three tube segments.

The relative tube-stretching velocity at two beads, $v_{\mathrm{T}}(s_i) - v_{\mathrm{T}}(s_{i-1})$, can be determined analytically from the imposed flow field and the instantaneous orientation of the tube where the beads are located. For convenience, we give here the general formula for the velocity for a continuous chain ($N \to \infty$) relative to the chosen origin, even though the chain is actually discrete,

$$v_{\mathrm{T}}(s) = \boldsymbol{\kappa} : \int_0^s \frac{\boldsymbol{u}(s')\boldsymbol{u}(s')}{|\boldsymbol{u}(s')|^2} ds'. \tag{A.3}$$

For example, for the case sketched in Figure A.1, the relative tube velocity of the two beads is given by

$$\begin{aligned} v_{\mathrm{T}}(s_i) - v_{\mathrm{T}}(s_{i-1}) &= \boldsymbol{\kappa} : \left[\frac{\boldsymbol{u}_{k-1}\boldsymbol{u}_{k-1}}{|\boldsymbol{u}_{k-1}|^2} Q_i^{k-1} + \frac{\boldsymbol{u}_k \boldsymbol{u}_k}{|\boldsymbol{u}_k|^2} Q_i^k \right. \\ &\quad \left. + \frac{\boldsymbol{u}_{k+1}\boldsymbol{u}_{k+1}}{|\boldsymbol{u}_{k+1}|^2} Q_i^{k+1} \right], \end{aligned} \tag{A.4}$$

where $\boldsymbol{u}_k$ is the orientation vector of the kth tube segment; and Q_i^k is the part of Q_i confined in the kth tube segment.

The orientation of the tube segment during deformation from time t' to time t can be found by the deterministic time evolution described by

$$\boldsymbol{u}_k(t) = \boldsymbol{E}(t, t') \cdot \boldsymbol{u}_k(t'), \tag{A.5}$$

where $\boldsymbol{E}(t, t')$ is the deformation gradient tensor (for a definition see Eq. (8.1–4) of Bird *et al.* (1987)).

To be consistent with the original picture, we assume a Kramers-type expression for the polymer contribution to the stress (again for a continuous chain),

$$\boldsymbol{\tau}^{\mathrm{p}} = \frac{N n k_{\mathrm{B}} T}{3} \boldsymbol{\delta} - n \left\langle \int H Q(s) \frac{\boldsymbol{u}(s)\boldsymbol{u}(s)}{|\boldsymbol{u}(s)|^2} ds \right\rangle, \tag{A.6}$$

where $\boldsymbol{\delta}$ is the unit tensor, n is the number density of polymer, and the integral is over the entire length of the chain. For example, the integral evaluated over the length of the chain occupied by chain segment i of the discrete chain shown in Figure A.1 is given by

$$HQ_i \left(\frac{Q_i^{k-1}}{|\boldsymbol{u}_{k-1}|^2} \boldsymbol{u}_{k-1}\boldsymbol{u}_{k-1} + \frac{Q_i^{k}}{|\boldsymbol{u}_{k}|^2} \boldsymbol{u}_{k}\boldsymbol{u}_{k} + \frac{Q_i^{k+1}}{|\boldsymbol{u}_{k+1}|^2} \boldsymbol{u}_{k+1}\boldsymbol{u}_{k+1} \right). \quad \text{(A.7)}$$

We have obtained a complete set of equations for the chain and tube dynamics, Eqs. (A.2), (A.3) and (A.5). In the simulation, one can first find the tube orientation via Eq. (A.5), and then solve Eqs. (A.2) and (A.3) to obtain the new chain lengths and bead locations.

A.2 Simulation Algorithm

In this section, we describe the stochastic simulations used to obtain rheological properties. We first introduce the stochastic algorithm for finding the chain length and orientation, followed by a discussion of how constraint release is accomplished in the simulation.

A.2.1 Stochastic Algorithm

The discretized equations corresponding to Eq. (A.2) employing first order, Eulerian forward schemes are (shown for the case of a Hookean spring force):

$$\begin{aligned}
\Delta\bar{s}_0 &= \frac{H}{\zeta} Q_1(t)\,\Delta t + \sqrt{2k_{\mathrm{B}}T/\zeta}\,\sqrt{\Delta t}\,\xi_0, \\
Q_1(t+\Delta t) &= Q_1(t) + [v_{\mathrm{T}}(s_1) - v_{\mathrm{T}}(s_0)]\,\Delta t + \frac{H}{\zeta}[Q_2(t) - 2Q_1(t)]\,\Delta t \\
&\quad + \sqrt{2k_{\mathrm{B}}T/\zeta}\,\sqrt{\Delta t}\,(\xi_1 - \xi_0), \\
Q_n(t+\Delta t) &= Q_n(t) + [v_{\mathrm{T}}(s_n) - v_{\mathrm{T}}(s_{n-1})]\,\Delta t \\
&\quad + \frac{H}{\zeta}[Q_{n+1}(t) - 2Q_n(t) + Q_{n-1}(t)]\,\Delta t \\
&\quad + \sqrt{2k_{\mathrm{B}}T/\zeta}\,\sqrt{\Delta t}\,(\xi_n - \xi_{n-1}), \qquad n = 2, ..., N-1, \\
Q_N(t+\Delta t) &= Q_N(t) + [v_{\mathrm{T}}(s_N) - v_{\mathrm{T}}(s_{N-1})]\,\Delta t \\
&\quad + \frac{H}{\zeta}[-2Q_N(t) + Q_{N-1}(t)]\,\Delta t \\
&\quad + \sqrt{2k_{\mathrm{B}}T/\zeta}\,\sqrt{\Delta t}\,(\xi_N - \xi_{N-1}),
\end{aligned} \quad \text{(A.8)}$$

where $\Delta\bar{s}_0 := [\dot{s_0} - v_{\mathrm{T}}(s_0)]\,\Delta t$, and ξ_i is a random number whose distribution satisfies zero mean and unit variance. Note that $\Delta\bar{s}_0$ is the movement of the chain in the confining tube relative to one end. This quantity can be used to determine the chain reptation at that end of the tube. For

example, when $\Delta\bar{s}_0 < 0$, the chain reptates out of the tube by an amount of $-\Delta\bar{s}_0$ at that end.

Since the governing equation for a chain segment length, Q_i, is stochastic, the total chain length will also fluctuate with time. Such a situation is different from most earlier works that assume constant contour length by neglecting the Brownian forces on the beads. Also note that the information concerning chain connectivity, chain retraction, reptation, and the chain-length fluctuations are all consistently incorporated into Eq. (A.8). These processes follow from the mechanical model and are not put in by hand. Also note that no Maxwell demons are employed to prevent the chain from collapsing to a point in the tube. Finally, predictions can be made for general flow fields, unlike most previous modifications, which are either limited to equilibrium state or only a few types of flow fields.

The algorithm is simulated in the following way:

(i) First, we make the length and time dimensionless by the characteristic length $\sqrt{k_B T/H}$ and the characteristic time $\lambda_H := \zeta/4H$, respectively. Since the equilibrium chain length is stochastic, we first average the chain length over the whole ensemble of chains, and then divide the average chain length by $\langle Z\rangle_{eq}$ to obtain the average equilibrium tube segment length. For the same reason, the number of tube segments for each chain is stochastic and can be slightly different from the specified value of $\langle Z\rangle_{eq}$, even at equilibrium. During flow, the average number of entanglements can decrease dramatically.

(ii) The dimensionless time step size is chosen to be 0.2 for most of the simulations. Smaller values of the time step size have been tested, and the differences in predictions are found to be insignificant. During each time step, $N+1$ uniform random numbers that satisfy the distribution of ξ_i are created by a pseudo-random number generator, and the equation set in Eq. (A.8) is solved to find $\Delta\bar{s}_0$ and Q_i for a new time step for each polymer chain. Note that during each time step, bead overlap can occur, and these beads are relocated according to the hard-sphere, excluded-volume potential by a simple reflection algorithm which takes into account multiple bead overlappings.

(iii) The length and orientation of each tube segment at a new time step is determined by Eq. (A.5).

(iv) If $\Delta\bar{s}_0$ found from step (*ii*) is less than zero, that end of the chain will reptate out the tube by an amount $-\Delta\bar{s}_0$, in a random direction, and a new tube segment at that end should be created; otherwise, the chain segment on that end retracts and the tube segment at that end should be cut by an amount

$\Delta\bar{s}_0$. Note that in order not to introduce artificial effects from the chosen time step size, when a new tube segment is created, we will first fill out the tube segment to its full length before another new tube segment is created.

(v) After step (iv), if the new chain length turns out to be greater than the new tube length, then the chain segment on the other end will reptate out of the tube in a random direction, and a new tube segment should be created by an amount such that the total tube length equals the chain length. All beads are relocated hereafter using a redistribution subroutine such that the stochastic differential equation is solved, and no bead overlap occurs. Each bead could reside in a different tube segment at the new time step.

(vi) Having information of both the bead locations and the tube segment orientations, we can finally evaluate the polymer contribution to stress by Eq. (A.6).

A.2.2 Constraint Release

Consistent with our mean-field picture and the time discretization of our simulation algorithm, we assume that whenever a tube segment is destroyed by reptation, constraint release for some other chain segment *might* result. To add the constraint release mechanism to the stochastic algorithm described above, we first note that the entanglements are continuously renewed and destroyed because of chain reptation. Thus, we must find a criterion determining whether or not the constraint on a certain chain segment should be released when another tube segment reptates. In order to do that, we first recognize that a newly created tube segment presumably will not impose any new constraint on those tube segments already existing. Based on this idea, we can implement the constraint release mechanism in our simulation algorithm by adding one extra step between steps (v) and (vi); whenever an end tube segment u_e^j is destroyed by reptation, we randomly pick a kink formed by two tube segments, $\boldsymbol{u}_k^i$ and $\boldsymbol{u}_{k+1}^i$, where i and j denote two different polymer chains. If the time of creation of the chosen tube segments by reptation is prior to that of the destroyed end segment, then a constraint release will result; otherwise, there will be no constraint release. Once the constraint release occurs, we specify a new tube segment $\boldsymbol{u'}_k^i$ according to

$$\boldsymbol{u'}_k^i = \boldsymbol{u}_k^i + \boldsymbol{u}_{k+1}^i. \tag{A.9}$$

We expect the results to be independent of ensemble size, since the number of tube segments being destroyed by reptation increases linearly with the ensemble size, whereas the probability of a tube being selected at random from a single destruction decreases inversely with ensemble size. Hence,

the probability for a single tube segment to be selected for constraint release, which is the product of these two probabilities, is independent of ensemble size.

Note that during flow, the slip links, or entanglement points, in a single chain are destroyed by more mechanisms: chain retraction, chain-length fluctuations, reptation and constraint release. However, the entanglement points are simultaneously created by both chain reptation and chain-length fluctuations. The number of entanglements for a single chain fluctuates, and the average number results from a competition of these processes. During rapid deformations, the rate of destruction processes grows, whereas the creation processes are relatively unaffected by flow. Hence, the number of entanglements can decrease somewhat at high shear rates, for example.

References

Bird, R. B.; Hassager, O.; Armstrong, R. C. and Curtiss, C. F. (1987). *Dynamics of Polymeric Liquids Vol I: Fluid Mechanics*. Addison-Wesley, New York, second edition.

Hua, C. C. and Schieber, J. D. (1998). Segment connectivity, chain-length breathing, segmental stretch, and constraint release in reptation models. I. Theory and single-step strain predictions. *J. Chem. Phys.*, **109**(22), 10018–10027.

Hua, C. C.; Schieber, J. D. and Venerus, D. C. (1999). Segment connectivity, chain-length breathing, segmental stretch, and constraint release in reptation models. III. Shear Flows. *J. Rheol.*, **43**(3), 701–717.

B

Inflation and Instability of a Polymeric Membrane

We consider an axisymmetric polymeric membrane inflated by a uniform pressure difference acting across the membrane. The polymeric material is described by an arbitrary combination of a viscoelastic and a purely viscous component to the stress. Some viscoelastic materials described by a Mooney-Rivlin model show a monotone increasing pressure during inflation of a spherical membrane. These materials develop a homogeneous membrane thickness in agreement with the Considère-Pearson condition. Molecularly based models such as the neo-Hookean, Doi-Edwards or Tom-Pom model show a pressure maximum when inflated. Membranes described by these models develop a local thinning of the membrane which may lead to bursting in finite time. [1]

B.1 Introduction

The inflation of a membrane may be used to investigate the rheological properties of polymers (Wineman, 1978). However the deformation in inflating membranes is not homogeneous. In the axisymmetric inflation of a circular membrane the local material deformation ranges from equal biaxial stretching at the pole to planar elongation at the rim. Thus in order to obtain maximum rheological information from an inflation experiment it is necessary to have a simulation method for the inflation process. Moreover since the rheological modeling of polymer melts in biaxial and planar stretching is still in the developing stages, it is convenient for explorative purposes to have a formulation in which the constitutive equation may easily be exchanged. This was recognized in the pioneering developments by Wineman (1976, 1978, 1979). An elegant high order finite element method for the numerical analysis of viscoelastic inflation was introduced by Warby and Whiteman (1988). We here demonstrate that it is possible alternatively to construct a finite element method where the element coordinates converge to second order in the element size based on a locally

[1] This part of the work has been published in *J. Non-Newtonian Fluid Mech.*, **88**, 185–204 (1999).

zeroth order discontinuous stress description.

The mathematical treatment of membrane inflation was initially developed for elastic membranes.The developments were based on the theories for large strain elasticity with particular application to rubber materials (Mooney, 1940; Rivlin, 1948; Adkins and Rivlin, 1952; Green and Adkins, 1970). Thus Green and Adkins (1970) formulated a system of seven nonlinear ordinary differential equations for the description of the material motion in axisymmetrical membrane inflation. The unknowns are the radial position after deformation, the principal stretch ratios, the stress resultants and the principal curvatures. In later developments Yang and Feng (1970) and Wineman (1976, 1978) reformulated this description into systems of three first order nonlinear differential equations.

In what seems to have been the first application of the finite element method to the membrane inflation process, Oden and Sato (1967) replaced the continuum membrane by a set of triangular elements at the onset. A similar method was used by Charrier *et al.* (1987, 1989), who considered free and constrained inflation of elastic membranes and compared with carefully observed profiles of thin natural latex rubber membranes in axisymmetric as well as nonaxisymmetric geometries. In fact, the discretization of a membrane into triangular elements produces very flexible simulation methods and seems to form the basis for most commercial thermoforming simulation programs (see *e.g.* Novotný *et al.* (1998)). By contrast finite element methods based on a discretization of continuum equations (Cook, 1982; Fried, 1982) have been limited to axisymmetric inflation probably due to the lack of a mathematical formulation of the balance equations for a general 2D membrane surface embedded in a 3D space.

Simulations of thermoforming operations is frequently based on the assumption of large elastic strain with negligible relaxation (Khayat *et al.*, 1993). Indeed we have found the elastic deformation description to be a good prerequisite to the understanding of viscoelastic behavior. We therefore base our investigations on a general type of viscoelastic behavior that has the possibility for special choices of parameters to describe elastic response to fast deformations. Special consideration will be given to some molecular models for uncrosslinked linear and branched polymer melts. The fast deformation and instability of such materials is discussed in a companion paper (McKinley and Hassager, 1999). Finally it will be shown, that the addition of a small amount of viscosity will stabilize the deformation process.

B.2 Model equations

We consider the axisymmetric, unconstrained inflation of a thin polymeric membrane described in a cylindrical coordinate system (r, z) as shown in Figure 1. At time $t = 0$ the membrane is located at positions $z = 0$,

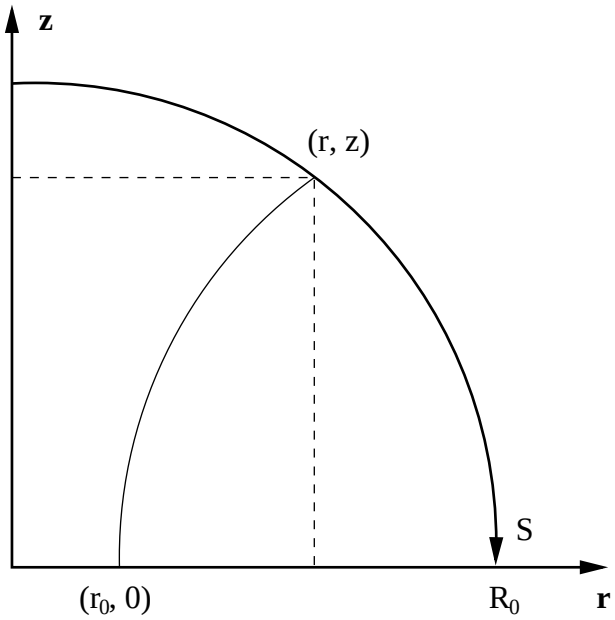

Figure B.1. Cross-section through membrane described in a cylindrical coordinate system showing the displacement of a particle from $(r_0, 0)$ to (r, z). Also shown is the arclength s from the pole measured along the membrane.

$r \in [0, R_0]$. The inflation for $t > 0$ is the result of a transmembrane pressure difference Δp which may be a function of time. The membrane is assumed to be so thin that inertia and stress gradients perpendicular to the plane of the membrane can be neglected. The membrane is fixed at the edge $(R_0, 0)$ so the material undergoes an inhomogeneous shearfree deformation (Bird *et al.*, 1987). A given material particle initially located at the position $(r_0, 0)$ is displaced at time t to a position (r, z). We use a Lagrangian description so the object becomes to determine the functions $r(r_0, t)$ and $z(r_0, t)$ for $r_0 \in [0, R_0]$ and $t > 0$ subject to the conditions that:

$$r(0, t) = 0, \quad r(R_0, t) = R_0, \quad z(R_0, t) = 0. \tag{B.1}$$

At each particle the principal directions of stretch are the meridional direction (1), the circumferential direction (2) and the direction normal to the membrane (3). The principal stretch ratios in these directions are (Wagner, 1994):

$$\lambda_1 = \sqrt{\left(\frac{\mathrm{d}r}{\mathrm{d}r_0}\right)^2 + \left(\frac{\mathrm{d}z}{\mathrm{d}r_0}\right)^2}, \quad \lambda_2 = \frac{r}{r_0}, \quad \lambda_3 = \frac{\delta}{\delta_0} \tag{B.2}$$

Here δ_0 is the uniform initial thickness of the membrane and $\delta(r_0, t)$ is the local thickness at time t. Incompressibility of the material is expressed by

$$\lambda_1 \lambda_2 \lambda_3 = 1 \tag{B.3}$$

We also introduce the notation t_1 for the traction (force pr. unit length in the 2-direction) transmitted in the 1-direction and t_2 for the traction

transmitted in the 2-direction. These are related to the membrane thickness and the principal stresses $(\tau_{11}, \tau_{22}, \tau_{33})$ as follows:

$$t_1 - \delta(\tau_{11} - \tau_{33}) = 0 \tag{B.4}$$

$$t_2 - \delta(\tau_{22} - \tau_{33}) = 0 \tag{B.5}$$

Two force balances are needed to describe the quasistatic equilibrium at each particle (Green and Adkins, 1970):

$$r\,\frac{\mathrm{d}t_1}{\mathrm{d}s} + \left(\frac{\mathrm{d}r}{\mathrm{d}s}\right)\,(t_1 - t_2) = 0 \tag{B.6}$$

$$\kappa_1\, t_1 + \kappa_2\, t_2 - \Delta p = 0 \tag{B.7}$$

Here s is the arclength along the membrane as shown in Figure 1. Also κ_1 and κ_2 are the principal curvatures in the meridional and circumferential directions:

$$\kappa_1 = \frac{\frac{\mathrm{d}^2 r}{\mathrm{d}s^2}}{\sqrt{1 - \left(\frac{\mathrm{d}r}{\mathrm{d}s}\right)^2}} \tag{B.8}$$

$$\kappa_2 = \frac{-\sqrt{1 - \left(\frac{\mathrm{d}r}{\mathrm{d}s}\right)^2}}{r} \tag{B.9}$$

It remains to relate the principal stresses to the deformation history by means of constitutive equations for the material. We wish to describe a material with relaxation in slow deformations and rubbery elastic behavior in fast deformations. Moreover we want to include the option of describing a glassy behavior in the limit of very fast deformations. We do this by splitting the extra stress $\boldsymbol{\tau}$, into a viscoelastic part $\boldsymbol{\tau_e}$ intended to model the rubbery behavior with relaxation and a viscous part $\boldsymbol{\tau_v}$ to model the glassy reaction as follows:

$$\boldsymbol{\tau}(t) = \boldsymbol{\tau}_v(t) + \boldsymbol{\tau}_e(t) \tag{B.10}$$

The viscous and the viscoelastic parts are described respectively by a Newtonian fluid model and a Rivlin-Sawyers integral model as follows:

$$\boldsymbol{\tau}_v(t) = -\beta\eta_0\dot{\boldsymbol{\gamma}}(t) \tag{B.11}$$

$$\boldsymbol{\tau}_e(t) = \int_{-\infty}^{t} M(t-t')\left[\phi_1(I_1, I_2)\boldsymbol{\gamma}_{[0]} + \phi_2(I_1, I_2)\boldsymbol{\gamma}^{[0]}\right] dt' \tag{B.12}$$

Here η_0 is the zero shear-rate viscosity composed of a contribution $\beta\eta_0$ from $\boldsymbol{\tau}_v$ and contribution $\int_0^\infty M(s)sds = (1-\beta)\eta_0$ from $\boldsymbol{\tau}_e$. The notation for the tensors is that of Bird *et al.* (1987) and the two damping functions are constrained by

$$\phi_1(3,3) + \phi_2(3,3) = 1 \tag{B.13}$$

The principal stresses for the viscous contribution to the stress may be expressed in a form convenient for the Lagrangian specification as follows:

$$\tau_{ii} = -2\beta\eta_0 \frac{\mathrm{d}}{\mathrm{d}t} \ln \lambda_i, \quad i = 1, 2, 3. \tag{B.14}$$

The resistance to fast deformations is recognized in the time derivatives, which make instantaneous deformations impossible for materials when $\beta > 0$. Conversely when $\beta = 0$ the model may describe a rubbery elastic material in the limit of fast deformations. Thus provided $\beta = 0$ and the integral $G = \int_0^\infty M(s)ds$ exists, the fast deformation limit is given by

$$\boldsymbol{\tau} = G\left[\phi_1(I_1, I_2)\boldsymbol{\gamma}_{[0]} + \phi_2(I_1, I_2)\boldsymbol{\gamma}^{[0]}\right] \tag{B.15}$$

where G is the plateau modulus. For illustrative purposes we investigate here the fast behavior of several materials with a molecular origin.
The *neo-Hookean* model (Rivlin, 1948) for permanently crosslinked elastomers (Treloar, 1958) is obtained with the combination:

$$(\phi_1, \phi_2) = (1, 0)$$

The *Mooney-Rivlin* model (Mooney, 1940) model is obtained with the combination:

$$(\phi_1, \phi_2) = (\phi, 1 - \phi)$$

for constant values of $\phi \in [0, 1]$. The molecular origin of the ϕ_2 term has been discussed by Wagner (1994).
The fast deformation limit (McKinley and Hassager, 1999) of the *Doi-Edwards* model (Doi and Edwards, 1978) for uncrosslinked linear polymer chains is obtained in the Currie approximation (Currie, 1982) with:

$$(\phi_1, \phi_2) = 5(1, (I_2 + 13/4)^{-1/2})/(J - 1), \quad \text{where} \quad J = I_1 + 2(I_2 + 13/4)^{1/2}$$

The fast deformation limit (McKinley and Hassager, 1999) of the *Tom-Pom* model (McLeish and Larson, 1998) for uncrosslinked linear($q = 1$) and branched($q \geq 2$) polymer chains. is obtained with:

$$(\phi_1, \phi_2) = \begin{cases} (1, 0), & I_1 \leq 3q^2 \\ 3(1, 0)q^2/I_1, & I_1 > 3q^2 \end{cases} \tag{B.16}$$

Here $q \in \mathbb{N}$ is the number of branches. For $q = 1$ the model describes linear chains and can be recognized as as an even simpler approximation to the Doi-Edwards model than the Currie approximation.

B.3 Finite element equations

In the numerical algorithm it is possible to discretize just $r(r_0, t)$ and $z(r_0, t)$. However, as noted by Warby and Whiteman (1988), an algorithm

in which it is easy to change the constitutive equation is obtained if the tractions $t_1(r_0,t)$ and $t_2(r_0,t)$ are also discretized. We follow their procedure in this respect, so our model equations are Eqs. (B.4) – (B.7). The boundary conditions for the problem are:

$$r(0,t)=0,\;\; r(R_0,t)=R_0,\;\; z(r_0,t)=0. \tag{B.17}$$

There are no boundary conditions for the tractions. As a consequence of this asymmetry in the variables we have found it natural to interpolate the tractions with lower order polynomials than the coordinates. Let the interval $r_0\in[0,R_0]$ be divided into a total of N elements connected by $N+1$ nodes. Then the coordinates and tractions are interpolated by the following functions:

$$\hat{r}(r_0,t)=\sum_{n=1}^{N+1} r^n(t)\;\omega_n(r_0),\quad \hat{z}(r_0,t)=\sum_{n=1}^{N+1} z^n(t)\;\omega_n(r_0) \tag{B.18}$$

$$\hat{t_1}(r_0,t)=\sum_{n=1}^{N} t_1^n(t)\;\psi_n(r_0),\quad \hat{t_2}(r_0,t)=\sum_{n=1}^{N} t_2^n(t)\;\psi_n(r_0) \tag{B.19}$$

The $(\hat{r},\hat{z})$ are linear within each element, continuous at the nodes. The $(\hat{t_1},\hat{t_2})$ are constant within each element and discontinuous at the coordinate nodes. The essential boundary conditions for the problem imply that

$$r^1(t)=0,\;\; r^{N+1}(t)=R_0,\;\; z^{N+1}(t)=0 \tag{B.20}$$

We use the following Galerkin weak form of the model:

$$F_{1,m}=\int_0^S \hat{r}\,\frac{\mathrm{d}\hat{t_1}}{\mathrm{d}s}\,\omega_m\,ds+\int_0^S(\hat{t_1}-\hat{t_2})\,\frac{\mathrm{d}\hat{r}}{\mathrm{d}s}\,\omega_m\,ds=0,\;\; m=2,\cdots N \tag{B.21}$$

$$F_{2,m}=\int_0^S\left(1-\left(\frac{\mathrm{d}\hat{r}}{\mathrm{d}s}\right)^2\right)\,\frac{\hat{t_2}}{\hat{t_1}}\,\omega_m\,ds-\int_0^S\frac{\mathrm{d}^2\hat{r}}{\mathrm{d}s^2}\,\hat{r}\,\omega_m\,ds+$$

$$\int_0^S\frac{\Delta p}{\hat{t_1}}\sqrt{1-\left(\frac{\mathrm{d}\hat{r}}{\mathrm{d}s}\right)^2}\,\hat{r}\,\omega_m\,ds=0,\;\; m=1,\cdots N \tag{B.22}$$

$$F_{3,m}=\int_0^S\left(\hat{t_1}-\delta(\tau_{11}-\tau_{33})\right)\,\psi_m\,ds=0,\;\; m=1,\cdots N \tag{B.23}$$

$$F_{4,m}=\int_0^S\left(\hat{t_2}-\delta(\tau_{22}-\tau_{33})\right)\,\psi_m\,ds=0,\;\; m=1,\cdots N \tag{B.24}$$

We have found it more convenient to formulate the derivatives in these equations in terms of the arclength s rather than the independent variable

r_0. The two formulations are related of course through $ds = (ds/dr_0)\, dr_0$. Eqs. (B.21) and (B.22) are reformulated as follows:

$$F_{1,m} = -\int_0^S \hat{t_1}\, \hat{r}\, \frac{\mathrm{d}\omega_m}{\mathrm{d}s}\, ds - \int_0^S \hat{t_2}\, \frac{\mathrm{d}\hat{r}}{\mathrm{d}s}\, \omega_m\, ds = 0, \quad m = 2, \cdots N \tag{B.25}$$

$$F_{2,m} = \int_0^S \frac{\hat{t_2}}{\hat{t_1}}\, \omega_m\, ds + \int_0^S \frac{\hat{t_1} - \hat{t_2}}{\hat{t_1}} \left(\frac{\mathrm{d}\hat{r}}{\mathrm{d}s}\right)^2 \omega_m\, ds +$$

$$\int_0^S \hat{r}\, \frac{\mathrm{d}\hat{r}}{\mathrm{d}s}\, \frac{\mathrm{d}\omega_m}{\mathrm{d}s}\, ds + \int_0^S \frac{\Delta p}{\hat{t_1}} \sqrt{1 - \left(\frac{\mathrm{d}\hat{r}}{\mathrm{d}s}\right)^2}\, \hat{r}\, \omega_m\, ds = 0, \quad m = 1, \cdots N \tag{B.26}$$

Eqs. (B.23) – (B.26) together with Eq. (B.20) represent a total of $4N + 2$ equations for the determination of the $(r^n(t), z^n(t))$, $n = 1, \cdots N + 1$ and $(t_1^n(t), t_2^n(t))$, $n = 1, \cdots N$. The variables are further discretized in the time variable and solved at each time step with a Newton iteration.

The convergence of the method was investigated by systematically increasing the number of elements to a maximum of 320. The height of the pole obtained with 320 elements was then defined as the "exact" value and an estimate of the error introduced by using a coarser element discretization calculated as $\epsilon = |z^{320} - z^N|$. Typical results for ϵ as function of the length of the elements $\Delta r_0 = R_0/N$ are shown in Figure 2. It appears that to a good approximation $\epsilon \propto \Delta r_0^2$ indicating that the method converges to second order with the element size.

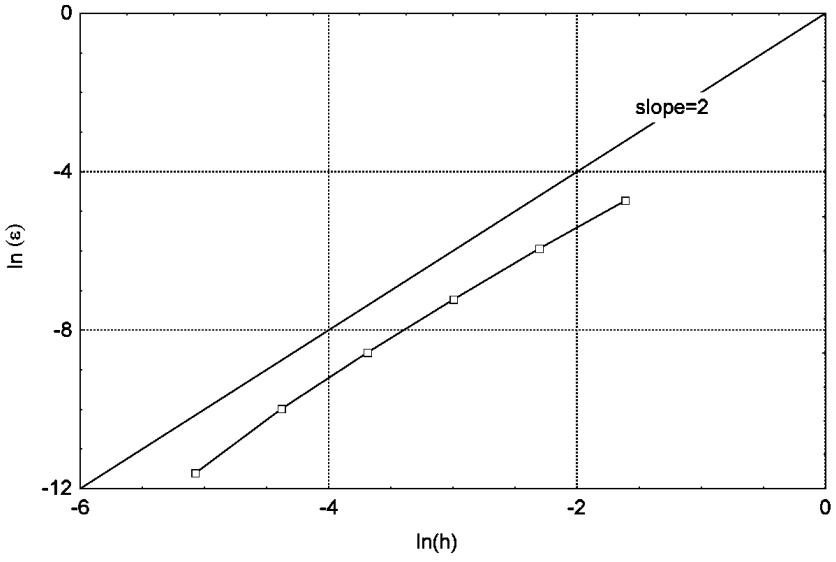

Figure B.2. Illustration of the second order convergence in the element length Δr_0.

B.4 Elastic inflation

We consider in some detail the purely elastic inflation based on the constitutive equation (Eq. (B.15)) for several reasons. Many thermoforming operations are in fact modeled as elastic deformations. This is sometimes referred to as a hyperelastic description (Khayat *et al.*, 1993). It has been used recently for the identification of material constants of acrylonitrile-butadiene-styrene (Derdouri *et al.*, 1998). Moreover the fast elastic response gives important information about the tensorial character of the constitutive equations also for viscoelastic materials.

B.4.1 Homogeneous spherical shell model

It is useful to have some *a priori* estimate of the magnitude of the deformations that can be expected for a given pressure difference. For this purpose we consider the rough homogeneous spherical shell model shown in Figure 3. The relation between pressure and deformation is based on the following two assumptions:

1. The membrane is inflated into the shape of a spherical shell of uniform thickness δ and radius of curvature R.

2. The principal stresses in the membrane can be computed from a homogeneous biaxial deformation of the same increase in area as that of the membrane.

We realize that these assumptions are not kinematically possible due to the stick condition at the rim. However the simple model still provides

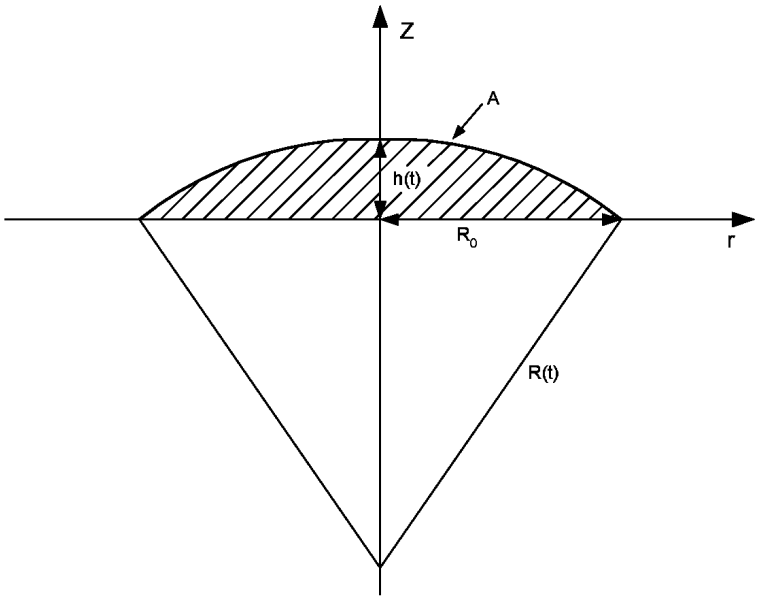

Figure B.3. The spherical shell model with radius of curvature R, height h and area $A = 2\pi hR$.

useful guidance for the finite element simulations. The radius of curvature of the sphere is related to the radius of the undeformed membrane R_0 and the height of the membrane h as follows:

$$R = \frac{R_0^2 + h^2}{2\ h} \tag{B.27}$$

Then for small values of h/R_0 the relation between pressure and deformation becomes approximately,

$$\Delta p \approx 12\ \frac{G\ \delta_0}{R_0}\ \left(\frac{h}{R_0}\right)^3 \tag{B.28}$$

This relation may be used to provide initial values for the Newton iteration for small deformations. It is also of interest to note the following relation between the stretch ratio λ of the material and the height:

$$\frac{h}{R_0} = \sqrt{\lambda^2\ -\ 1} \tag{B.29}$$

For biaxial inflation of a homogeneous spherical shell of a given material a critical situation occurs when the pressure vs. volume exhibits a maximum. The significance of this pressure maximum in terms of a possible instability seems to have been first pointed out by Cogswell and Moore (1974) based on a suggestion by Pearson. We denote the criterion for pressure maximum the *Considère-Pearson* criterion to distinguish it from the Considère criterion that applies to maximum force in uniaxial extension. The critical stretch ratios λ_c for pressure maximum in homogeneous biaxial extension derived recently (McKinley and Hassager, 1999) for a number of molecularly based models are given in Table 1. It is not immediately obvious how the λ_c should be interpreted in the membrane inflation problem under consideration since it involves an inhomogeneous mixture of biaxial and planar deformations. We have chosen to translate the exact values of λ_c into expected critical values for the height of the membranes h_c by

Model	Ratio λ_c	h_c/R_0
Neo-Hookean	1.3831	0.96
Mooney($\phi = 0.8234$)	1.8407	1.54
Mooney($\phi < 0.8234$)	(no maximum)	(no maximum)
Doi-Edwards-Currie	1.3022	0.83
Tom-Pom($q = 1$)	1.2400	0.73
Tom-Pom($q \geq 2$)	1.3831	0.96

Table B.1. Critical conditions for the inflation of membranes: λ_c: Stretch ratio for pressure maximum in biaxial inflation. h_c: Predicted corresponding height of polymer membrane.

means of the homogeneous spherical shell model in Eq. (B.29). Thus the h_c in Table 1 are the estimated critical heights of inflation for the polymer membrane as predicted from the Considère-Pearson criterion and the homogeneous spherical shell model.

Note that the Mooney model would predict instability for $\phi > 0.8234$ and no instability for $\phi < 0.8234$. The second entry in the table gives the stretch ratio at the limiting value of the parameter $\phi = 0.8234$ for which the maximum in the Considère-Pearson function becomes an inflection point. Also note, that the critical stretch ratio for the Tom-Pom model for branched polymer melts ($q \geq 2$) is identical to that of the neo-Hookean material inasmuch as Considère-Pearson instability occurs before $I_1 = 3q^2$.

B.4.2 Numerical results

Due to the occurence of a Considère-Pearson instability in the homogeneous spherical shell model as well as in previous observations (Green and Adkins, 1970), we can expect the occurence of a pressure maximum in the full finite element simulations of membrane inflation. Consequently we let the pressure be a dependent variable. In practice this is done by introducing the membrane height at the pole h as a new independent variable and augmenting the system of equations with $z_1 - h = 0$. We present our results in terms of the nondimensional height h/R_0 and the nondimensional pressure:

$$P = \frac{\Delta p \; R_0}{\delta_0 \; G} \tag{B.30}$$

The membrane shapes for the neo-Hookean model and the Mooney model

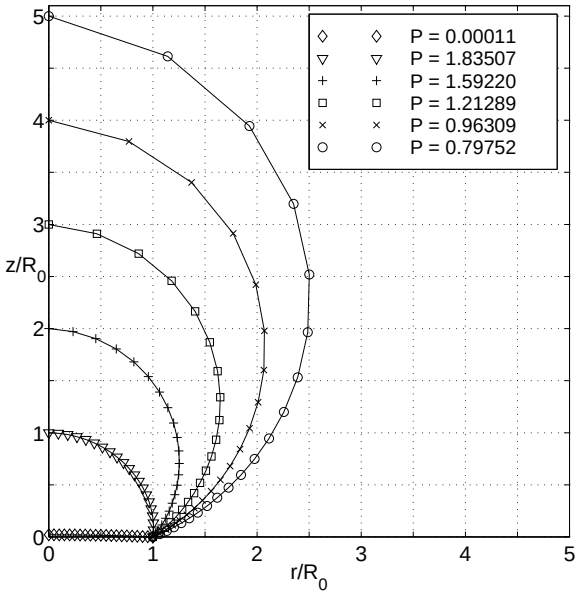

Figure B.4. Inflation profiles for elastic deformation of a neo-Hookean material.

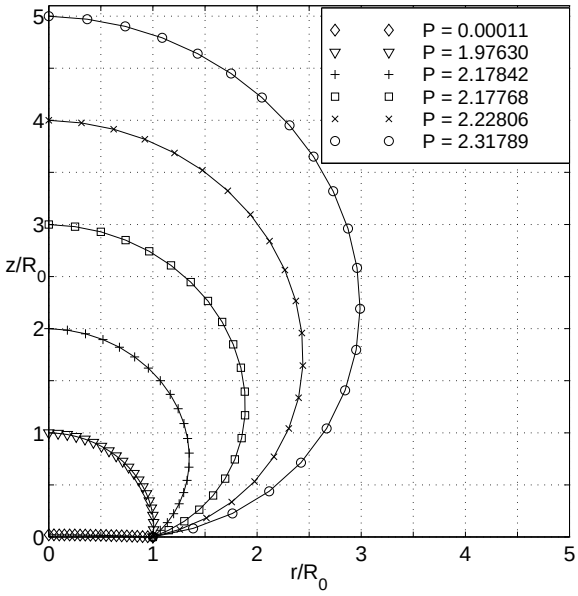

Figure B.5. Inflation profiles for elastic deformation of a Mooney-Rivlin material ($\phi = 0.95$).

($\phi = 0.95$ and $\phi = 0.00$) are shown in Figures 4, 5 and 6 respectively. The result of the Considère-Pearson instability in the neo-Hookean profile is seen in the very large stretch ratio in the element near the z-axis. This results in a strong thinning in the membrane thickness near the pole. By contrast for $\phi = 0.95$ in Figure 5 the stretch ratio and membrane thickness is stabilized near the pole. Finally in Figure 6 we observe a large value of λ_1

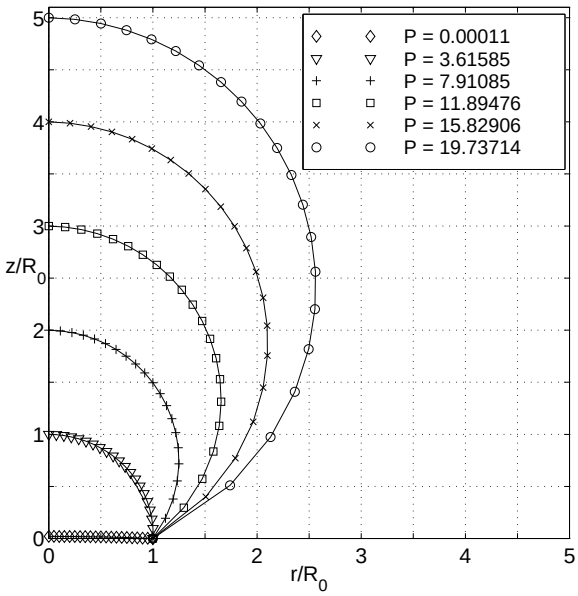

Figure B.6. Inflation profiles for elastic deformation of a Mooney-Rivlin material ($\phi = 0.00$).

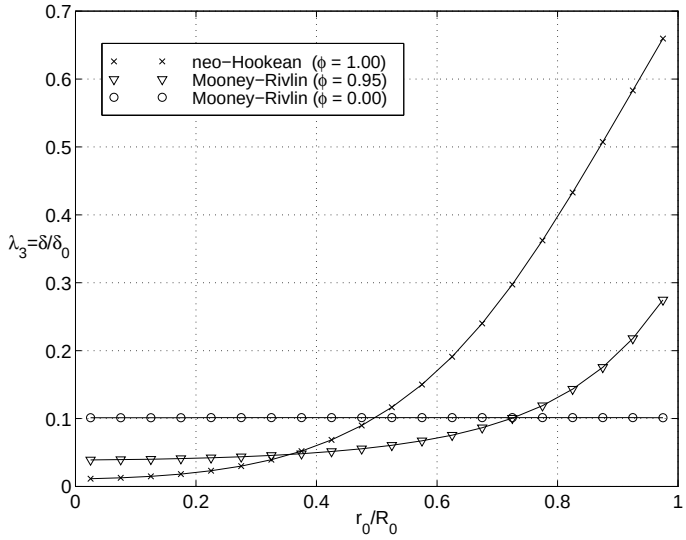

Figure B.7. Thickness distribution for elastic inflation of three membranes to a total height of $h/R_0 = 3$.

near the rim. Thus although the profiles in Figures 4, 5 and 6 may appear similar, that similarity hides large differences in the distribution of the thickness of the material such as would be important in thermoforming operations. This is illustrated in Figure 7 where the thickness δ/δ_0 is plotted as function of r_0/R_0. The Mooney-Rivlin material with $\phi = 0$ has practically uniform thickness, while the strong thinning of the neo-Hookean material is evident near the pole.

The pressures corresponding to a set of ϕ-values are shown in Figure 8. The instability for the neo-Hookean material is visible as a pressure maximum in the simulations. The corresponding critical nondimensional height is $h/R_0 = 1.18$ which is to be compared with the approximate value of 0.96 from Table 1. Apparently the shell model provides a conservative estimate of the magnitude of the critical deformation. Moreover note from Table 1 that the Considère-Pearson condition suggests that stability of inflation is guaranteed with a weighting of about 18% of the $\boldsymbol{\gamma}^{[0]}$-tensor relative to the sum of the two strain tensors. The full numerical simulations in Figure 8 clearly show that stability is certainly obtained with 10% weighting of the $\boldsymbol{\gamma}^{[0]}$-tensor. The simulations are consistent with the suggestion that the Considère-Pearson criterion is a sufficient but not necessary condition for stability of inflation.

It is seen, that the behavior in fast elastic membrane inflation is very sensitive to the ϕ-parameter in the Mooney model. This fact can be understood in terms of the dependence of the corresponding strain energy function ($w = [\phi I_1 + (1-\phi)I_2]/2$) in the available invariant space (e.g. Figure 8.3-1 of Bird *et al.* (1987)). When $\phi = 1$ the strain energy increases very slowly along the curve for biaxial stretching. It is interesting to note, that while the relative weighting of the two strain tensors is of of

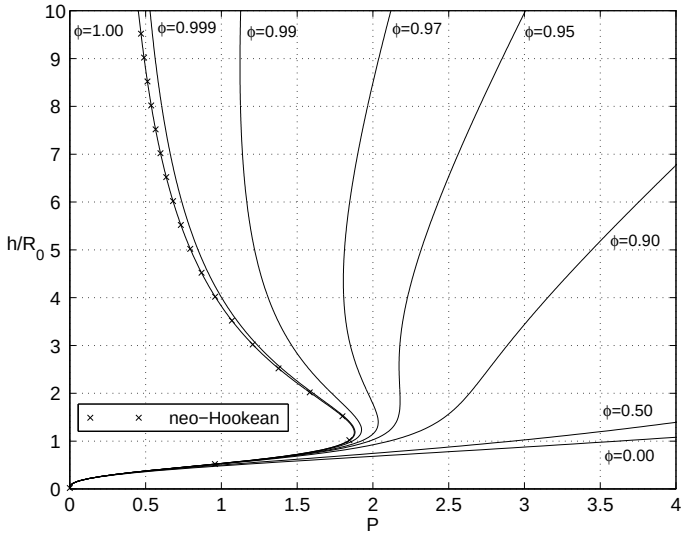

Figure B.8. Relation between the membrane height and pressure for a range of constant values of the ϕ-parameter in the Mooney-Rivlin model. The critical point for the neo-Hookean material is located at (1.88,1.18).

key importance in thermoforming operations, the weighting is in shear related to the second normal stress difference, a quantity that is not easily measured and often considered to be of minor industrial interest.

In Figure 9 the corresponding plot for the Tom-Pom model ($q = 1, 2, 3$) and the Doi-Edwards-Currie model is contrasted with the neo-Hookean model and the Mooney model for $\phi = 0$. It is seen that the Tom-Pom model for $q = 1$ becomes unstable at even lower strains than the neo-

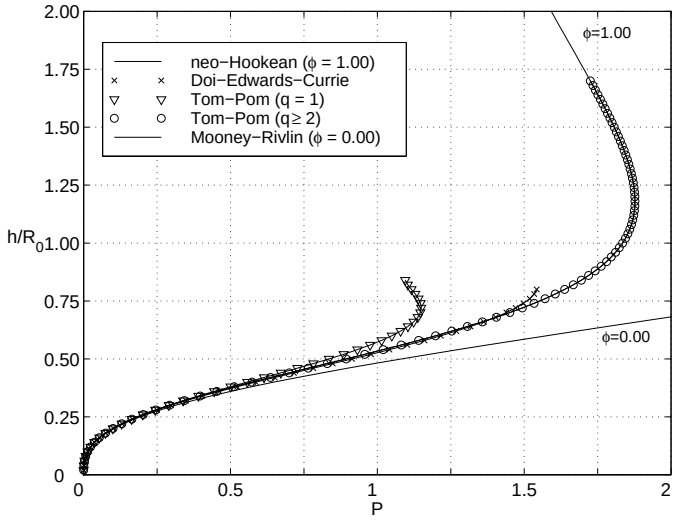

Figure B.9. Relation between the membrane height and pressure for the Tom-Pom model ($q = 1, 2, 3$) and the Doi-Edwards-Currie model contrasted with the neo-Hookean model and the Mooney-Rivlin model($\phi = 0$). The Tom-Pom model for $q = 2, 3$ follows the neo-Hookean model exactly.

Hookean model. The simulation shows a critical height of $h/R_0 = 0.72$ which compares very well with the approximate value of 0.73 from Table 1. The curve terminates at $h/R_0 = 84$. As explained in more detail in Section B.6 this reflects a failure of the material. This is in contrast to the behavior of the neo-Hookean material which continues to large values of h/R_0 albeit with a stong local thinning of the material near the pole. For $q \geq 2$ the Tom-Pom model follows the behavior of the neo-Hookean model until the strain becomes sufficient to induce branch-point withdrawal ($I_1 > 3q^2$) (McKinley and Hassager, 1999). This happens after the position of maximum pressure.

The numerical simulations for the Doi-Edwards-Currie model terminate at a critical height of $h/R_0 = 0.80$ which likewise compares well with Table 1. Keep in mind, that the neo-Hookean model was derived for a polymeric network, while the Tom-Pom model for $q = 1$ and the Doi-Edwards model were derived for uncrosslinked linear polymer chains. Thus it is not surprising that the neo-Hookean model is more stable in membrane inflation than the Tom-Pom($q = 1$) and Doi-Edwards models (which should be more or less identical).

B.5 Viscoelastic inflation (constant pressure)

We consider here a step change in pressure from zero to a constant value. We wish to model the transient inflation that results when $\beta > 0$. In rheological terms this may be described as an inhomogenoues creep test for a mixture of biaxial and planar elongation. In order to get an accurate description of the transient inflation of a given material it would be necessary to determine the memory function $M(s)$ as well as β from measurements of the linear viscoelastic properties. However in order to explore the types of response possible we assume that the viscoelastic stress is dominated by just one relaxation time so that

$$M(s) = (1 - \beta)\frac{\eta_0}{\lambda^2}\exp(-s/\lambda) \tag{B.31}$$

where λ is the dominant time constant. Furthermore we restrict the simulations at constant pressure to the combination $\phi_1 = 1, \phi_2 = 0$. Thus in effect we consider an Oldroyd-B model with a relaxation time λ and a "retardation" time $\beta\lambda$.

B.5.1 Approximate viscous response

When $\beta > 0$ the initial response is dominated by the viscous (retardation) term. In fact the homogeneous spherical shell model may be used to get an idea of the time scale for the viscous response to a step change in pressure. Imagine a flat membrane at rest which is at time $t = 0$ suddenly subjected to a step change in the pressure of magnitude Δp. The initial

response will then be determined only by the viscosity of the material $\beta\eta_0$. According to the homogeneous spherical shell model, the height of the membrane can be shown to develop according to:

$$\Delta p = 24\beta\eta_0\delta_0 R_0^2 \frac{h^2}{\left(R_0^2 + h^2\right)^3} \frac{\mathrm{d}h}{\mathrm{d}t} \tag{B.32}$$

When $h(t) \ll R_0$ the solution with $h(0) = 0$ is:

$$\frac{h(t)}{R_0} \approx \frac{1}{2}\sqrt[3]{\frac{t}{\tau_s}}, \quad \tau_s = \frac{\beta\eta_0\delta_0}{\Delta p\, R_0} \tag{B.33}$$

It is seen that the response although not instantaneous is very fast for small times. The solution above is useful for providing initial values for the Newton iteration in the numerical solution. The addition of a small amount of viscous response in itself may be used as a numerical stabilizer for discontinuous changes in pressure.

B.5.2 Numerical results

To illustrate the control of the initial response to a step change in pressure obtained with a viscous component we show in Figure 10 the membrane height as function of time scaled with the viscous time scale τ_s introduced in Eq. (B.33). We have used the fixed value of $\beta = 0.05$. Also shown in the figure is the numerical result for the completely Newtonian membrane ($\beta = 1$). It is seen that for sufficiently high values of the nondimensional pressure, the development in the membrane height is given just by the

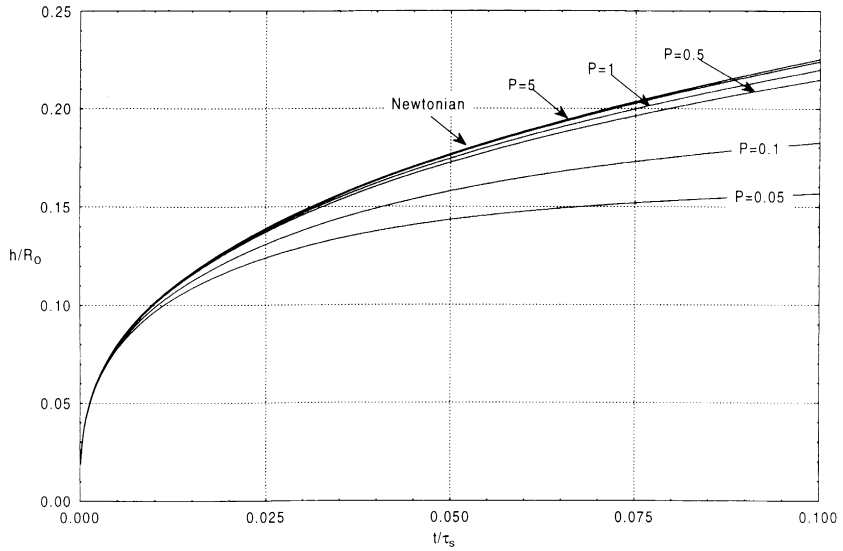

Figure B.10. Membrane height as function of time for the Oldroyd-B model with a fixed value of $\beta = 0.05$ shown for a variety of pressures. Time t is scaled with a time constant based on the instantaneous or solvent viscosity.

viscous contribution to the stress. That is to be expected since for large P the instantaneous equilibrium deformation would be very large, and so the deformation becomes controlled by the viscous response. In fact for $P = 5$ there would be no equilibrium position in fast elastic deformation of a membrane with $\beta = 0.00$, as seen in Figures 8 and 9. Nevertheless the transient response is well defined and controlled due to the small viscous component included ($\beta = 0.05$). Conversely for small pressures ($P = 0.05$) the viscoelastic stresses start to limit the deformation at an early stage.

Also we may illustrate the effect of changing the amount of viscous vs. viscoelastic stress at fixed values of the pressure difference. For this purpose we introduce a time scale based on the zero shear-rate viscosity:

$$\tau_0 = \frac{\eta_0 \delta_0}{\Delta p \; R_0} \tag{B.34}$$

Based on this time scale we show in Figure 11 the development of the membrane height for a fixed value of $P = 0.1$ and a sequence of β-values. The value of $\beta = 1$ is a Newtonian fluid while the value $\beta = 0$ (not shown) would correspond to an upper convected Maxwell model. The latter model would give an instantaneous jump to $h/R_0 \approx 0.2$ according to Figure 9. This tendency can be seen in the graph for $\beta = 0.05$. The relaxation of the material can also be seen in the slope of the lines. To get a feeling for the relaxation note that $t/\lambda = t/(\tau_0 P)$. Hence $t/\tau_0 = 0.1$ corresponds to $t/\lambda = 1$ so it is reasonable that the material relaxation can be seen.

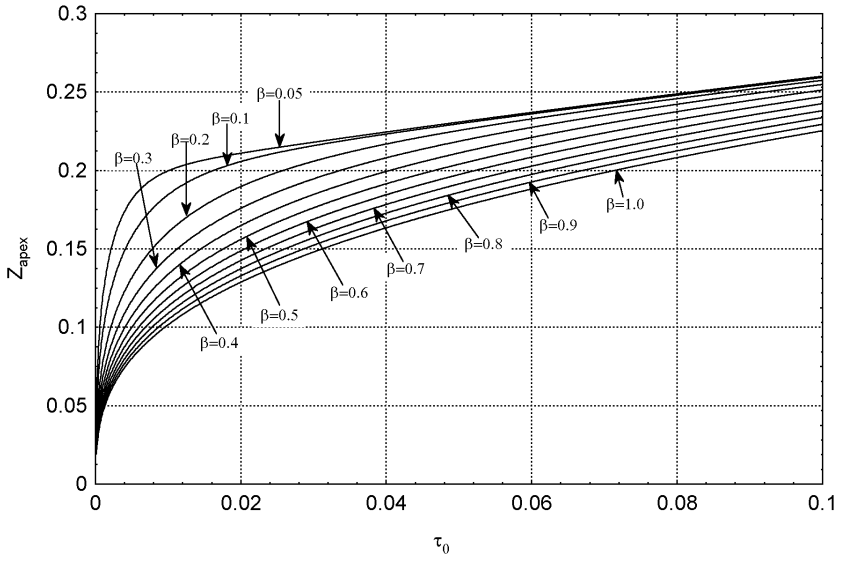

Figure B.11. Membrane height as function of time for the Oldroyd-B model for a fixed pressure $P = 0.1$ shown for a variety of relative amounts of solvent viscosity β. Time t is scaled with a time constant based on the total viscosity.

B.6 Viscoelastic inflation (constant volume flow)

Finally we illustrate the inflation of a membrane due to a constant flow rate of an incompressible fluid. Thus given a constant volume rate of flow Q the volume bounded by the inflated membrane becomes Qt at time t. In this situation the pressure difference becomes a dependent variable whereas time is now the independent variable. In practice this is done by augmenting the system of equations with a volume balance. Furthermore we assume that the inflation is so rapid that there is no relaxation of the viscoelastic term. That is to say we use the rapid deformation limit in Eq. (B.15) for the Rivlin-Sawyers model. When $\beta = 0$ this solution procedure traces through exactly the same membrane profiles and pressure values shown in Figures 4 – 9 where the height is the independent variable. However we now investigate the consequences of adding a small retardation term. It follows from Eq. (B.32) that for $\beta > 0$ the resulting pressure is given approximately by:

$$\Delta p \approx \frac{192\beta\eta_0 Q}{\pi R_0^3}\left(\frac{\delta_0}{R_0}\right)\left(\frac{Qt}{\pi R_0^3}\right)^2 \tag{B.35}$$

This approximate relation that applies for small values of $Qt/\pi R_0^3$ is used to obtain initial estimates for the Newton iteration in the first time step of the numerical algorithm. We show then in Figure 12 traces of height vs. pressure for a number of materials with the fixed value of $\beta = 0.01$. In Figure 12 both h/R_0 and P are computed quantities the independent variable being time which is not shown. The traces depend on the rate of

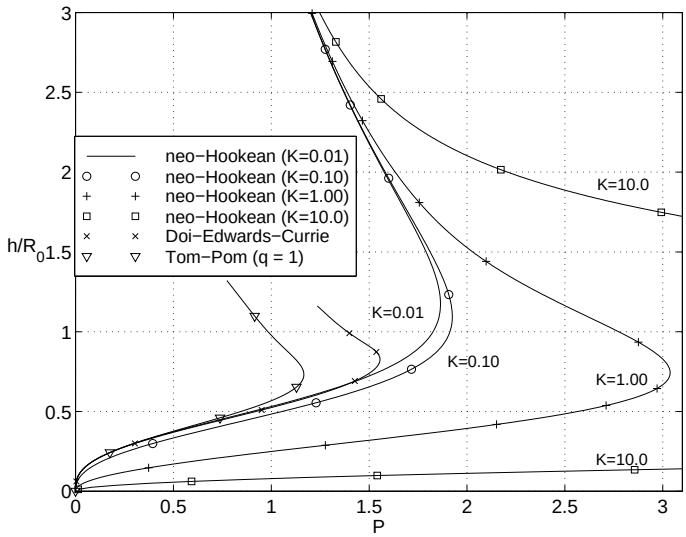

Figure B.12. Relation between the membrane height and pressure for a fixed value of $\beta = 0.01$. Results are shown for $K = 0.01$ for the modified Tom-Pom ($q = 1$) and Doi-Edwards-Currie models and for various values of K for the neo-Hookean model.

inflation given in terms of the parameter

$$K = \frac{Q\beta\lambda}{R_0^3} \tag{B.36}$$

which is recognized to be a kind of Deborah number based on the retardation time $\beta\lambda$. Results are shown for the neo-Hookean model, and the fast deformation limit of the Doi-Edwards-Currie and Tom-Pom models. The trace for the neo-Hookean model with $K = 0.01$ is indistinquishable from the ideally elastic trace in Figure 9 (corresponding to $K = 0$). As the flow rate is increased, the material generates increasingly high stresses. This is the result of the excitation of the relaxation times associated with the small retardation term. For $K = 10.0$ it is evident that very high pressures are indeed generated and it is in this sense that the response can be interpreted as being glassy.

We turn now to the behavior of the modified Doi-Edwards-Currie and Tom-Pom ($q = 1$) models for linear polymer melts in Figure 12. The traces are shown for $K = 0.01$ so by analogy with the situation for the neo-Hookean model one would expect the traces to follow the trace for the unmodified fast deformation limits in Figure 9. Indeed this is correct up to the termination points for the ideally elastic computations in Figure 9, but the traces can be extended beyond the termination points due to the

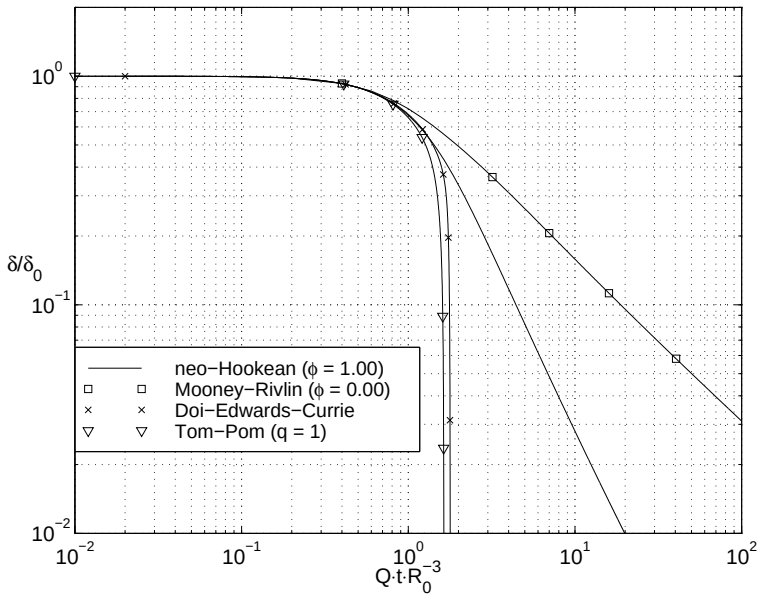

Figure B.13. Thickness of the membrane at the pole as function of time shown for a number of materials all with $\beta = 0.01$ and $K = 0.01$. The Tom-Pom ($q = 1$) and Doi-Edwards-Currie models exhibit catastrophic thinning near the pole whereas the Mooney-Rivlin ($\phi = 0.00$) and neo-Hookean materials show asymptotic behavior with slopes of $-2/3$ and $-3/2$ respectively. A membrane of uniform thickness corresponds to a straight line with slope $-2/3$.

stabilization by the small retardation term. This enables us to investigate further the behavior near the termination points. In Figure 13 we show the thickness of the membrane at the pole as function of time for a neo-Hookean model ($\phi = 1.00$), a Mooney-Rivlin model ($\phi = 0.00$), the Doi-Edwards-Currie model and the Tom-Pom ($q = 1$) model all modified with a retardation term $\beta = 0.01$ and $K = 0.01$. It should be noted that a membrane of uniform thickness will correspond to a straight line with a slope of $-2/3$ in this plot. Indeed the Mooney-Rivlin material does show an asymptotic behavior with a slope $-2/3$. This is in agreement with the Considère-Pearson criterion since the pressure vs. inflation is a monotone increasing function for this material. The membrane thickness at the pole of the neo-Hookean material by contrast decreases faster and has a limiting slope of $-3/2$. Hence the membrane becomes very thin near the pole, but it does not "burst". Finally the membranes composed of the Doi-Edwards-Currie and the Tom-Pom ($q = 1$) materials show a catastrophic thinning near the pole. Clearly the thickness goes to zero in finite time, so the membrane bursts.

The traces for the Tom-Pom model of branched polymer melts (not shown) follow the neo-Hookean trace until branch-point withdrawal. This happens when $I_1 = 3q^2$ or at a thickness $\delta/\delta_0 \approx 2/3q^2$. At this instant we expect the membrane to show catastrophic thinning similar to the situation for $q = 1$. The interrelation of polymer architecture and stability boundaries for several strong stretching processes is discussed further in a companion paper (McKinley and Hassager, 1999).

B.7 Conclusions

We have presented a finite element method for the simulation of inflation of axisymmetric viscoelastic membranes. The method uses a stress representation that is constant in each element and discontinuous at the element boundaries. The method converges to second order with the element size.

The simulations show that fast behavior may be controlled by viscous components to the stress. Effectively the limitation in deformation rates due to the onset of glassy behavior can be described in this way.

A qualitative understanding of the behavior of inflated membranes may be obtained from the Considère-Pearson criterion which we formulate as follows:

> Uniform inflation of an elastic membrane is guaranteed provided the pressure is a monotone increasing function of the volume.

A wide range of Mooney-Rivlin materials satisfy this condition and do indeed develop a uniform membrane thickness. The simulations indicate that the criterion is a sufficient but not necessary condition for stability of inflation.

Several molecularly based models such as the neo-Hookean, Doi-Edwards or Tom-Pom model cease to satisfy the Considère-Pearson criterion at a critical inflation. We have simulated two types of behavior in these situations. The neo-Hookean model develops a strong local thinning of the membrane but do not burst in finite time. The Doi-Edwards-Currie model and the Tom-Pom model for linear polymer melts exhibit a catastrophic local thinning of the membrane and burst.

Acknowledgments

The authors would like to thank a number of people for numerous stimulating discussions on membrane inflation including G.H. McKinley, J. Schieber, J.H. Christensen, C.L. Lauritsen and H.K. Rasmussen.

References

Adkins, J. E. and Rivlin, R. S. (1952). Large elastic deformations of isotropic materials IX The deformation of thin shells. *Philos. Trans. R. Soc. (London) A*, pages 505–531.

Bird, R. B.; Hassager, O.; Armstrong, R. C. and Curtiss, C. F. (1987). *Dynamics of Polymeric Liquids Vol I: Fluid Mechanics*. Addison-Wesley, New York, second edition.

Charrier, J. M.; Shrivastava, S. and Wu, R. (1987). Free and contrained inflation of elastic membranes in relation to thermoforming - axisymmetric problems. *J. Strain Analysis*, **2**, 115–125.

Charrier, J. M.; Shrivastava, S. and Wu, R. (1989). Free and contrained inflation of elastic membranes in relation to thermoforming - nonaxisymmetric problems. *J. Strain Analysis*, **24**, 55–74.

Cogswell, F. N. and Moore, D. R. (1974). A comparison between simple shear, elongation and equal biaxial extension deformations. *Polymer Eng. Sci.*, **14**, 573–576.

Cook, W. A. (1982). A finite element model for nonlinear shells of revolution. *Int. J. Numer. Meth. Eng.*, **18**, 135–149.

Currie, P. K. (1982). *J. Non-Newtonian Fluid Mech.*, **11**, 53–68.

Derdouri, A.; Connolly, R.; Khayat, R.; Verron, E. and Peseux, B. (1998). *Material constants identification for thermoforming simulation*. ANTEC 1998, Atlanta, Georgia, USA, April 26–30.

Doi, M. and Edwards, S. F. (1978). Dynamics of concentrated polymer systems. Part 1–3. *J. Chem. Soc. Faraday Trans. II*, **74**, 1789–1832.

Fried, I. (1982). Finite element computation of large rubber membrane deformations. *Int. J. Numer. Meth. Eng.*, **18**, 653–660.

Green, A. E. and Adkins, J. E. (1970). *Large Elastic Deformations*. Oxford University Press, London.

Khayat, R. E.; Derdouri, A. and Garcia-Rejon, A. (1993). Multiple contact and axisymmetric inflation of hyperelastic membranes. *Proc. Instn. Mech. Engrs. C: J. Mech. Eng. Sci.*, **207**, 175–183.

McKinley, G. H. and Hassager, O. (1999). The Considère Condition and Rapid Stretching of Linear and Branched Polymer Melts. *J. Rheol.*, **43**, 1195–1212.

McLeish, T. C. B. and Larson, R. G. (1998). Molecular constitutive equations for a class of branched polymers: The Pom-Pom model. *J. Rheol.*, **42**(1), 81–110.

Mooney (1940). *J. Appl. Phys.*, **11**, 582.

Novotný, P.; Kouba, K. and Sáha, P. (1998). The role of material in the simulation of the thermoforming process: Progress and trends in rheology. In *Proceedings of the fifth European rheology conference*, pages 367–368, Portorož, Slovenia.

Oden, J. T. and Sato, T. (1967). Finite strains and displacements of elastic membranes by the finite element method. *Int. J. Solids Structures*, **3**, 471–488.

Rivlin, R. S. (1948). Large elastic deformations of isotropic materials I Fundamental concepts. *Philos. Trans. R. Soc. (London) A240*, pages 459–490.

Treloar, L. R. G. (1958). *The Physics of Rubber Elasticity*. Oxford University Press, London.

Wagner, M. H. (1994). The origin of the C_2 term in rubber elasticity. *J. Rheol.*, **38**, 655–679.

Warby, M. K. and Whiteman, J. R. (1988). Finite element model of viscoelastic membrane deformation. *Computer Meth. in Appl. Mech. and Eng.*, **68**, 33–54.

Wineman, A. (1978). On axisymmetric deformations of nonlinear viscoelastic membranes. *J. Non-Newtonian Fluid Mech.*, **4**, 249–260.

Wineman, A. (1979). On the simultaneous elongation and inflation of a tubular membrane of a BKZ fluid. *J. Non-Newtonian Fluid Mech.*, **6**, 111–125.

Wineman, A. S. (1976). Large axisymmetric inflation of a nonlinear viscoelastic membrane by lateral pressure. *Trans. Soc. Rheol.*, **20**, 203–225.

Yang, W. H. and Feng, W. W. (1970). On axisymmetric deformations of nonlinear membranes. *J. Appl. Mech.*, pages 1002–1011.

C

Joint Authorship Declarations

Joint Authorship Declaration

Regarding the article "*Linear Viscoelastic Predictions of a Full-Chain Reptation Model with Chain-Length Fluctuations and Constraint Release*" by Jesper Neergaard (first author), Jay D. Schieber and David C. Venerus (co-authors).

As co-author of the above article I hereby accept that the first author includes it as a chapter in his Ph. D. thesis entitled "*A Stochastic Approach to Modeling the Dynamics of Linear, Entangled Polymer Melts*". I verify that all numerical simulations and post processing of the results, on which the paper is based, were carried out by the first author.

I contributed to the article by supervising the first author and by engaging in discussions about the results. The article was written jointly by the first author and me.

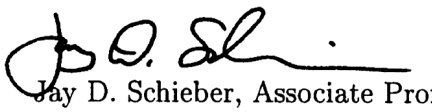

Jay D. Schieber, Associate Professor

Joint Authorship Declaration

Regarding the article "*Linear Viscoelastic Predictions of a Full-Chain Reptation Model with Chain-Length Fluctuations and Constraint Release*" by Jesper Neergaard (first author), Jay D. Schieber and David C. Venerus (co-authors).

As co-author of the above article I hereby accept that the first author includes it as a chapter in his Ph. D. thesis entitled "*A Stochastic Approach to Modeling the Dynamics of Linear, Entangled Polymer Melts*". I verify that all numerical simulations and post processing of the results, on which the paper is based, were carried out by the first author.

I contributed to the article by supervising the first author and by engaging in discussions about the results and the manuscript. All experimental work presented in the paper was carried out by me.

David C. Venerus, Associate Professor

Joint Authorship Declaration

Regarding the article "*Dynamics of Linear, Entangled Polymeric Liquids in Shear Flows*" by Jesper Neergaard (first author) and Jay D. Schieber (co-author).

As co-author of the above article I hereby accept that the first author includes it as a chapter in his Ph. D. thesis entitled "*A Stochastic Approach to Modeling the Dynamics of Linear, Entangled Polymer Melts*". I verify that all numerical simulations and post processing of the results, on which the paper is based, were carried out by the first author, who also wrote the first draft of the manuscript.

I contributed to the article by supervising the first author and by engaging in discussions about the results and the manuscript.

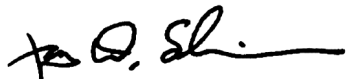

Jay D. Schieber, Associate Professor

Joint Authorship Declaration

Regarding the article "*Exponential Shear Flow of Linear, Entangled Polymeric Liquids*" by Jesper Neergaard (first author), Kyungho Park, David C. Venerus and Jay D. Schieber (co-authors).

As co-author of the above article I hereby accept that the first author includes it as a chapter in his Ph. D. thesis entitled "*A Stochastic Approach to Modeling the Dynamics of Linear, Entangled Polymer Melts*". I verify that all numerical simulations and post processing of the results, on which the paper is based, were carried out by the first author.

I contributed to the article by supervising the first author and by engaging in discussions about the results. The article was written jointly by the first author and me.

Jay D. Schieber, Associate Professor

Joint Authorship Declaration

Regarding the article "*Exponential Shear Flow of Linear, Entangled Polymeric Liquids*" by Jesper Neergaard (first author), Kyungho Park, David C. Venerus and Jay D. Schieber (co-authors).

As co-author of the above article I hereby accept that the first author includes it as a chapter in his Ph. D. thesis entitled "*A Stochastic Approach to Modeling the Dynamics of Linear, Entangled Polymer Melts*". I verify that all numerical simulations and post processing of the results, on which the paper is based, were carried out by the first author.

I contributed to the article by supervising the first author and by engaging in discussions about the results and the manuscript. All experimental work presented in the paper was carried out by my graduate student Kyungho Park and me.

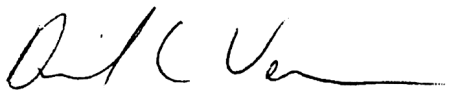

David C. Venerus, Associate Professor

Joint Authorship Declaration

Regarding the article "*Inflation and Instability of a Polymeric Membrane*" by Ole Hassager (first author), Susanne B. Kristensen, Johannes R. Larsen and Jesper Neergaard (co-authors).

The first author and the co-authors of the article hereby accept that Jesper Neergaard appends the above article to his Ph. D. thesis entitled "*A Stochastic Approach to Modeling the Dynamics of Linear, Entangled Polymer Melts*". The first author and the co-authors also verify that with the exception of Section 5 all numerical simulations and post processing of the results, on which the paper is based, were carried out by Jesper Neergaard. The article was written by the first author and Jesper Neergaard furthermore contributed by engaging in discussions about the results.

Ole Hassager, Professor